Incoherent ϕ photo-production from deuteron at SPring-8/LEPS

Manabu Miyabe

Incoherent ϕ photo-production from deuteron at SPring-8/LEPS

（SPring-8/LEPS における重水素標的を用いたインコヒーレント ϕ 中間子生成）

Manabu Miyabe

The members of committee approved this thesis defended on Janualy 26th, 2010 :

Professor Takashi Nakano,	Research Center for Nuclear Physics, Osaka university
Professor Hiroshi Toki,	Research Center for Nuclear Physics, Osaka university
Professor Tadafumi Kishimoto,	Department of physics, Osaka university
Professor Masaru Yosoi,	Research Center for Nuclear Physics, Osaka university
Professor Toru Sato,	Department of physics, Osaka university
Professor Hiroyuki Noumi,	Research Center for Nuclear Physics, Osaka university

Abstract

We present measurements of differential cross sections and decay asymmetries of incoherent ϕ-meson photoproduction from the deuteron at forward angles using linearly polarized photons beam in energy range from the production threshold to E_γ=2.4 GeV. The experiment was performed at the SPring-8/LEPS facility. The differential cross section of incoherent production shows a large suppression compared with the free proton case. The reduction for the deuteron cannot be clearly explained in terms of simple isospin asymmetry. The decay asymmetry of incoherent ϕ photoproduction shows that the η exchange process is small. Since the exclusive K^+K^-p cross section shows the same reduction with incoherent, both the proton and neutron cross section reduce similarly. Consequently, the π η interference effect is small too.

The present results suggest that our understanding of ϕ-photoproduction within a nucleus should be rearranged. The small pseudo-scalar amplitude supports the existence of an exotic process in the cross section enhancement from proton.

Contents

Chapter 1

Physics Motivation

In recent physics, a QCD framework achieves great success to discribe the strong interactions in hadron. QCD developed the meson and barions mechanisms which were supported by many experiments, on the other hand, there still exist theoretical predictions without observation. Hadrons are restricted to colorless states by QCD quark confinement, gluon and glueball which carries the strong interaction with these hadrons. To study ϕ photo-production from nucleon is useful tool to explore such gluonic interactions . Because the meson photoproduction process are considered Pomeron exchange, and pseudoscalar meson(π,η) exchange, except for second-Pomeron as glueball candidate[1][2][3], we have to explore such all process precisely. Some theoretical predictions shows that near the production threshold energy, second Pomeron becomes comparable with simple pomeron exchange process which dominant in high energy region. In addition, since the OZI rule strongly suppresses conventional meson (π,η) exchanges in the t-channel, ϕ meson production provides opportunity to study these nonconventional production mechanisms. Such a study is difficult in ρ and ω photoproduction, since the contribution from meson exchange processes is dominant in the threshold.
To study photoproduction from a deuteron target which contains neutron is useful to examine the π and η exchange process from the isotopic effect of proton and neutron.
In this thesis, with extracting the quasi-free ϕ photo-production from neutron in deuteron target, we investigate the meson exchange process amplitude which is infomation for the exotic glueball exchange mechanisms. The experimental and theoretical backgrounds for this study are discribed below.

1.1 Introduction

1.1.1 ϕ photoproduction from proton

The experimental study for ϕ photoproduction of vector meson near the threshold energy becomes active during recent years. In the high energy region, the total cross section of vector meson increases roughly in proportion to incident photon energy. This energy dependence of the cross section is understood by vector meson dominance (VMD)[4], where at forward angles, photon behaves as a vector meson and the interaction of vector meson with nucleon occurs when a fluctuation time is long enough.

The weak energy dependence and the exponential decrease of differential cross sections

as a function of momentum transfer t at high energies are well interpreted as the Pomeron exchange process in the Regge theory[5]. It was expected that in the diffractive region the dominant contribution comes from the Pomeron exchange, since the processes associated with conventional meson (quark) exchanges are suppressed by the OZI rule. For example, the pseudo scalar π and η meson exchanges are suppressed and relatively small compared with the dominant Pomeron exchange process. These models are designed for the vector meson photoproduction at high energy and small momentum transfer. The adaptation of these models into the low energy region and close to the threshold is not clear.

On the other hand, in resent experimental results[6] in the threshold energy region, the cross section at forward angle is not simply decreased with energy (Fig1.1). The data show a bump structure around $E_\gamma \sim 2$ GeV. The model based on the calculation[3] including Pomeron exchange and π/η exchange processes failed to explain such a bump structure. Another peculiarity of this data is a strong deviation of the spin-density matrix element ρ^1_{1-1} from 0.5(Fig1.2), which is in favor of a sizable contribution of unnatural parity exchange processes. If natural-parity exchange(Pomeron, 0^+ glueball) is dominant, ρ^1_{1-1} close to +0.5, in a contrasting situation, if unnatural-parity exchange(pseudo-scalar) is dominant, ρ^1_{1-1} reaches -0.5 (Ref. Section A). The relative contribution between the natural parity exchange and the unnatural parity exchange in this experiment has no energy dependence of ρ^1_{1-1} around the bump structure. As mentioned before, a contribution from the Pomeron exchange decreases with decreasing energy, and the contributions from the pseudo-scalar exchange increase. In order to keep the relative contribution same, additional natural-parity exchange mechanisms (glueball exchange) are expected[3].

- To clarify the exotic process like a glueball exchange, it is important to examine the π and η meson exchange mechanisms.

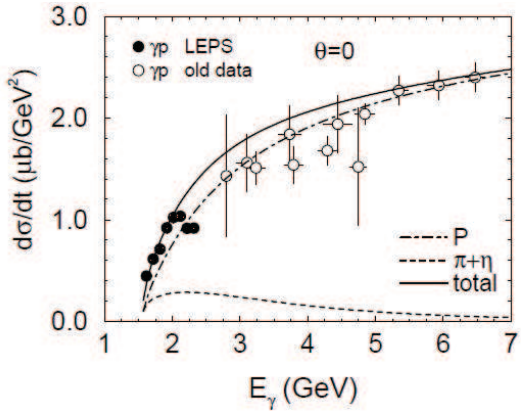

Figure 1.1: Differential cross section of the $\gamma p \to \phi p$ reaction at $t = t_{min}$ as a function of the photon energy. [6]

1.1.2 ϕ photoproduction from deuteron

The study of ϕ photoproduction off deuteron is considered a useful tool for such analysis of production mechanisms. In Fig 1.3, the coherent and in-coherent ϕ meson photoproduction

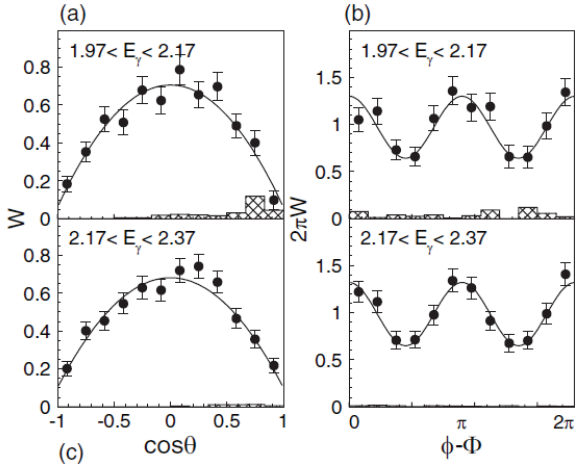

Figure 1.2: Decay angular distributions in the Gottfried-Jackson frame $\rho^{-1}_{1-1} = 0.197 \pm 0.03(\text{stat}) \pm 0.022(\text{syst})$ in E1(1.97GeV¡E_γ¡2.17GeV) and $0.189 \pm 0.024(\text{stat}) \pm 0.006(\text{syst})$ in E2(2.17GeV¡E_γ¡2.37GeV) [6]

processes are exhibited.

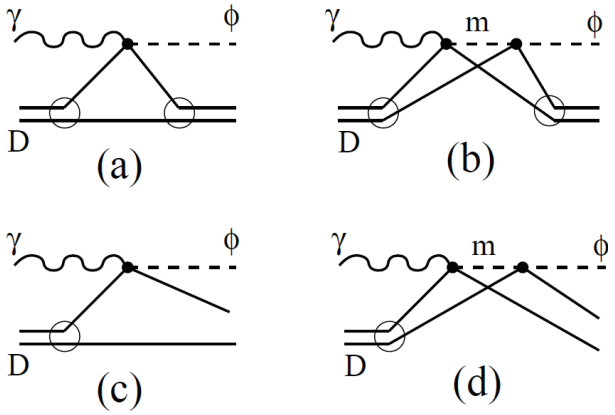

Figure 1.3: Diagrammatic representation of coherent (a,b) and in-coherent (c,d) ϕ meson photoproduction in γD reactions with single (a,c) and double (b,d) scattering contributions. [7].

In the case of the coherent ϕ photoproduction off the deuteron (Fig.1.3 a,b), the isovector π-meson exchange amplitude is eliminated because of its isoscalar target. Recently experimental results[8],[9] of coherent ϕ photoproduction off deuteron are reported. The cross section and the decay angular distribution of the coherent production off deuteron at forward angle(Fig.1.4) shows a strong increase with photon energy and a complete dominance of helicity-conserving natural-parity exchange processes(Fig.1.5). The absence of unnatural-parity isovector π-exchange, together with negligible contribution of η-exchange is inferred. Nevertheless the model calculation taking into account pomeron and η-exchange processes are not well consistent at low energies. From this, additional pomeron trajectory or additional natural-parity processes beyond pomeron exchange in the near-threshold region are required.

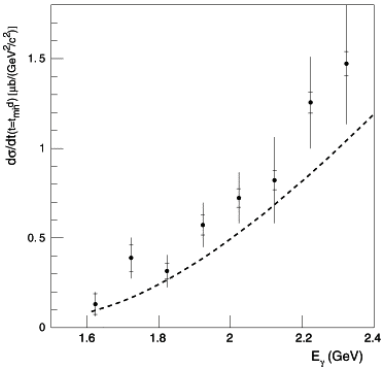

Figure 1.4: $d\sigma/dt$ at $t = t_{min}$ as a function of photon energy. The dashed line is the prediction of $d\sigma/dt$ at zero degree by a model including pomeron and η-exchange processes

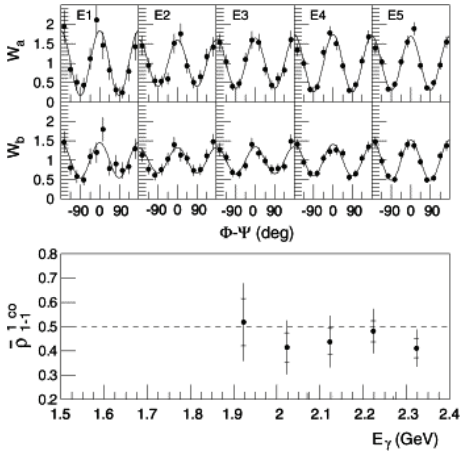

Figure 1.5: The decay angular distributions $W_{a,b}(\phi, \Phi)$ of K^+K^- pair events overlaid with the fit in five E_γ bins of equal width and the decay asymmetry of $\gamma d \to \phi d$ as a function of photon energy. The subscript a (b) denotes the events of missing mass smaller (larger) than 1.89 GeV/c^2. The E_γ binning starts from E1=(1.87,1.97) GeV and ends at E5=(2.27,2.37) GeV.

1.1.3 incoherent ϕ photoproduction from deuteron

In this thesis, the analysis of incoherent photoproduction off deuteron (Fig.1.3) is presented. In Ref. [2], since coupling constant $g_{\eta pp}$ and $g_{\pi pp}$ have the same sign, it is predicted that a constructive interference between isovector-π and isoscalar-η exchange amplitudes happens for the $\gamma p \to \phi p$ process. By contrast, it becomes a destructive interference for the $\gamma n \to \phi n$, because $g_{\pi nn}$(=-$g_{\pi pp}$) is of opposite sign of $g_{\eta nn}$(=$g_{\eta pp}$) based on isospin symmetry. According to the model calculation at small momentum transfer $|t|$ regions, this isospin π-η interference would lead to a small reduction of cross section for the interactions with neutron target, relative to those with proton target(Fig1.7). A more visible effect is the increase of decay asymmetry toward the limit of complete natural-parity exchange processes (Fig1.7). Experimental measurements of decay asymmetry in the incoherent process will help investigate the amount of isospin asymmetry and also information of production mechanisms. Since the cross section and decay asymmetry for quasi-free incoherent ϕ photo-production provide the amplitude

of pseudo-scalar exchange process, it supports to understand the new additional production mechanisms like a glueball exchange.

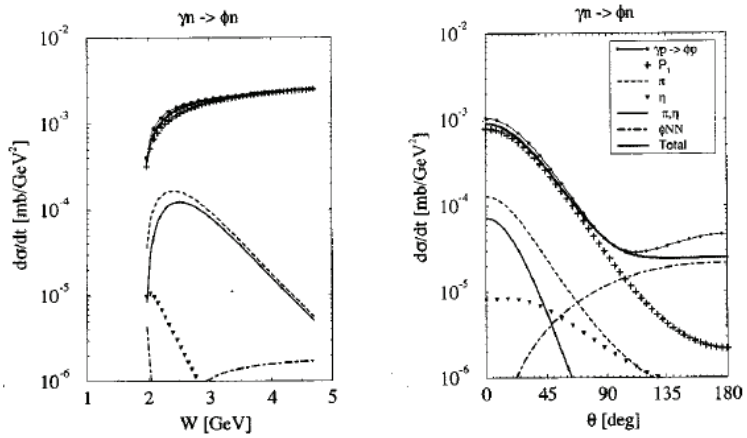

Figure 1.6: The differential cross section of $\gamma n \to \phi n$ at $t = t_{min}$ in the left panel, The right panel shows the angular distribution at $E_\gamma = 2$ GeV (W = 2.15 GeV). Dot-marked thin lines correspond to the $\gamma p \to \phi p$ reaction.[2]

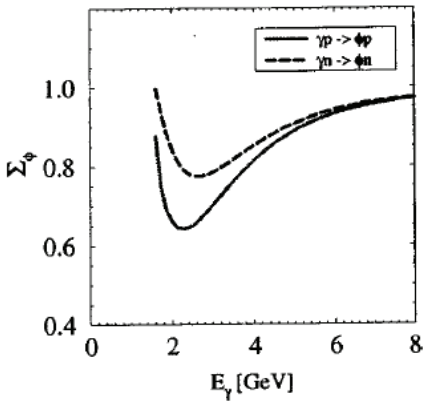

Figure 1.7: The predicted decay asymmetry $\Sigma_\phi = 2\rho^{-1}_{1-1}$ distribution as a function of photon energy. A solid and dashed line show proton and neutron case respectively.[2]

1.1.4 Physics goal

The objectives of this paper are as follows,

- The bump structure in the cross section for $\gamma p \to \phi p$ reaction [6] indicates the existence of exotic process. Sizeable deviations of spin density matrix element ρ^1_{1-1} from 0.5(pure natural parity exchange) is explained by a large contribution of the unnatural parity π,η exchange processes. But, since no energy dependence of ρ^1_{1-1} and the contribution from the Pomeron exchange decreases as decreasing energy, an additional contribution with natural parity exchange such as glueball exchange is needed corresponding to the increasing unnatural parity contribution π η. Hence, in order to investigate this additional contributions, the strength of π, η exchange process is quite important in this energy region.

- For isotopic effect, constructive interference between π and η happens for the $\gamma p \to \phi p$ process. To investigate the π-η interference, comparison of the cross section for $\gamma p \to \phi p$ with the cross section for $\gamma n \to \phi n$ is useful method. When the strong π-η interference is observed, the η exchange amplitude is possibly comparable with π exchange.

- The spin density matrix ρ^1_{1-1} for incoherent photo-production at forward angle is sensitive to the η exchange process amplitude [10]. When the discrepancy with ρ^1_{1-1} for proton and neutron is large, the η exchange process amplitude grows up correspondingly.

- The result of ϕ photo-production off nuclei [11] showed a large target mass number dependence of A^α. In a simple Glauber approximation, the inelastic ϕ-N cross section $\sigma_{\phi N}$ was determined to be about 35 mb which significantly larger than theoretical predictions. But in these study, they assumed that ϕ photo-production off nucleon in nuclei occured diffractively from the isospin-independent free nucleon. For an examination of model, it is reliable to adapt these assumption to the simplest nucleus deuteron, where nuclear density effects are minimized.

As explained above, because the cross section and decay angular distribution for incoherent $\gamma N \to \phi N$ provide the unique information of pseudo scalar π and η exchange process, we could explore the substantiality of the exotic (glueball exchange) process for the bump structure in $\gamma p \to \phi p$ cross section.
In this thesis, we report the measurement of the differential cross section and decay angular distribution for incoherent ϕ photo-production $\gamma N \to \phi N$ from deuteron at forward angles near the production threshold with linearly-polarized photon beam.

Chapter 2

Experimental apparatus

The decay angular distributions and the differential cross sections of ϕ photoproduction were measured at the SPring-8/LEPS facility. The linearly-polarized photons were produced at SPring-8 BL33LEP beamline (LEPS facility). The liquid hydrogen target was installed and irradiated to the beam. The LEPS facility consists of a laser transport system, a photon tagging system (tagger), a new liquid hydrogen and deuteron target and a charged particle spectrometer. The experimental apparatus of the measurement is described in this chapter.

2.1 The beam

2.1.1 The backward Compton scattering

A Compton scattering of photons by electrons is one of the most simple process in quantum electrodynamics (QED). In 1963, Milburn [12] and Tumanian [13] pointed out that high energy polarized photons are produced by collisions of polarized laser photons with relativistic electrons at a direction of electrons. This process is generally called as Backward Compton Scattering (BCS). Energies of scattered photons are the same order of magnitude as those of electrons. For example, a few GeV photons are able to be produced by shooting a few eV light to 8 GeV electrons.

The BCS provides an opportunity to obtain high energy photon beams in electron accelerators. The first photon beam facility by using the BCS technique for physics measurements has been built at SLAC [14] in 1969. Since 1969, the BCS technique has been used to make a high energy photon beam [15, 16, 17]. On the basis of these facility construction and of the new development of laser technology, we have built a new facility (LEPS facility) for the BCS photon beam at the SPring-8 in Hyogo, Japan for the measurements of photoproduction of mesons and/or baryons [18]. The LEPS facility provides the BCS photon beams of the world highest energies (maximum 2.4 GeV) where the photoproduction of the ϕ meson can be studied from the threshold (E_γ=1.573 GeV). The Ar-ion laser (Coherent Sabre) was used as a source of photons in the UV region (333.6-363.8 nm).

An energy spectrum of scattered photons in the BCS process has a quasi-flat shape. On the other hand, the production of Bremsstrahlung photons, which is widely used to produce high energy photons, results in a spectrum proportional to $\sim 1/E_\gamma$, i.e. many low energy photons are produced due to the divergence at low energy. Low energy photons, which can not

produce ϕ mesons, generate a large amount of e^+e^- pair backgrounds. Amount of such low energy photons can be much reduced in the BCS photon beams. Figure 2.1 (left-hand side) shows the energy spectrum of the BCS photons produced from the collision of 351 nm (single line) laser against the 8 GeV electron beam at the SPring-8 storage ring. The measurement was performed by using a full-absorption type electromagnetic calorimeter consists of PbWO crystals [19]. For comparison, the energy spectrum of the Bremsstrahlung photon when the laser light was turned off is shown in right-hand side of Fig.2.1. The flatness of the energy spectrum of the BCS photon beam compared to the Bremsstrahlung photon is evident.

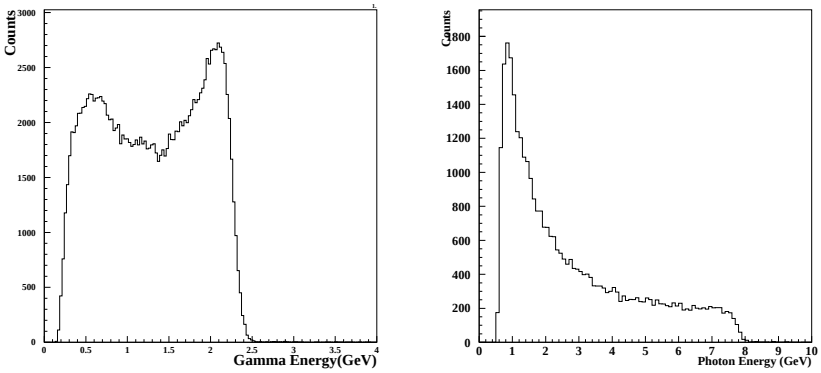

Figure 2.1: Energy spectrum of the BCS photon at the LEPS facility (left-hand side), Energy spectrum of the gas Bremsstrahlung photon (right-hand side)

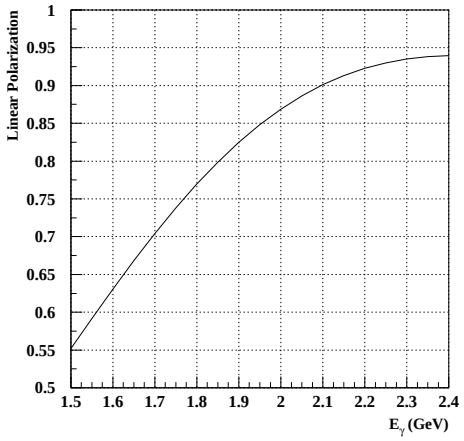

Figure 2.2: Linear polarization as a function of photon energy. 100% polarization of the laser light is assumed in the calculation.

Since the polarization of laser light is transferred to the photon beam according to the QED, high degree of polarization can be easily achieved. The linear polarization of the BCS photons depends on photon energy as shown in Figure 2.2. The maximum polarization amounts to

94% for the highest photon energy (2.4 GeV) when a 100% linearly-polarized laser is used. There is no major difficulty for controlling the polarization states of the BCS photons since the direction of the laser polarization is easily handled. The high degree of polarization allows us to perform precise measurements of polarization observables which are important to unveil the reaction mechanisms as discussed in Appendix A.

2.1.2 Beamline set-up

The SPring-8 (Super Photon ring-8 GeV) is the facility of the 3rd generation synchrotron radiation source. The SPring-8 composed of 1 GeV injector linac, 8 GeV booster synchrotron, and 8 GeV electron storage ring. There are 61 beamlines available for scientific research activities [20]. The laser-electron photon facility was built at the beamline BL33LEP which is dedicated for the experiments of subnuclear physics research [21, 22, 23, 24, 25, 26].

The laser optics

A schematic view of the laser optics is shown in Fig. 2.3. An Ar-ion laser (Coherent Sabre) was used as a source of photons. The laser was operated with a multi-line mode. The wave length of the laser beam consists of several lines in the UV region (333.6-363.8 nm) where the major components are 351.1 nm and 363.8 nm. Thanks to the property of laser resonator, the emitted laser beam is almost 100% linearly polarized. A typical power of the laser beam was about 5 W. The laser beam size was enlarged by a beam expander, which consisted of a couple of optical lens to focus at the straight section of the storage ring where the electron beam circulated. Four optical mirrors were used to navigate the laser beam to the storage ring. The direction of linear polarization of the laser beam was controlled by a half wave length plate ($\lambda/2$ plate). We set the direction of the linear polarization (define as the direction of the electric field) to the vertical direction and the horizontal direction in the measurement. The direction of polarization was changed in every a few hours. The polarization angle and degree were measured at the end of the straight section in the storage ring. A Glan-laser prism was used as a polarization analyzer. In the polarization measurement, the Glan-laser prism was rotated and the intensity of the laser was measured behind the prism with a photodiode as a function of rotation angle of the polarizer. Fig. 2.4 shows the intensity distributions of the laser after a polarizer for the vertical and horizontal polarized laser. The angle and degree of the polarization were obtained by analyzing spectrum [27].

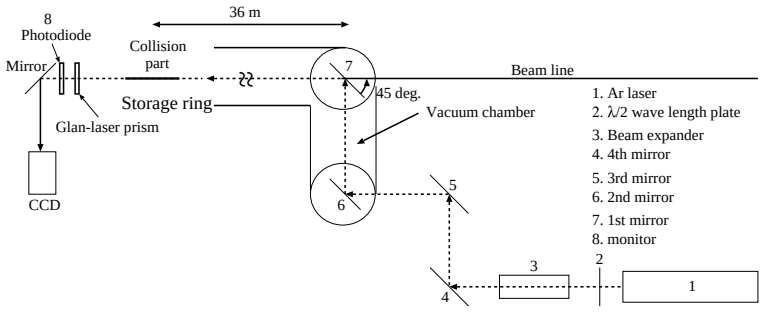

Figure 2.3: Laser optics of the LEPS facility

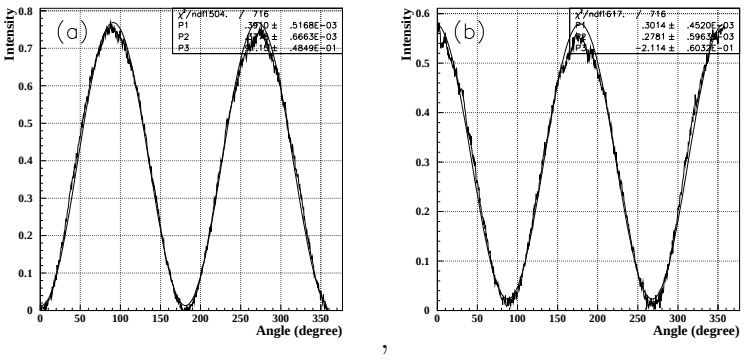

Figure 2.4: Intensity of photo-diode output as a function of the angle of the Glan-laser prism for (a) vertically polarized laser, (b) horizontally polarized laser [27]. The curves are the results of fitting to the data with a function of sine function plus constant.

2.2 The tagger

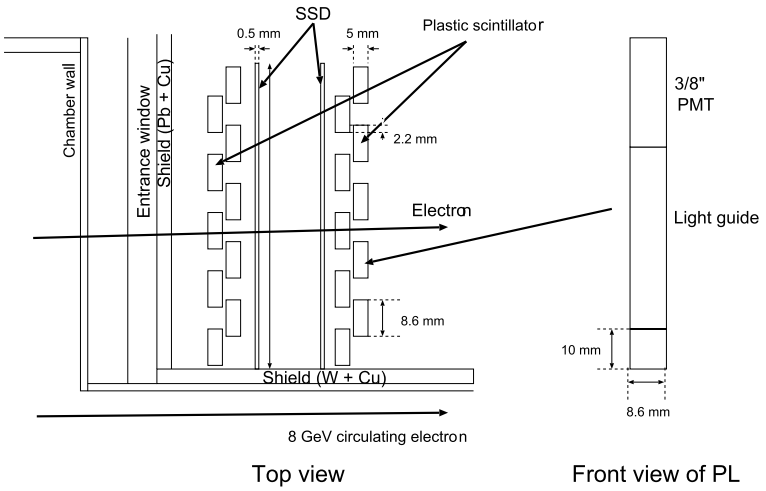

Figure 2.5: The tagging counter

The energy of photons was determined by measuring the energy of the recoiled electron $E_{e'}$. The energy conservation of the electron and photon leads the energy of photons as $E_\gamma = E_e - E_{e'}$ where E_e is the energy of the electron beam circulating in the storage ring (7.975 ± 0.003 GeV [28]). The recoiled electrons were detected with the tagging counter which was installed at the downstream of the bending magnet of the storage ring. The backward Compton scattering takes place at the straight section of the storage ring. The recoiled electrons passed through the bending magnet which bent the recoiled electron trajectory. Displacement of the trajectory at the downstream of the bending magnet depends on the energy of recoiled electrons. The position of tagging counter was corresponded to displacement of the recoiled electron from which the energy of photon was obtained. The tagging counter consisted of two layers of plastic scintillation counters and two layers of silicon strip detectors (SSD). A schematic view of the tagging counter is shown in Fig. 2.5. A layer of the plastic scintillation counter consisted of 10

segments of plastic scintillators which provided a timing signal of the recoiled electron signal. SSD consisted of 512 readout strips with a $100\mu m$ pitch which provided position information for the recoiled electron trajectory. The energy of photon was obtained by the position of the SSD strip. The photon energy resolution was 10 MeV [29] which was determined by the energy resolution of the electron beam and the performance of the bending magnet as a momentum analyzer for recoiled electrons. With the tagging counter, the photon energy from 1.5 GeV to 2.9 GeV was covered.

2.3 The target

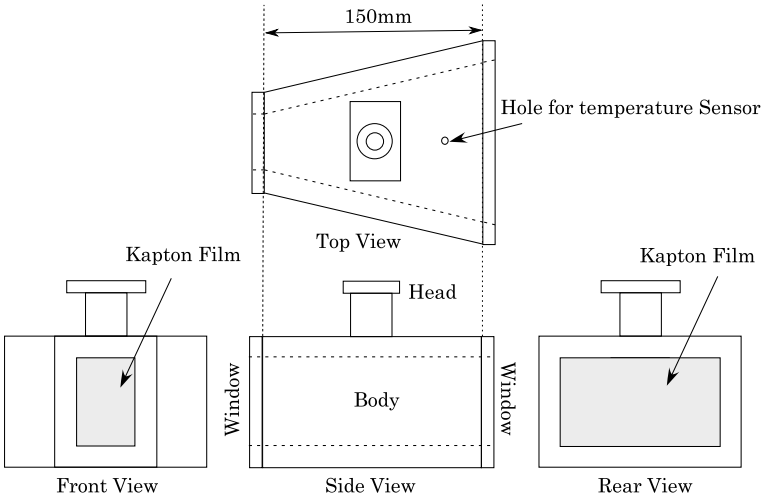

Figure 2.6: The liquid hydrogen target

A 150mm-long liquid hydrogen and deuterium target [30] was used in the experiment. This liquid target system has been upgraded from 50mm-long before experiment. The shape of the target is shown in Fig. 2.6. The inner size of the cell is about 660 cm^3 and the large acceptance of $|\theta_x| < 20^\circ$ and $|\theta_y|$ is achieved even the most upstream. The target cell was made of copper with a thickness of 8 mm. The entrance and exit windows of the target cell were made of Aramid films with a thickness of 125 μm. The target was located at the 995 mm upstream of the center of the dipole magnet (Section 2.4). The temperature and pressure of the target was kept at 20.5 K and 1.05 atom, respectively. The shape of the target cell was designed so that the target cell did not cut the acceptance of the charged particle spectrometer even when the reaction took place at the upstream of the target cell.

2.4 The charged particle spectrometer

The charged particle spectrometer consisted of a dipole magnet, tracking detectors, a start counter, a silica aerogel Čerenkov counter, an upstream veto counter and a time-of-flight counter. A schematic view of the charged particle spectrometer is shown in Fig. 2.7.

The dipole magnet provided the magnetic field for momentum analysis. Aperture of the dipole magnet was 55 cm high and 135 cm wide. The length of the pole along the photon

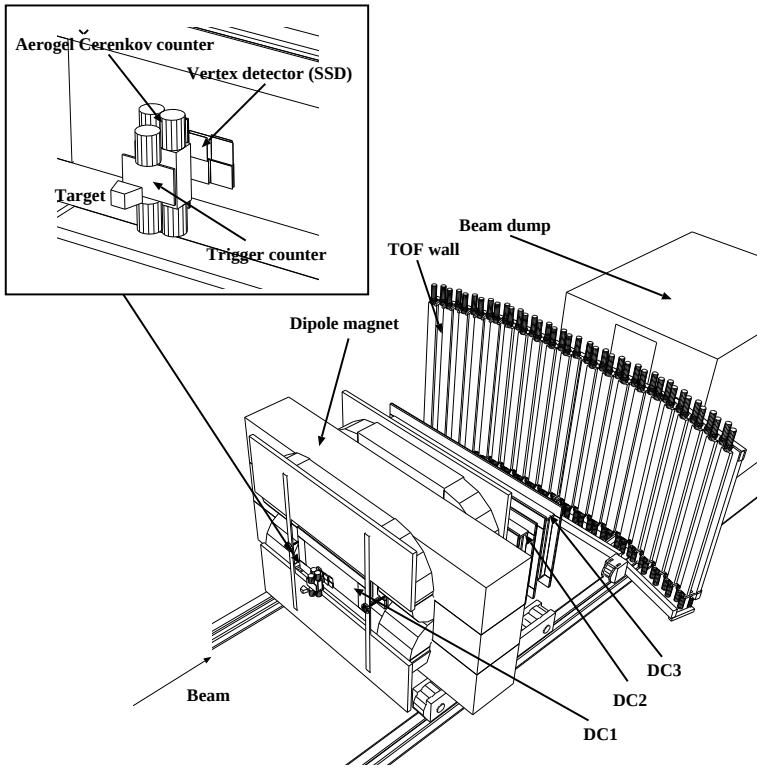

Figure 2.7: The LEPS charged particle spectrometer

beam was 60 cm. The maximum field strength was 0.7 T at the center of the dipole magnet. A current provided to the magnet was 800 A. A magnetic field map was calculated by using OPERA-3d TOSCA package [31] which provided the 3-dimensional magnetic field distribution. Results of the calculation by TOSCA agreed well with the measurements by hole probes. Inside the magnet, a pair of lead bar with 10 cm thick, 4 cm high and 44 cm wide were installed in the horizontal plane at the 20 cm downstream of the magnet center in order to block the e^+e^- pairs produced at upstream.

The tracking detectors consisted of a silicon vertex detector (SVTX) and three drift chambers (DC1, DC2 and DC3). The SVTX and DC1 were located at the upstream of the dipole magnet and DC2 and DC3 were located at the downstream.

The SVTX was a silicon strip detector with a thickness of 300 μm and with 120 μm strip pitch. Total number of strip was 8192 . Half of the strips were placed in the vertical direction and the other half were placed in the horizontal direction. There was a hole at the center of the detector where the photon beam went through without having any reactions with the detector. The efficiency of the SVTX detector was checked by good proton tracks reconstructed without using the SVTX hits. The efficiency was 100% for most of strips. There were 56 strips which were very noisy; They always gave high noise signals due to electrical noise (hot strip). The hot strips were killed in the offline analysis. The efficiency of the strips next to the hot strip were not 100% but 97% because of imperfection of collecting charge induced by the charged particle.

The DC1 consisted of 6 planes. There were 3 planes for the x direction, 2 planes for the u direction and 1 plane for the v directions. The u and v planes were inclined by +45° and -45°

with respect to the vertical direction. The field wires were arranged in a hexagonal shape. The active area of the DC1 was 30 cm high and 60 cm wide. The wire spacing of sense wires was 12 mm. The total number of wire for the x, u and v planes were 144, 96 and 48, respectively. The DC2 and DC3 have the same structure. They consisted of 5 planes with the two x plane, the two u plane and the one v plane. Here u and v planes were inclined by +30° and -30° with respect to the vertical direction. The field wires were arranged in a hexagonal shape. The active area of the DC2 and DC3 was 80 cm high and 200 cm wide. The spacing of sense wires was 20 mm. The windows of the entrance and exit of the DC1, DC2 and DC3 were made of aluminized-mylar sheet with a thickness of 125 μm. The efficiency of the drift chambers were 97-100% and the resolution was found to be approximately 200 μm [32].

The time-of-flight of the charged particle was measured using the start counter (TRG), the time-of-flight (TOF) counter, and RF signal of the accelerator. The start counter, which was made of a 5 mm thick plastic scintillator with 94 mm high 150 mm wide, provided a start timing of the trigger of data taking. The TOF start timing was given by the timing of RF signal of the accelerator with a frequency of 508 MHz. However, we found that there was a problem of RF signal in a part of data. In such a case, the start counter was used as a TOF start timing instead of the RF timing when RF signal was not valid. The TOF stop timing was provided by the TOF counter which consisted of 40 slats of 40 mm thick plastic scintillator with 2000 mm high and 120 mm wide. An average of timing resolution of TOF measurement was 123 psec when RF signal was used, and 170 psec when the start counter was used [33].

The silica aerogel Čerenkov counter (AC) was located at the downstream of the start counter to veto the events for e^+e^- pair creation in the trigger level. The index of the silica aerogel was 1.03. The Čerenkov threshold momentum for electron, pion and kaon were 0.002 GeV, 0.57 GeV and 2.0 GeV, respectively. The inefficiency of the Čerenkov counter for e^+e^- was about 0.1% [33].

The upstream veto counter (UPveto) was a plastic scintillation counter with a thickness of 5 mm, 200 mm high and 190 mm wide which was located at the 4 m upstream from the target. The UPveto was used to veto charged particles, most of which are e^+ and/or e^- produced at upstream, in trigger level.

2.5 Data acquisition

The trigger for the data taking [34] consisted of (1) a tagger signal (TAG) which was defined as the coincidence signal of valid signals of scintillator in each layer, (2) a signal from UPveto, (3) a signal from TRG (STA), (4) signal from AC, (5) a signal from TOF. Diagram of the readout logic for trigger was shown in Fig. 2.8. The main trigger (hadron trigger) was defined as

$$Tag \otimes \overline{UpVeto} \otimes STA \otimes \overline{AC} \otimes TOF \tag{2.1}$$

Another trigger (e^+e^- trigger) to monitor the detector by using e^+e^- event was prepared. The e^+e^- trigger was define as

$$Tag \otimes \overline{UpVeto} \otimes STA \otimes TOF \tag{2.2}$$

i.e. veto signal for AC was removed from the hadron trigger. The diagram of trigger logic is shown in Fig. 2.9. In the experiment, data were taken by these two triggers. The e^+e^- trigger

was pre-scaled so that trigger rate is sufficiently low. A typical trigger rate for the hadron trigger was 100 cps. The trigger rate for the pre-scaled-e^+e^- trigger was 4 cps.

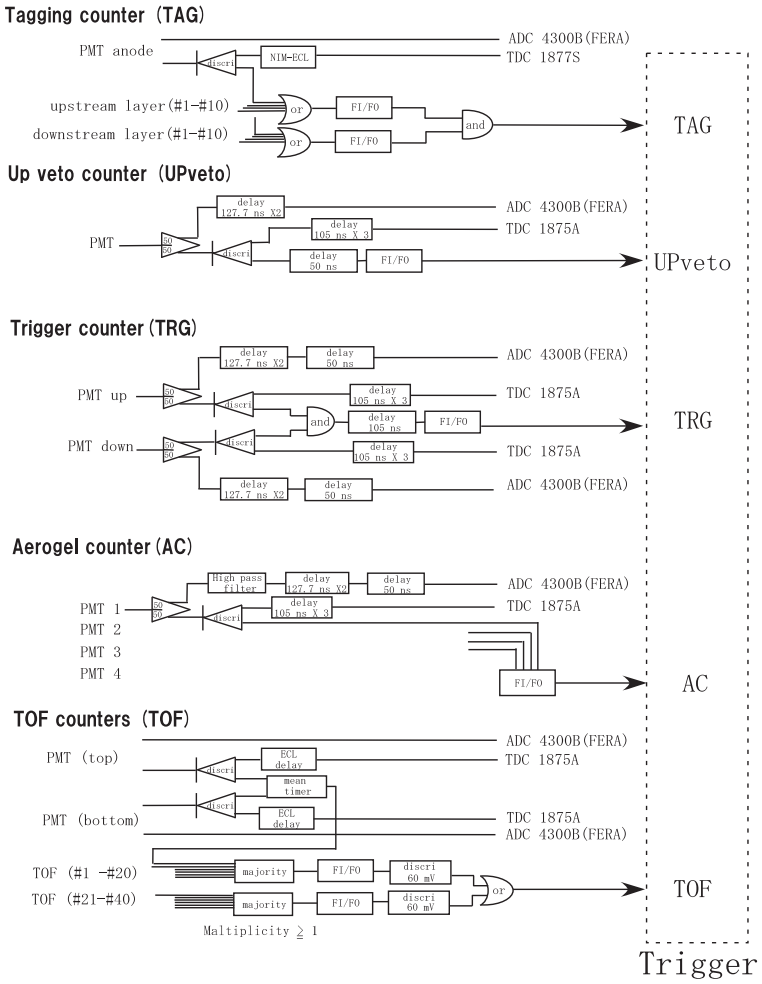

Figure 2.8: Read out logic

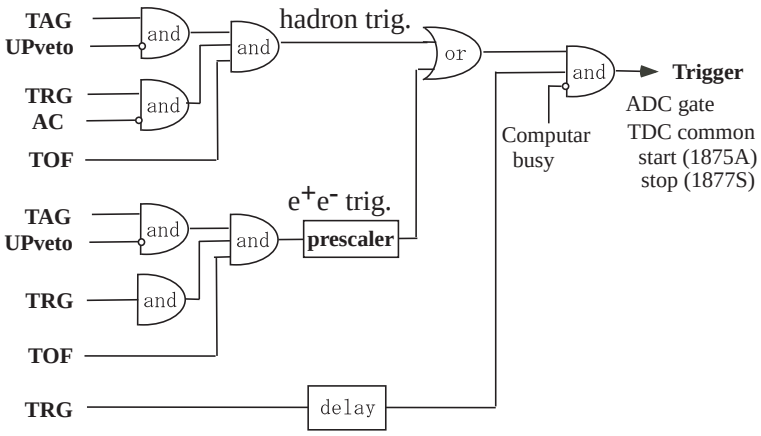

Figure 2.9: Trigger logic

Chapter 3

Data analysis

In this chapter, data analysis for the ϕ photoproduction is described.

3.1 Offline analysis program, LEPSana

A general offline analysis program (LEPSana) was developed by LEPS collaboration. LEPSana extract the raw data which are digital outputs of ADC and TDC from the LEPS detectors, and analyze the information on the beam energy and momenta, positions, mass of charged particles from the data. The outputs of the process were written in the NTUPLE format [35] and further analysis was done by accessing the ntuple in PAW.

The calibration of detectors and some parameters, such as timing offset and PMT gain of the TOF counter [33], the tagging counter timing offset [36], x-t curve (a conversion function from drift time to drift distance) and resolutions of the drift chambers [32], have been calculated. During the long run periods of data taking, variation of calibrations were corrected by run-by-run based parameters.

3.2 Monte Carlo simulation

The acceptance of the LEPS spectrometer for the ϕ photoproduction was studied by a Monte Carlo simulation for the LEPS spectrometer g3leps [37]. The g3leps has been developed by LEPS collaboration and is based on the CERN program library, GEANT 3.21 [38]. The g3leps simulates a generation of particles from the ϕ photoproduction reaction and processes during passage of the particles through the experimental apparatus which also including particle decay, energy loss, multiple scattering of particles. The ϕ mesons could be produced by arbitrary spin density matrices values. The GHEISHA package was used to simulate hadronic interactions. The g3leps describes responses of the detectors followed by a passage of the particles. The measured resolution and efficiency of the SVTX and the drift chambers, timing resolution of the TOF counter were implemented in the g3leps. A realistic beam shape of the polarized-photon beam and the beam energy resolution were implemented as well.

The output from the Monte Carlo simulator was very similar NTUPLE format to the offline analysis program, LEPSana which was used to analyze the real data. Monte Carlo data was analyzed by exactly the same analysis processes as in the case of the real data.

A Monte Carlo event generator dedicated for the generation of ϕ photoproduction reaction off deuteron target was developed. The momentum distribution of nucleons inside the deuteron target is modeled by the well-known PARIS potential [39]. The ϕ-meson event generator generated K^+K^- and proton(or neutron) from the reaction $\gamma+p(n) \rightarrow \phi+p(n)$, $\phi \rightarrow K^+ + K^-$ in the ϕ-meson rest frame with user-defined parameterization of cross section as a function of energy, momentum transfer and spin density matrix elements. And also, the coherent production $\gamma + D \rightarrow \phi + D$ is implemented.

The acceptance for ϕ photoproduction was studied by this Monte Carlo simulator (See Section 3.6).

For the study of the backgrounds in the K^+K^-p final state, non resonant K^+K^- production was used (see Section 3.7).

3.3 Drift Chamber

The experiment for this study was carried out during 2002∼2003. In this experiment (Long-LH_2, Long-LD_2), the target system was replaced from previous experiment (short-LH_2) in 2000∼2001. And also there are minor changes between these experiments. For example, the depth of the multi-hit TDC (the maximum number of accepted hits) was set to be 3 for DC2, DC3 and DC1X3 while it was set to be 8 for the previous (short-LH_2) experiment. When signal gain from wire is large, we have some small noise pulses and these noises could be accepted by TDC priority to a true pulse. This causes the large number of outliers (Sec.3.4.4) and the low plane efficiency. Fig.3.1 shows a TDC pluse width distributions for DC3. Clearly there are pulses come from noise around the width $\leq$ 40ch region.

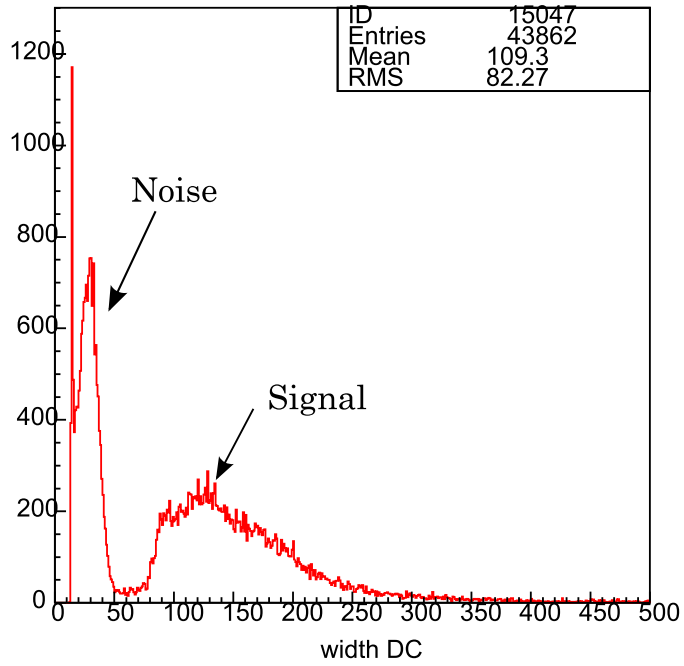

Figure 3.1: Drift chamber TDC width distribution

3.3.1 t_0 calibration

Drift chamber TDC timing offset value(t_0) is determined by fitting the right edge of the timing t distribution with a Gaussian convoluted step function since charged particles come with a uniform distribution in a local region. A drift time t_{drift} is determined from a this t_0, and a leading edge of the first hit t as

$$t_{drift} = -t - t_0 \times 0.5 nsec/channel. \tag{3.1}$$

Fig.3.2 shows Drift chamber TDC offset value(t_0) as a function of run number. The t_0 is not stable during these run period. For this reason, t_0 is frequently determined per 10 runs.

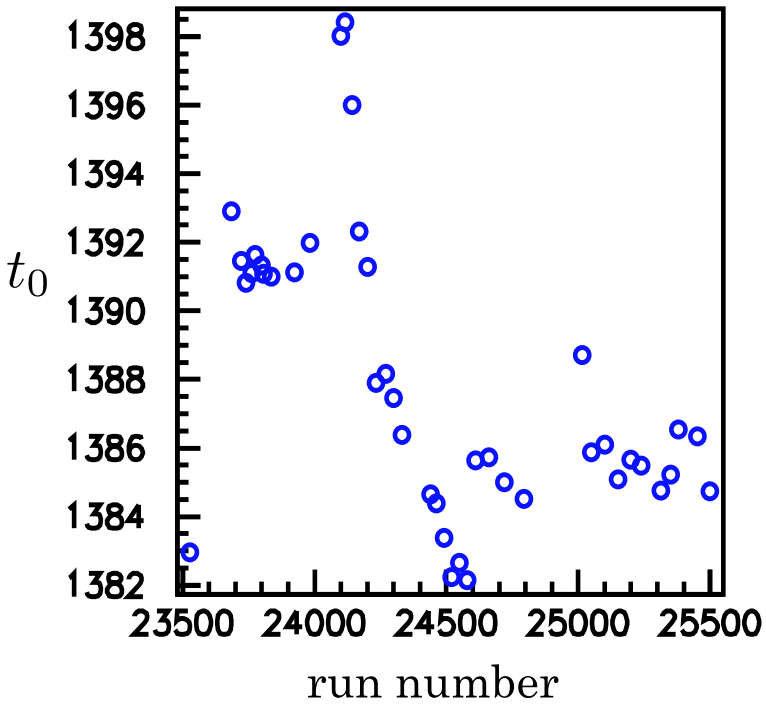

Figure 3.2: Drift chamber TDC t_0 as a function of run number

The drift time t_{drift} is translated to the drift length x_{drift}(x-t curve) as

$$x_{drift} = c_1 t_{drift} + c_2 t_{drift}^2 + c_3 t_{drift}^3 \tag{3.2}$$

where c_1,c_2, and c_3 are the parameters for the x-t curve. But the problem of t_0 fluctuation and noises come from the limited depth number of pulses as mentioned before, the resolution of drift chamber get worth.

Consequently, to improve this problem, x_{drift} is modified as

$$x_{drift} = c_1 t_{drift} + c_2 t_{drift}^2 + c_3 t_{drift}^3 + c_4 \tag{3.3}$$

where, c_4 is new parameter for this purpose.

Fig.3.3 shows the 4-parameters fit results for x-t curve. Since the low width noise, The resolution of position at the far from sense wire is not good. New parameter c_4 correct the discrepancy in original position. Table 3.1 shows the resolution of drift chambers for Long-LH_2 and the previous short LH_2. Since the noisy signal, the resolution of drift chamber is worth than previous experiments. Nevertheless, as seen in Fig.3.4,3.5 which shows the number of outlier and χ^2 probability (Sec.3.4.4) respectively, the tracking efficiency and quality become acceptable after this study.

Table 3.1: Resolution of Drift chamber. Each row shows the resolution at the previous experiment (Short-LH2) and this study(Long-LH2), respectively.

Plane	DC1X	DC1X′	DC1U	DC1U′	DC1V	DC1X″
Short LH_2	.205	.212	.202	.198	.239	.228
Long LH_2	.240	.258	.218	.212	.233	.218
Plane	DC2X	DC2X′	DC2U	DC2U′	DC2V	
Short LH_2	.187	.186	.195	.195	.300	
Long LH_2	.266	.265	.270	.271	.387	
Plane	DC3X	DC3X′	DC3U	DC3U′	DC3V	
Short LH_2	.204	.204	.199	.198	.278	
Long LH_2	.281	.279	.280	.278	.379	

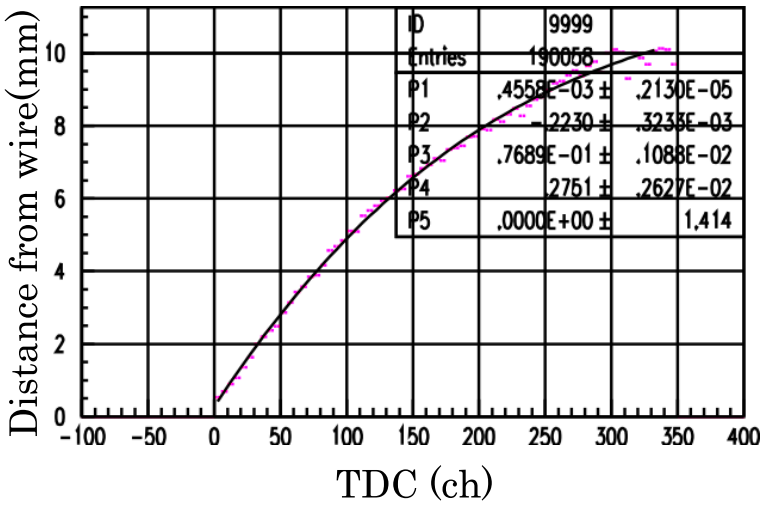

Figure 3.3: Drift chamber TDC x-t curve. Solid line shows the result of 4-parameter polynomial function fit.

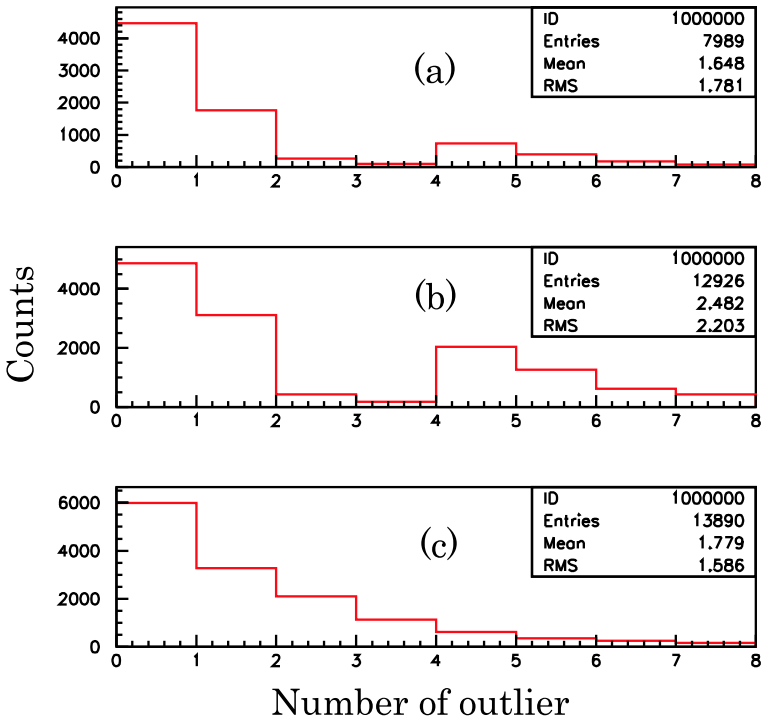

Figure 3.4: Number of Outlier for (a) short LH_2, (b) Long LH_2(original) and (c) Long LH_2 (after this study) respectively.

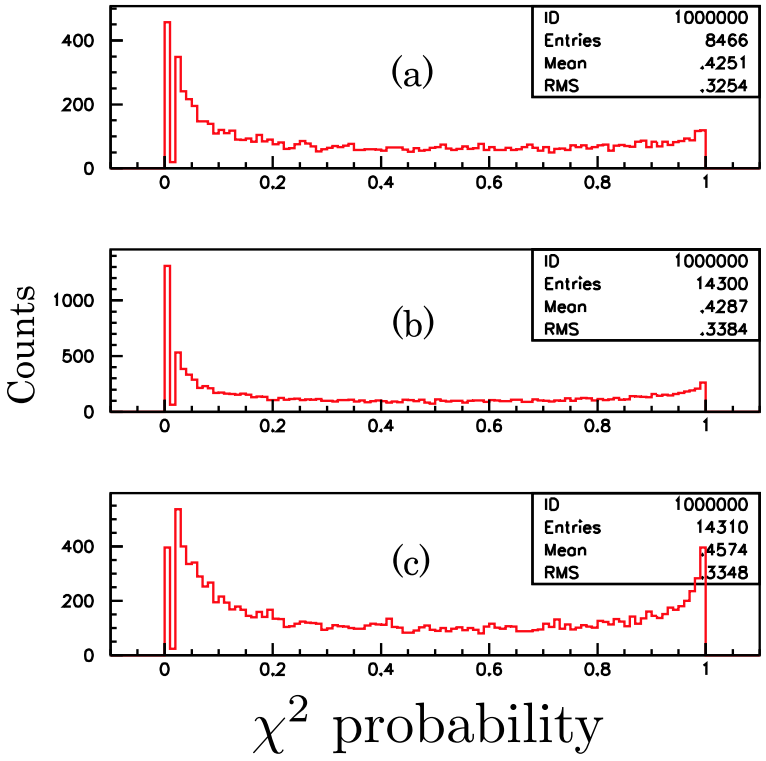

Figure 3.5: χ^2 probability for (a) short LH_2, (b) Long LH_2(original) and (c) Long LH_2 (after this study) respectively.

3.4 Event selections

The $\phi \to K^+K^-$ decay mode was used to discriminate photo-production of ϕ mesons. In this section, definitions of several selections to identify photoproduction of ϕ meson from deuteron are discussed.

3.4.1 Run selection

The first selection of the analysis is the choice of good condition runs. This experiment was carried out from May 2002 to Jun 2003. Each data taking time period is about a few hour per 1 run, and the total run number is 1309 for deuteron target(LD_2) and 767 for hydrogen(LH_2) respectively. These run data also contain such as the detector calibration study run or junk run, in which troubles of data taking system have happened. After rejection of above runs, the total number of run is 1283 for deuteron 746 for hydrogen.

3.4.2 Number of track

The number of charged particles was required to be larger than 1 for $\phi \to K^+K^-$ event. Table 3.2 shows the number of events survived this cut.

Table 3.2: Number of tracks

Cuts	LD2		LH2	
	Horz	Vert	Horz	Vert
ALL	4.64×10^8		2.26×10^8	
	2.31×10^8	2.34×10^8	1.12×10^8	1.14×10^8
1	74,940,610	74,611,069	35,663,869	35,814,204
2	3,537,920	3,173,369	1,413,582	1,338,629
≥3	73,842	71,408	30,602	29,796
Total	3,611,762	3,244,777	1,444,184	1,368,425
	6,856,539		2,736,850	

3.4.3 Particle identification

Particle identify was made by using reconstructed mass. Mass of charged particle m is determined with momentum p, a path length L, and a time of flight T_{TOF} as

$$\begin{aligned} m^2 &= E^2 - p^2 = p^2\left\{\left(\frac{E}{p}\right)^2 - 1\right\} = p^2\left(\frac{1}{\beta^2} - 1\right) \\ \beta &= \frac{L/T_{TOF}}{c} \\ T_{TOF} &= T_{STOP} - T_{START} \end{aligned} \tag{3.4}$$

where β is a velocity of the particle in unit of the speed of the light. The T_{STOP} is determined by the time of the TOF wall counters, T_{START} is determined by the RF signals.
The reconstructed mass resolution $\sigma(m^2)$ was parameterized as

$$\sigma(m^2)^2 = 4m^2(\sigma_{ms}^2(1+(m/p)^2) + \sigma_{spe}^2 p^2) + 4p^2(p^2+m^2)(\sigma_{TOF}(c/L))^2 \tag{3.5}$$

where σ_{ms} is a contribution from the multiple scattering in momentum measurement. The σ_{spe} and σ_{TOF} are resolution of angle measurement by the spectrometer and time-of-flight resolution. c stands for the speed of light. Fig 3.6 shows $\sigma(m^2)$ distribution with each momentum p. The resolution $\sigma(m^2)$ is calculated by width of a Gaussian function fitted to the measured m^2 distribution. Solid line shows the parameterization in Eq. 3.5 with σ_{ms}, σ_{spe} estimated by Monte Carlo simulation. The average resolution of the TOF counter (σ_{tof}) was measured to be 175 psec in real data [33]. Typical mass resolution is 30 MeV for 1 GeV/c Kaon.

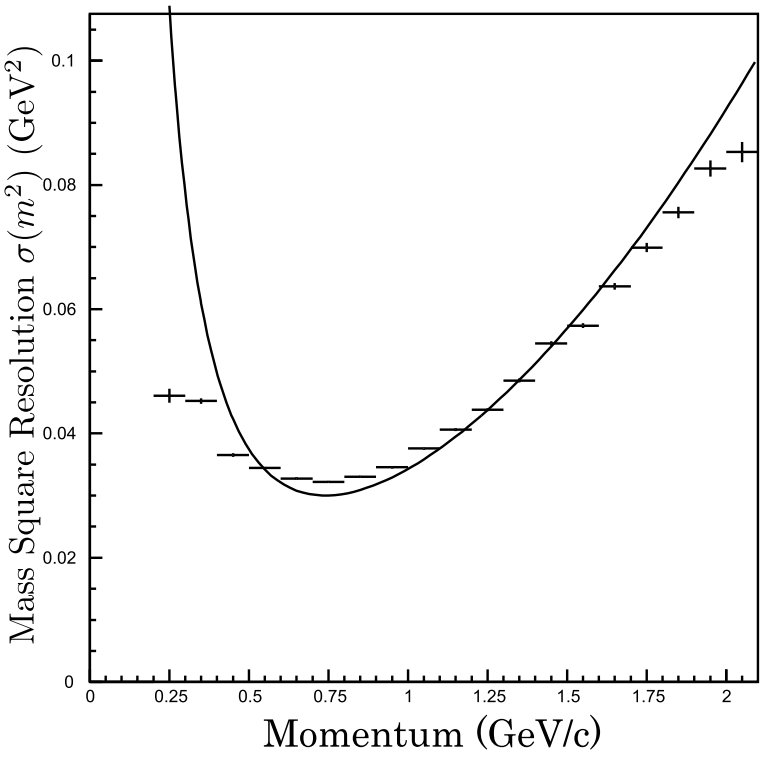

Figure 3.6: Momentum dependence of mass square resolution for deuteron. Solid line shows the estimated mass square resolution with Eq.3.5

The reconstructed mass distributions for positive charged particles and negative charged particles are shown in Fig. 3.7. The PID cut points are shown in Fig. 3.8. The cut points for $K^{\pm}$ and proton were defined as $4\sigma(m^2)$ in Eq.3.5 for the particle momentum below 1 GeV/c, $\sigma(m^2)$ also depends on momentum and is typical 25 MeV for momentum 1 GeV/c Kaon. Fig 3.8 shows two dimensional plot between measured mass square m^2 and measured momentum divided by charge (p/q). Solid line indicates the boundaries for kaon identification. Summary of PID cut is listed in Table 3.3.

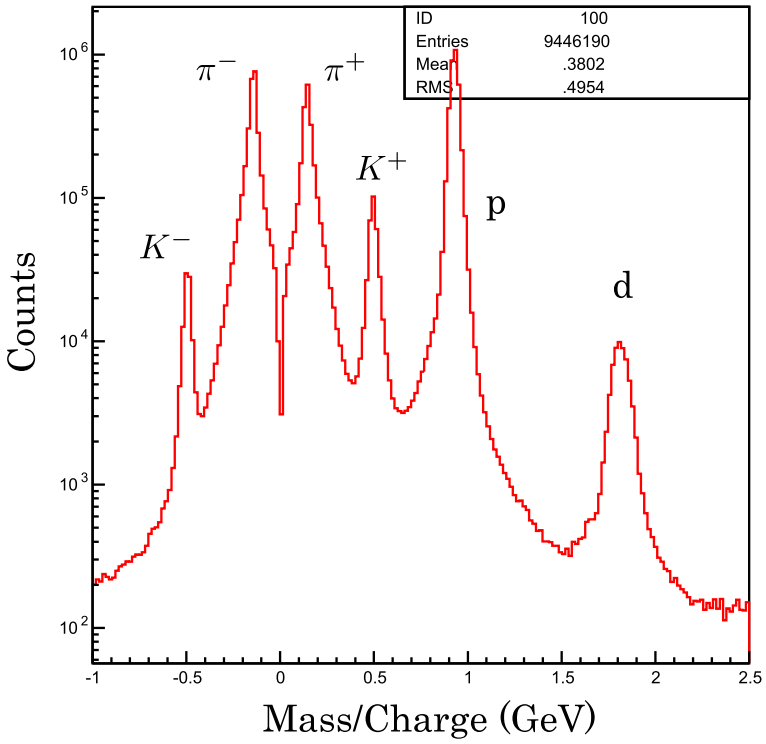

Figure 3.7: Reconstructed mass spectrum

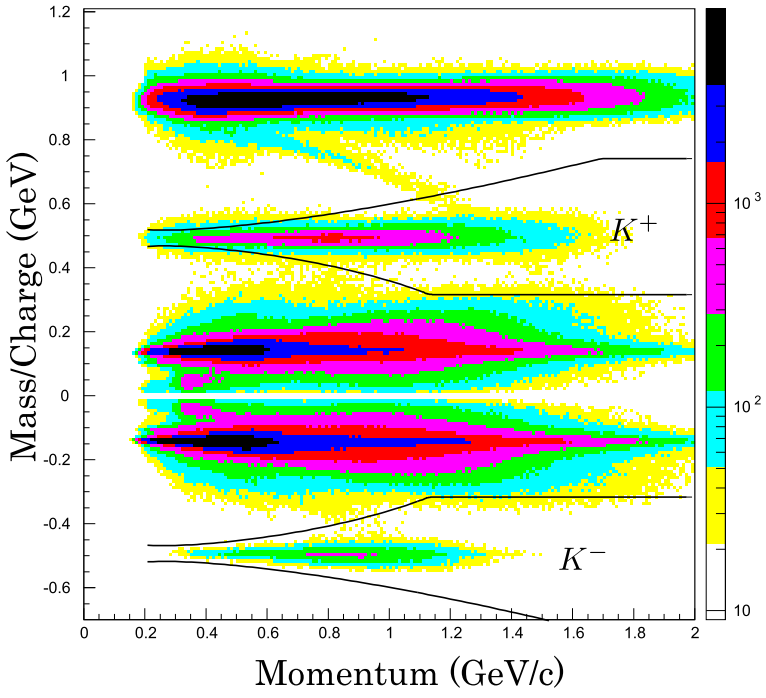

Figure 3.8: Particle identification. Solid line shows kaon identification boundaries

Table 3.3: Summary of PID cut

Cuts	LD2		LH2	
	Horz	Vert	Horz	Vert
# of track $\geq$2	3,611,762	3,244,777	1,444,184	1,368,425
K^- PID	84,807	72,185	33,635	28,918
K^+ PID	23,367	20,239	8,328	8,186
Total K^+K^-	23,367	20,239	8,328	8,186
	43,616		16,514	
p PID	752	712	363	411
Total K^+K^-p	752	712	363	411
	1,464		774	

3.4.4 Decay-in-flight cuts

Next, the event sample was applied decay-in-flight cut(DIF) which exclude the event such as $K \to \mu + \nu$ decay event. The decay-in-flight cut was consisted of three parts described below

Consistency of TOF hit

It is required that a hit TOF counter corresponding to the prediction from the track. When the difference of y position was greater than 80 mm or difference of the TOF slat number was greater than 1, those tracks were rejected by this cut.

Number of outlier

If hit of tracking chambers were deviated from the expected trajectories more than the resolution, The hit was judged as a background hit (outlier) and removed from the tracking. Decay-in-flight event had a track with a large number of outliers when it decayed in the middle of tracking volume (between SVTX and DC3). When the number of outliers were greater than 6, the tracks were rejected in the analysis.

χ^2 probability

The χ^2 probability is used to eliminate Decay-in-flight event. The χ^2 probability is defined as below,

$$Prob(\chi^2, ndf) = \int_{\chi^2}^{\infty} f(\chi\prime^2, ndf) d\chi\prime^2 \tag{3.6}$$

where f is the standard χ^2 distribution with number of degree of freedom ndf. The χ^2 probability of reconstructed track was required to be greater than 0.02.

The decay-in-flight cuts were applied not only for K mesons but also for proton tracks which have large reconstruction error due to mis-measurements of track position, such as mis-solving of left-right ambiguity of the drift chamber hits caused by the multiple scattering.

Summary of Decay-in-flight cut is listed in Table 3.4.

Table 3.4: Summary of DIF cut

Cuts	LD2		LH2	
	Horz	Vert	Horz	Vert
# of track $\geq$2	3,611,762	3,244,777	1,444,184	1,368,425
K^+K^- PID	23,367	20,239	8,328	8,186
Total DIF cut K^+K^-	19,943	17,577	7,145	7,189
	37,620		14,334	
K^+K^-p PID	752	712	363	411
Total DIF cut K^+K^-p	582	567	290	304
	1149		594	

3.4.5 The vertex cut

The vertex point of K^+K^- tracks is regarded as the produced position of ϕ meson, because of ϕ meson decays immediately. The distribution of the K^+K^--track vertex along with the z-coordinate after the DIF cuts are shown in Fig. 3.9. The events from reactions at the LH_2 target were clearly separated from the events from reactions at the start counter. A cut on the z-vertex ($-1120 < z < -885$ mm) was applied to select events from the LH_2 and LD_2 target. In Fig. 3.9 the previous (Short LH_2) experiment result[36] are also figured.

Fig. 3.10 shows the two-dimensional scatter plot of the events in xy plane. In order to select the events that come from target, cuts $-30. \leq x \leq 30.$ and $-30. \leq y \leq 30.$ was also applied.

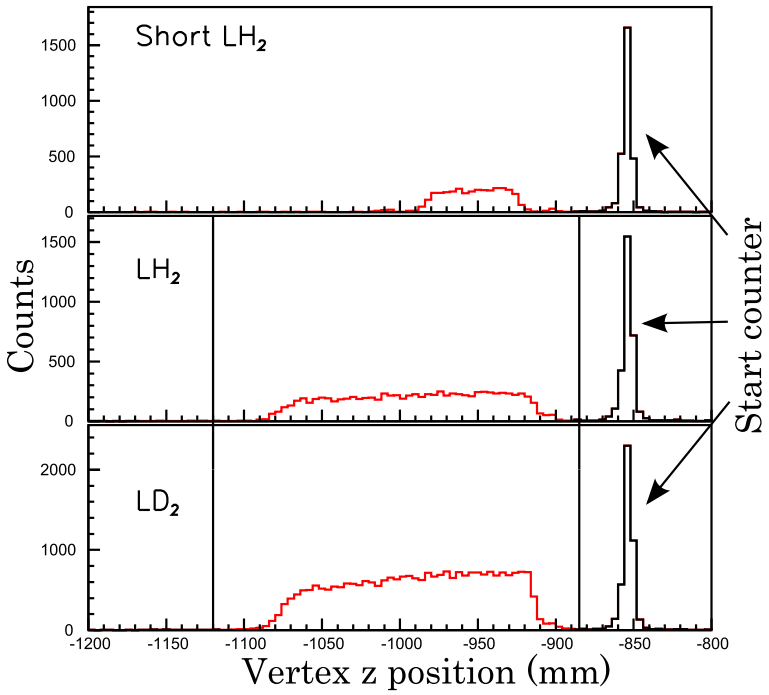

Figure 3.9: z-vertex distributions of the K^+K^- tracks

Summary of vertex cut is listed in Table 3.5.

3.4.6 Selection for valid Tagger hit

To evaluate the incident photon energy, Tagging counter signals were used. There also exist the event in which number of tagger counter hit (ntag) equal 0, or ntag ≥ 2. When the ntag greater than 1, it is necessary to select a hit. For photon energy calibration study [29], using estimation of Tagger SSD hit region from fired Plastic Scintillator channels, incident photon energy E_γ was also calculated at ntag ≥ 2. Fig.3.11 shows photon energy distribution both the ntag=1 and ntag ≥ 1 event. In this study, we required the tagger hit selection function[29] itagc.f ≥ 1, This function returns the positive value when we successfully calculated the photon energy. Summary of Tagger cut is listed in Table 3.6.

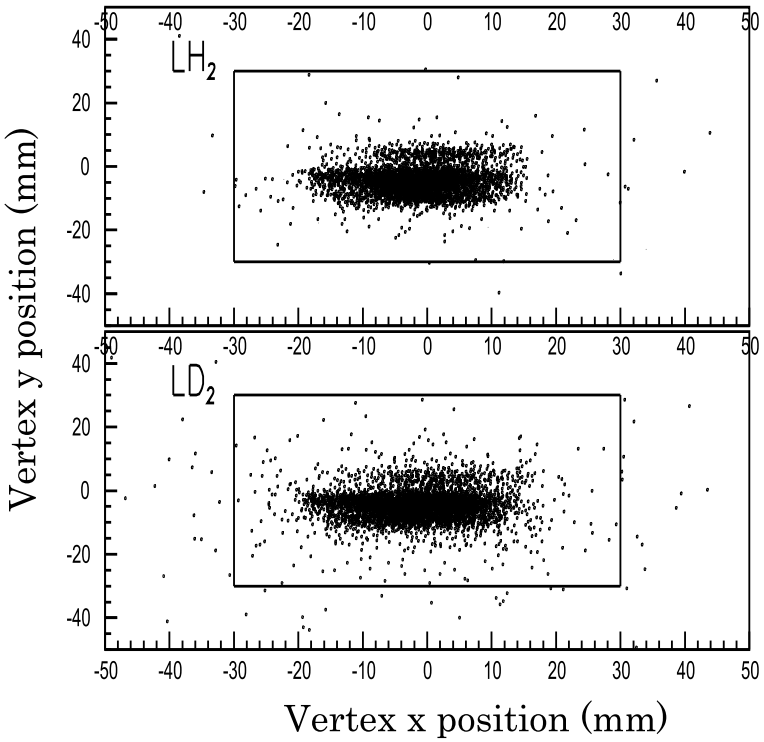

Figure 3.10: y-vertex versus the x-vertex two dimensional scatter plot of the K^+K^-. Because the beam profile are shifted during run period, y-vertex distribution is separated.

3.4.7 Invariant mass

The events of ϕ-meson photoproduction were identified using the K^+K^- invariant mass distribution. K^+K^- invariant mass($m_{K^+K^-}$) is described as

$$m^2_{K^+K^-} = \left(\sqrt{m^2_{K^+} + p^2_{K^+}} + \sqrt{m^2_{K^-} + p^2_{K^-}}\right)^2 - |p_{K^+} + p_{K^-}|^2 \tag{3.7}$$

where m_K is Kaon mass, p_{K^+} and p_{K^-} are measured K^+ and K^- momenta respectively. Fig. 3.12 shows the K^+K^- invariant mass distributions. The events of ϕ-meson photoproduction

Table 3.5: Summary of vertex cut

Cuts	LD2		LH2	
	Horz	Vert	Horz	Vert
DIF cut	19,943	17,577	7,145	7,189
Vertex cut K^+K^-	16,987	14,672	5,287	5,214
	31,659		10,501	
K^+K^-p DIF cut	587	567	290	304
Vertex cut K^+K^-p	471	447	217	220
	918		437	

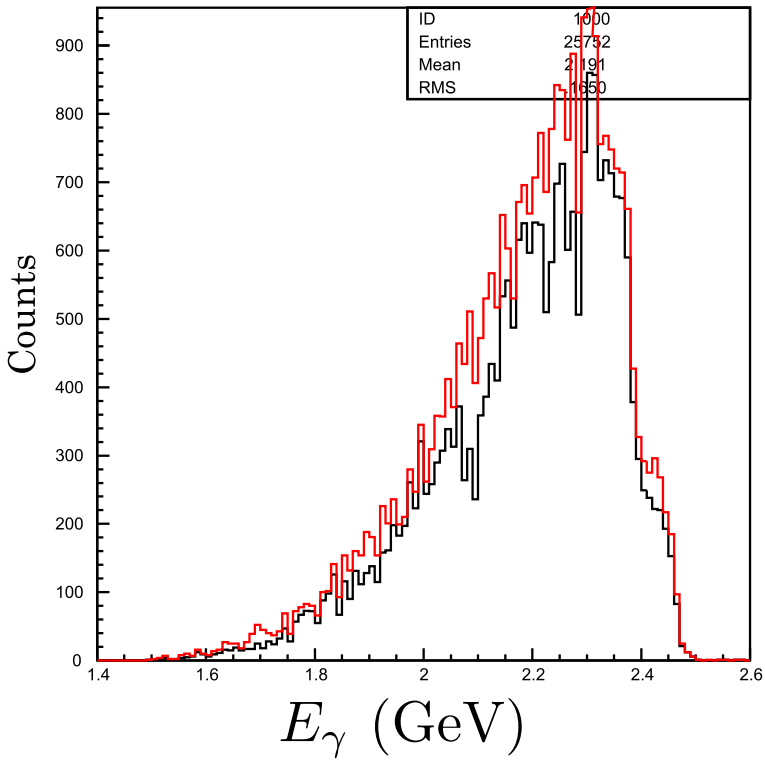

Figure 3.11: Distribution of photon energy for K^+K^- events. Black histogram shows ntag=1 event only, red histogram contains ntag≥2 event

were clearly identified as a sharp peak at the mass of ϕ-meson. The cut condition $|m_{K^+K^-} - m_\phi| \leq 10$ MeV is required for the K^+K^- invariant mass. Where, m_ϕ is PDG value of ϕ meson mass 1019.456 ± 0.020 and width Γ is 4.26 ± 0.05 MeV respectively [40].

There was a small amount of backgrounds. Fig.3.13 shows a Invariant mass distribution fitted by a Gaussian-convoluted Breit-Wigner function $F_{BW}(m,\sigma)$ and non-resonant K^+K^- background event N_{BG}. The invariant mass distribution was fitted with following parameterization,

$$N(m) = P1 * F_{BW}(m,\sigma) + P3 * N_{BG}$$

and, $F_{BW}(m,\sigma)$ is,

$$F_{BW}(m,\sigma) = \frac{1}{\sqrt{2\pi\sigma^2}} \int_{2m_K}^{\infty} dm' \exp \frac{-(m'-m)^2}{2\sigma^2} \frac{\Gamma/2\pi}{(m'-m_\phi)^2 + (\Gamma/2)^2}$$

where, P1,P2(=σ),P3 are fitting parameters, m is K^+K^- invariant mass, m_K is the K meson mass, m_ϕ is the mass of ϕ meson and Γ is width of the ϕ meson described above. The K^+K^- invariant mass resolution σ (= P2) was found to be 1.54 ± 0.06 MeV. Since the ϕ meson natural width is $\sigma = \Gamma/2.35 = 1.81$ MeV, the cut points on the K^+K^- invariant mass (1.009 ∼ 1.029) is greater than 2-σ. The origin of this background could be a non-resonant K^+K^-p production and/or the $f_0(980)$ photoproduction. The mass of the f_0 is below the two-kaon threshold but because of large width ∼ 60 MeV, the tail of the resonance can be the background events in the present analysis [41]. These backgrounds were subtracted in the data analysis. The procedure

Table 3.6: Summary of Tagger cut

Cuts	LD2		LH2	
	Horz	Vert	Horz	Vert
Vertex cut	16,987	14672	5,287	5,214
Tagger cut K^+K^-	139,42	12154	4399	4373
	26,096		8772	
K^+K^-p Vertex cut	471	447	217	220
Tagger cut K^+K^-p	374	376	186	176
	750		362	

of the background subtraction is described in Section 3.7.
Summary of invariant mass cut is listed in Table 3.7.

Table 3.7: Summary of invariant mass cut

Cuts	LD2		LH2	
	Horz	Vert	Horz	Vert
Invariant mass cut	10,076	9,050	3,027	3,078
	19,126		6,105	
Invariant mass cut (K^+K^-p)	215	221	104	116
	436		220	

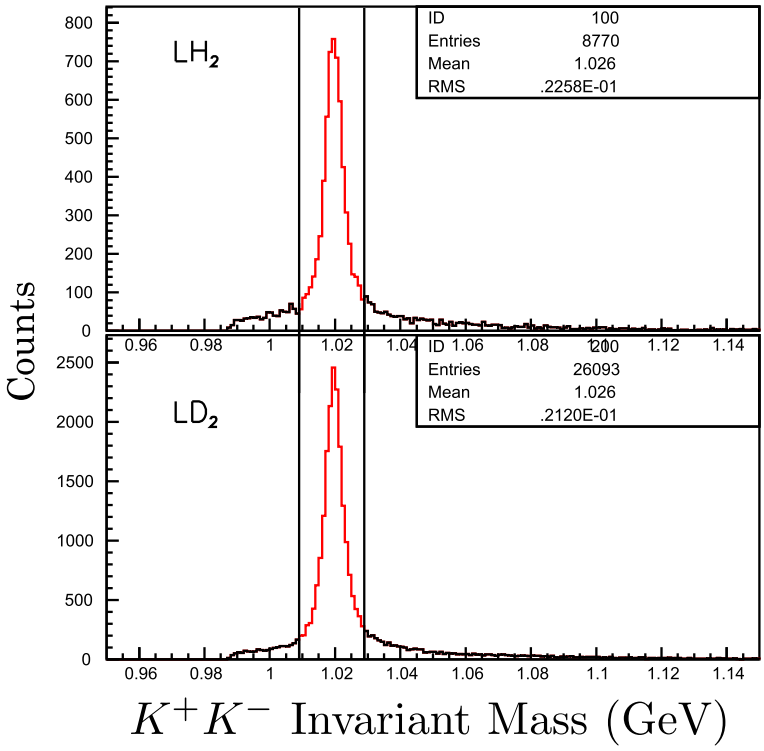

Figure 3.12: The K^+K^- invariant mass distribution at LH_2 and LD_2 target. The vertical line shows ± 10 MeV positions from the ϕ meson mass.

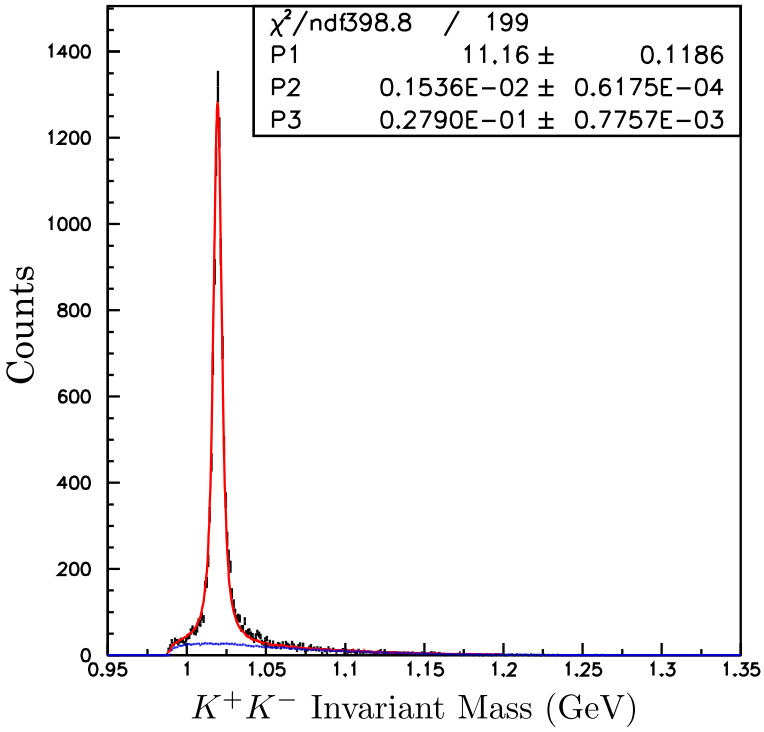

Figure 3.13: The K^+K^- invariant mass distribution Red histogram is results of fit. Blue histogram shows a non-resonant K^+K^- event.

3.4.8 Missing mass cut

After determining E_γ, the events from the reaction $\gamma + p(n) \to K^+K^-p(n)$ was identified with a cut on the missing mass distribution for the $\gamma p \to K^+K^-X$ process (MMp).

The missing mass distribution for the $(\gamma, K^+K^-)X$ is shown in Fig. 3.14. A sharp peak at the proton mass was observed in the spectrum for LH_2. On the other hand, for LD_2 case, a peak width get wider than LH_2 case because of the Fermi-momentum in the deuteron. The missing mass resolution for LD_2 was found to be about $\sim$ 28 MeV.

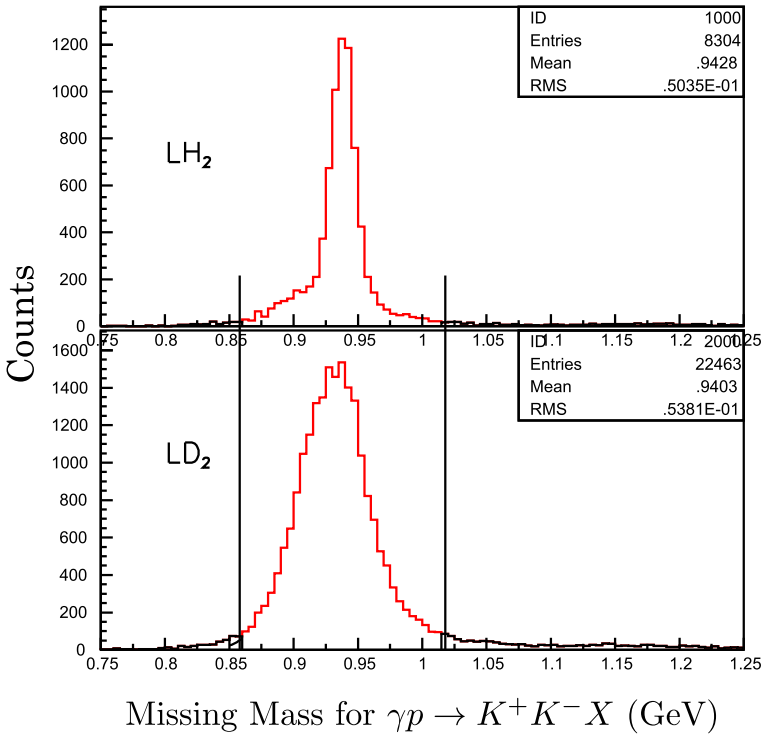

Figure 3.14: (a) Missing mass distribution for $\gamma p(n) \to K^+K^-X$ reaction LH_2 target and LD_2 target respectively.

In order to select the $K^+K^-p(n)$ final state, a cut on the missing mass spectrum $|MMp - M_p| \leq 80$ MeV was applied for the LH_2 and LD_2 target. Where M_p is PDG proton mass. The cut points corresponded to $\sim 3\sigma$ of the missing mass resolution.

Summary of missing mass cut is listed in Table 3.8.

Table 3.8: Summary of missing mass cut

Cuts	LD2		LH2	
	Horz	Vert	Horz	Vert
missing mass cut	9,418	8,372	2.913	2,945
	17,790		5,858	
missing mass cut (K^+K^-p)	144	156	89	94
	300		183	

3.4.9 Summary of ϕ selection cuts

The number of events after the various ϕ selection cuts discussed above are summarized in Table. 3.9 and 3.10 together with rejection factors. The rejection factor is defined as

$$Rejection\ factor = \frac{number\ of\ events\ before\ cut}{number\ of\ events\ after\ cut}$$

Table. 3.9 and 3.10 show the K^+K- mode and K^+K^-p mode result respectively.

Table 3.9: Summary of ϕ selection cut. Each cell shows the number of survived events in the cut together with rejection factor in the parentheses.

Cuts	LD2		LH2	
	Horz	Vert	Horz	Vert
Tirggered	2.34×10^8	2.31×10^8	1.14×10^8	1.12×10^8
ntrk≥2	3,537,920 (66.14)	3,173,369 (72.79)	1,413,582 (80.65)	1,338,629 (83.67)
K^- PID	84,807 (41.72)	72,185 (43.96)	33,635 (42.03)	28,918 (46.29)
K^+ PID	23,367 (3.63)	20,239 (3.57)	8,328 (4.04)	8,186 (3.53)
DIF	19,943 (1.17)	17,577 (1.15)	7,145 (1.17)	7,189 (1.14)
Vertex	16,987 (1.17)	14,672 (1.20)	5,287 (1.35)	5,214 (1.38)
Tagger	13,942 (1.22)	12,154 (1.21)	4,399 (1.20)	4,373 (1.19)
Invariant Mass	10,076 (1.38)	9,050 (1.34)	3,027 (1.45)	3,078 (1.42)
MMp	9,418 (1.07)	8,372 (1.08)	2,913 (1.04)	2,945 (1.05)
analyzed ϕ event	17,790		5,858	

Table 3.10: Summary of ϕ selection cut for K^+K^-p event. Each cell shows the number of survived events in the cut together with rejection factor in the parentheses.

Cuts	LD2		LH2	
	Horz	Vert	Horz	Vert
Tirggered	2.34×10^8	2.31×10^8	1.14×10^8	1.12×10^8
ntrk$\geq$3	73,842 (3168.9)	71,408 (3234.9)	30,602 (3725.2)	29,796 (3758.9)
K^+K^-p PID	752 (98.2)	712 (100.3)	363 (84.3)	411 (72.5)
DIF	582 (1.29)	567 (1.26)	290 (1.25)	304 (1.35)
Vertex	471 (1.24)	447 (1.27)	217 (1.34)	220 (1.38)
Tagger	374 (1.26)	376 (1.19)	186 (1.16)	176 (1.25)
Invariant mass	215 (1.74)	221 (1.70)	104 (1.79)	116 (1.52)
MMp	144 (1.49)	156 (1.42)	89 (1.17)	94 (1.23)
analyzed ϕ events	300		183	

3.5 Incoherent and coherent ϕ photo-production

For the Fermi momenta of the nucleon target inside deuteron, the kinematical energy for quasi-free like incoherent $K^+K^- + p(n)$ is not precisely determined by using incident photon energy (E_γ,P_γ). In order to investigate this effect, "minimum momentum spectator approximation" developed in Ref.[42] is applied to select out the quasi-free incoherent events. By Givining the information of incident photon energy(E_γ) and momenta of detected kaon pairs (p_{KK}), the missing energy (E_{miss}) and missing momentum (p_{miss}) in the final state can be determined as the total energy and momentum of an assumed two-nucleon system(M_{pn}). The momentum of a spectator nucleon in the laboratory system has its minimum magnitude if the direction of momentum is anti-parallel to that of the total missing momentum. This configuration is assumed in the "minimum momentum spectator approximation". The minimum momentum, p_{min}^{spec}, is defined as the component of the spectator momentum in the direction of the missing momentum.

$$
\begin{aligned}
p_{miss} &= p_\gamma - p_{KK} \\
E_{miss} &= E_\gamma + M_D - E_{KK} \\
M_{pn}^2 &= E_{miss}^2 - p_{miss}^2 \\
p_{cm} &= \frac{\sqrt{(M_{pn}+M_p+M_n)(M_{pn}-M_p+M_n)(M_{pn}+M_p-M_n)(M_{pn}-M_p-M_n)}}{2M_{pn}} \\
E_{cm}^2 &= M_{p(n)}^2 + p_{cm}^2 \\
p_{min}^{spec} &= \gamma(\beta E_{cm} - p_{cm})
\end{aligned}
\tag{3.8}
$$

where, M_p and M_n are proton and neutron mass respectively, $p_{miss} = \beta E_{miss}$, $\gamma M_{pn} = E_{miss}$ are defined.

Fig. 3.15 shows p_{min}^{spec} and target nucleon momentum in Monte-Carlo simulation. Monte-Carlo study shows that the p_{min}^{spec} correlates strongly with Fermi momentum of target nucleon in photon beam direction within our acceptance and p_{min}^{spec} could be used for estimating Fermi momenta of target nucleons.

Fig. 3.16 shows p_{min}^{spec} distribution in Monte-Carlo for the incoherent and coherent process respectively. The incoherent p_{min}^{spec} distribution mostly distribute around 0. And the width of distribution is 44.0 (MeV) using Gausian Function fitting. On the other hand, the coherent one is concrete lager than +0.1 GeV/c, because the both proton and neutron move with the same velocity.

Fig. 3.17 shows missing mass distribution for $\gamma + D \rightarrow \phi X$ (MM_D) with the coherent and incoherent Monte-Carlo simulation. Fitting for MM_D using the coherent and incoherent simulation are developed in Ref. [8]. In this plot, the coherent event are distributed around the douteron mass (1.875 GeV) and incoherent event are shown in higer energy side. To exclude this coherent event, we select the p_{min}^{spec} variable. The effect of p_{min}^{spec} are showed in Fig. 3.18. This plot represents the missing mass distribution for $\gamma + D \rightarrow \phi X$ (MM_D)(Upper histogram). And also, MM_D distribution limited to the $p_{min}^{spec} \geq 0.09$ GeV is discribed(Lower histogram). Thus, the coherent or incoherent process are possibly selected with the p_{min}^{spec} value. Of course, actual magnitude of the spectator nucleon momentum should be larger than p_{min}^{spec}, but we can

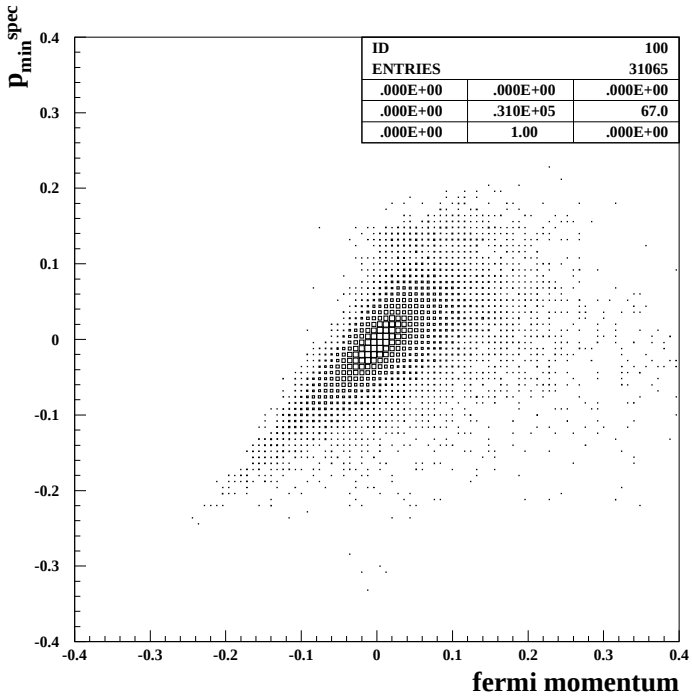

Figure 3.15: p_{min}^{spec} and target nucleon momentum in Monte-Carlo simulation

reject event with a large absolute value of p_{min}^{spec}. In this analysis the cut point for the incoherent and coherent process is set to $p_{min}^{spec} = 90$ MeV which correspondings to 2-σ of incoherent event. But of course, there are the contamination from coherent event(See Appendix.C).

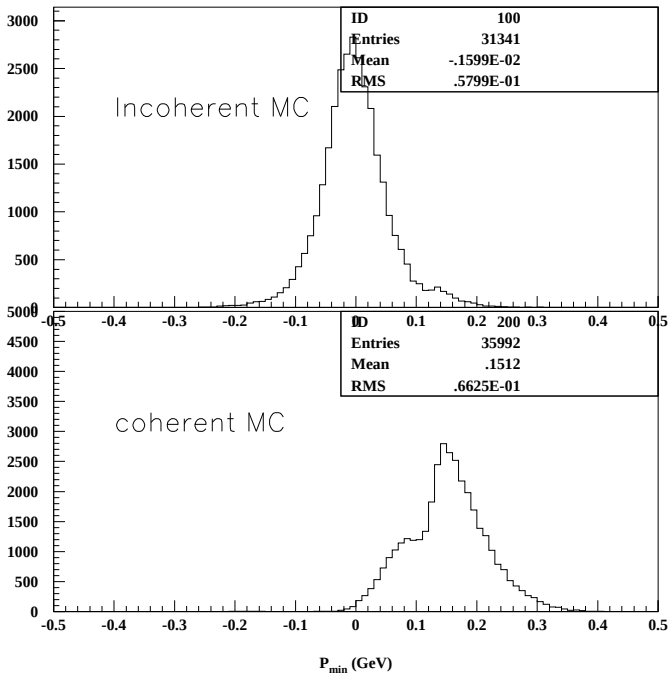

Figure 3.16: p_{min}^{spec} distribution in Monte-Carlo. Incoherent and Coherent process are shown respectively.

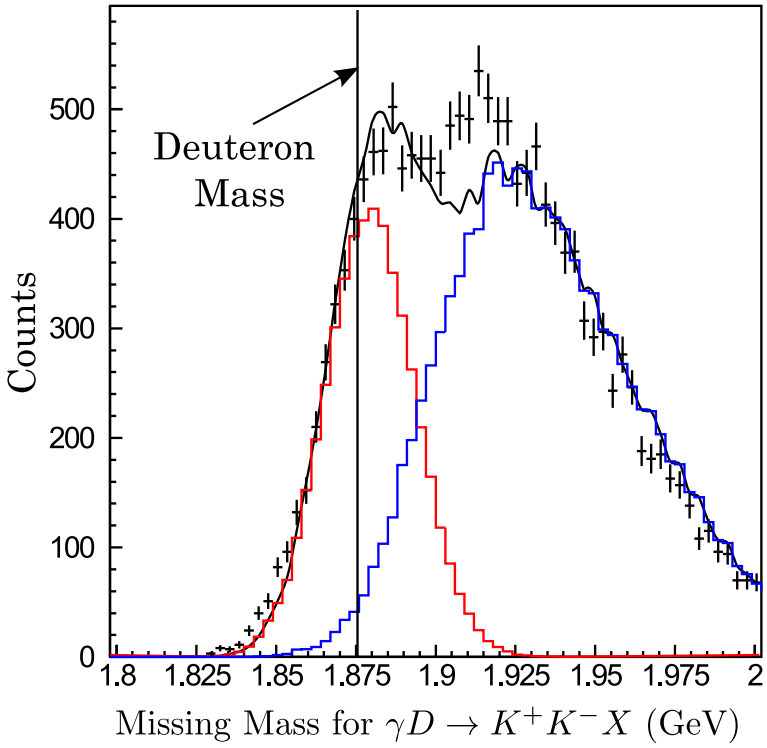

Figure 3.17: MM_D distribution for experimental data (black points) with Monte-Carlo simulation (blue line) and coherent (red line)

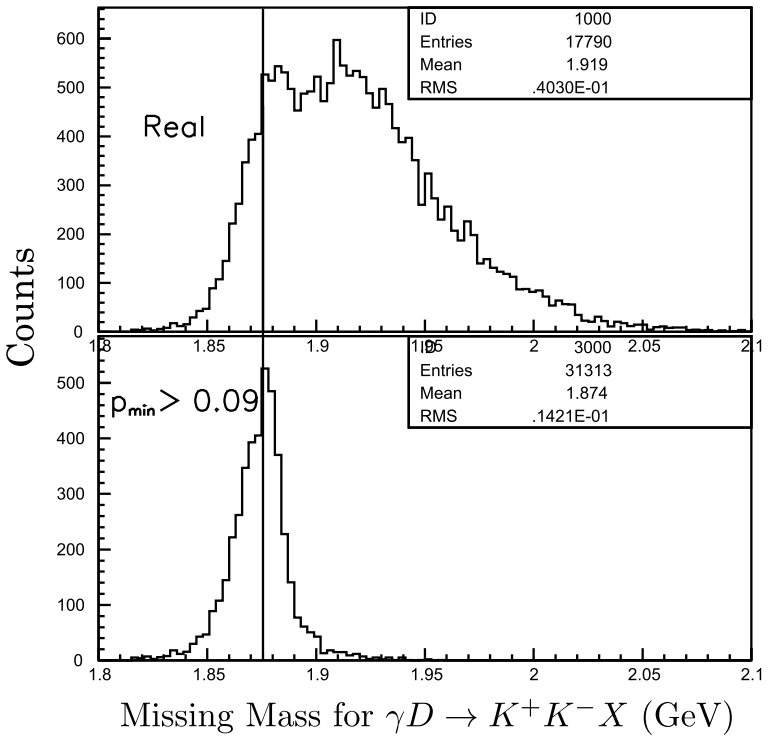

Figure 3.18: MM_D distribution for experiment data (Real) event through the ϕ selection cut, and lower one is selected $p_{min}^{spec} \geq 90$ MeV event. Vertical line shows deuteron mass

3.6 acceptance calculation

The acceptance for the LEPS spectrometer was obtained by the Monte Carlo simulation for ϕ photoproduction. The same selection cuts and analysis criteria, which were described in Section 3.4, were applied for the Monte Carlo data. The acceptance was given by the number of accepted events divided by the number of generated events in the Monte Carlo simulation.

In the cross section measurement, the data with the horizontal polarization (Horz data) and data with the vertical polarization (Vert data) were merged to make an unpolarized data where any polarization effects were canceled in the first order. Note that there was a difference of the beam profile between the vertical polarization and the horizontal polarization, however dependence of the acceptance on the x and y coordinates of the production point was found to be small. Therefore, the effect of different beam profile was neglected. The cross section from nucleon as a function of momentum transfer t is written as,

$$\begin{aligned} \frac{d\sigma}{dt} &= C\exp(b\tilde{t}) \\ \tilde{t} &= t + |t|_{min}, \end{aligned} \tag{3.9}$$

where C is a constant factor and b is slope parameters. Since the $|t|_{min}$ is kinematical limit of t and depend on E_γ, the variable $\tilde{t}$ is introduced. In this study, b was set to 3.38 GeV^{-2} for incoherent $\gamma N \to \phi N$ process, which calculated the observed t-slope in free proton data which is shown in [36].

The momentum distribution of nucleons inside the deuteron target is modeled by the well-known PARIS potential [39].

The acceptance for the Horz data was different from that for Vert data. The acceptance also depended on the spin density matrix elements. Then, the spin density matrix elements value of incoherent production was introduced as the proton values [36] for nucleon target. In the measurements of the decay angular distributions, the Horz data and the Vert data were analyzed separately.

The incoherent ϕ photoproduction events were generated according to spin density matrix elements ρ and slope b as

$$\begin{aligned} \rho^0_{00} &= 0.069 \\ \rho^0_{1-1} &= 0.039 \\ \rho^1_{1-1} &= 0.19 \\ b &= 3.38 \end{aligned} \tag{3.10}$$

which calculated by ϕ photoproduction from proton[36]. Obviously, when the difference between proton and neutron inside of deuteron is large, the discrepancy of spin density matrics and slope is not negligible. But, it was found that the t distribution and decay asymmetry are reproduced with reasonable accuracy (See Sec 4.1, 4.2).

3.7 Background estimation

The candidate of the background events in $\gamma N \to \phi N$ process are

- non-resonant K^+K^- events.
- contributions from Final State Interaction(FSI).
- $\Lambda(1520)$ production.

In this analysis, the backgrounds is assumed the non-resonant K^+K^-N backgrounds in which no signature of formation of the resonance was seen. Analysis of the backgrounds is described in this section, and the estimation for FSI is described Appendix.(B).

The Monte Carlo simulation for the backgrounds was necessary in order to know the best way of background subtraction. The K^+K^- invariant mass distributions were studied for this purpose.

3.7.1 The Non-resonant K^+K^-N background

A Monte Carlo simulator for the non-resonant K^+K^-N background was obtained by assuming the three-body phase space of the reaction $\gamma N \to K^+K^-N$. Figure 3.19 shows the K^+K^- invariant mass distribution for non-resonant K^+K^- production. Number of background counts in the ϕ signal region was deduced by scaling the simulated background shape to fit the real data. The scaling factor was obtained from sidebands in the K^+K^- invariant mass in both real data and Monte-Carlo data. The background region was defined as $M(K^+K^-) < 1.009$ GeV (left) and $1.039 < M(K^+K^-)$ (right). The ϕ peak region was defined as $1.009 < M(K^+K^-) < 1.029$ GeV (see Section 3.4). Number of background counts N_{BG} in the signal region has been estimated as

$$N_{BG} = \alpha(N^{real}_{left} + N^{real}_{right}) \tag{3.11}$$

$$\alpha = \frac{N^{MC}_{BG}}{N^{MC}_{left} + N^{MC}_{right}} \tag{3.12}$$

where N^{real}_{left}, N^{real}_{left}, N^{MC}_{left} and N^{MC}_{right} are numbers of backgrounds in left and right for real and Monte-Carlo, respectively. In real data, a tail of the Breit-Wigner distribution for the ϕ-meson was also present in sidebands. The leakage of ϕ signal in sidebands was estimated by Monte Carlo simulation for the ϕ photoproduction, and they were 4.5% for left and 6.0% for right(Fig.3.20) which were almost independent of E_γ and t. The numbers of background counts in sidebands (N^{real}_{left}, N^{real}_{right}) were obtained from total numbers of counts in sidebands ($N^{real}_{left} + N^{real}_{right}$) with correction for the leakage of ϕ meson events into sidebands; i.e.

$$N^{real}_{left} \simeq N^{real}_{left} - 0.045 N^{real}_{signal} \tag{3.13}$$

$$N^{real}_{right} \simeq N^{real}_{right} - 0.06 N^{real}_{signal}, \tag{3.14}$$

Where N^{real}_{signal} stands for number of counts in signal region. The number of ϕ-meson signal in the signal region was obtained by subtracting N_{BG} from total number of events in the ϕ signal region (N^{real}_{signal}),

$$N_\phi = N^{real}_{signal} - N_{BG}. \tag{3.15}$$

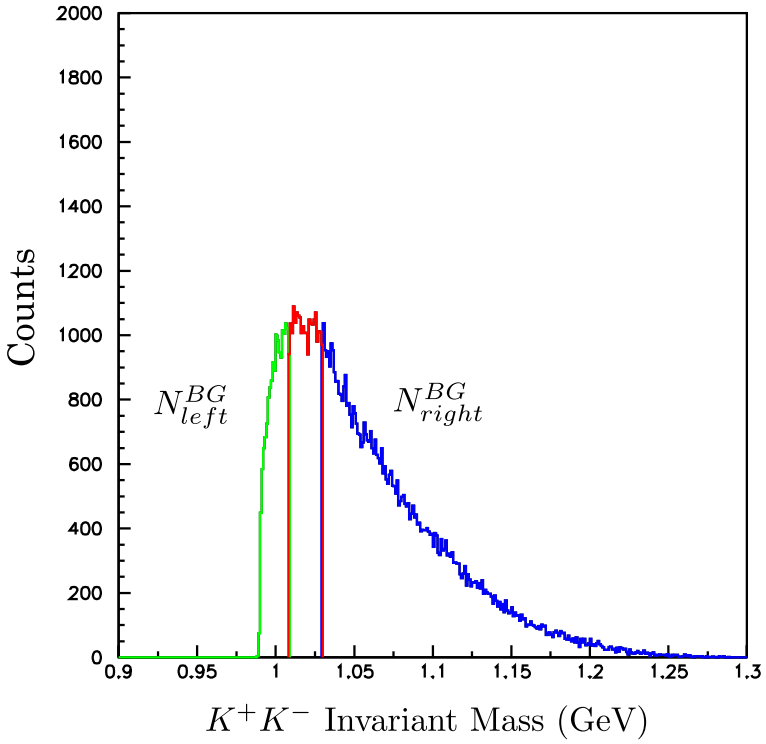

Figure 3.19: Invariant mass distribution for non-resonant K^+K^- (MC). The red histogram shows the event which pass the ϕ selection cut, and the green and blue ones show the events used in the background estimation.

The observed ϕ-meson sample (Section 3.4) was divided into several parts in terms of E_γ, t and decay angles. The backgrounds were subtracted by this method in each sub-sample.

3.7.2 $\Lambda(1520)$ background

The background candidates for ϕ peak signal are not only the non-resonant K^+K^- but also the $\Lambda(1520)$ photo-production on the proton as

$$\begin{aligned} \gamma + p &\rightarrow K^+\Lambda(1520) \\ \Lambda(1520) &\rightarrow K^- + p \end{aligned} \tag{3.16}$$

Figure 3.22 shows the Dalitz plot for K^+K^-p final state. The locus corresponds to the $\Lambda(1520)$ was not clearly visible. A projection of this distribution onto the K^-p invariant mass is shown in Fig.3.23. The $\Lambda(1520)$ peak appears in condition K^+K^- invariant mass (M_{KK}) $\geq$ 1.039 GeV and (M_{KK}) $\leq$ 0.989 GeV. Fig.3.24 shows the number of $\Lambda(1520)$ count. The number of $\Lambda(1520)$ events in ϕ signal region which come from extrapolation is 53 in all E_γ. This value is negligibly-small compared with the ϕ-signal count.

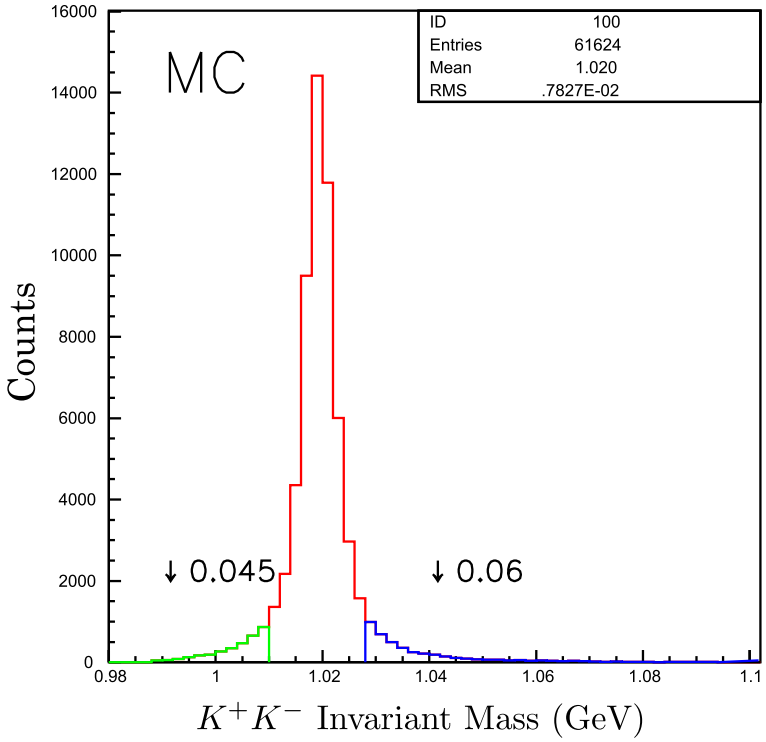

Figure 3.20: Invariant mass distribution for Monte-Carlo K^+K^-. The red histogram shows the ϕ peak signal, and the green and blue ones show ϕ signals in background region.

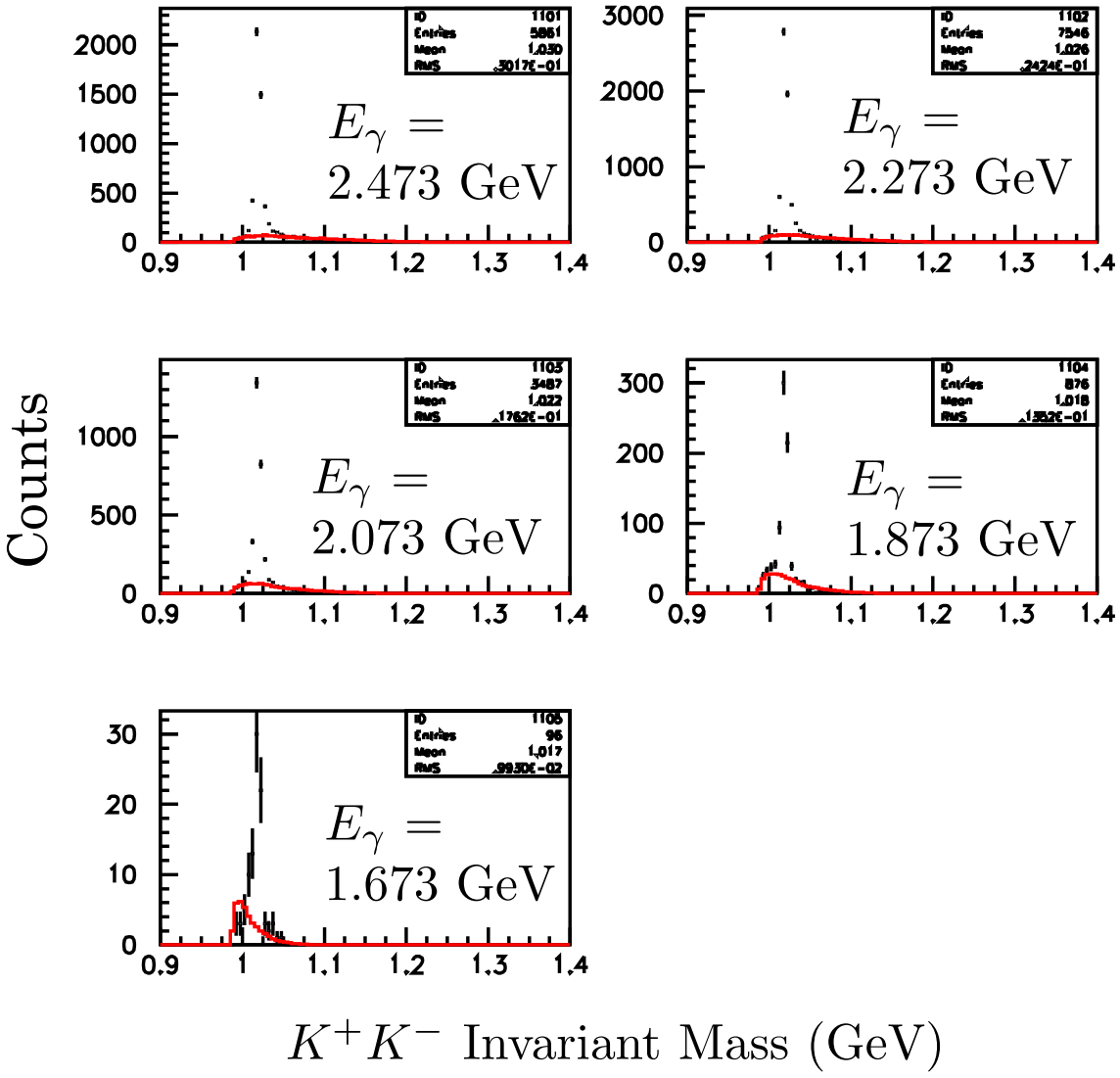

Figure 3.21: The K^+K^- invariant mass distributions for real data and MC simulation. The red curves indicate the estimation of the non-resonant background .

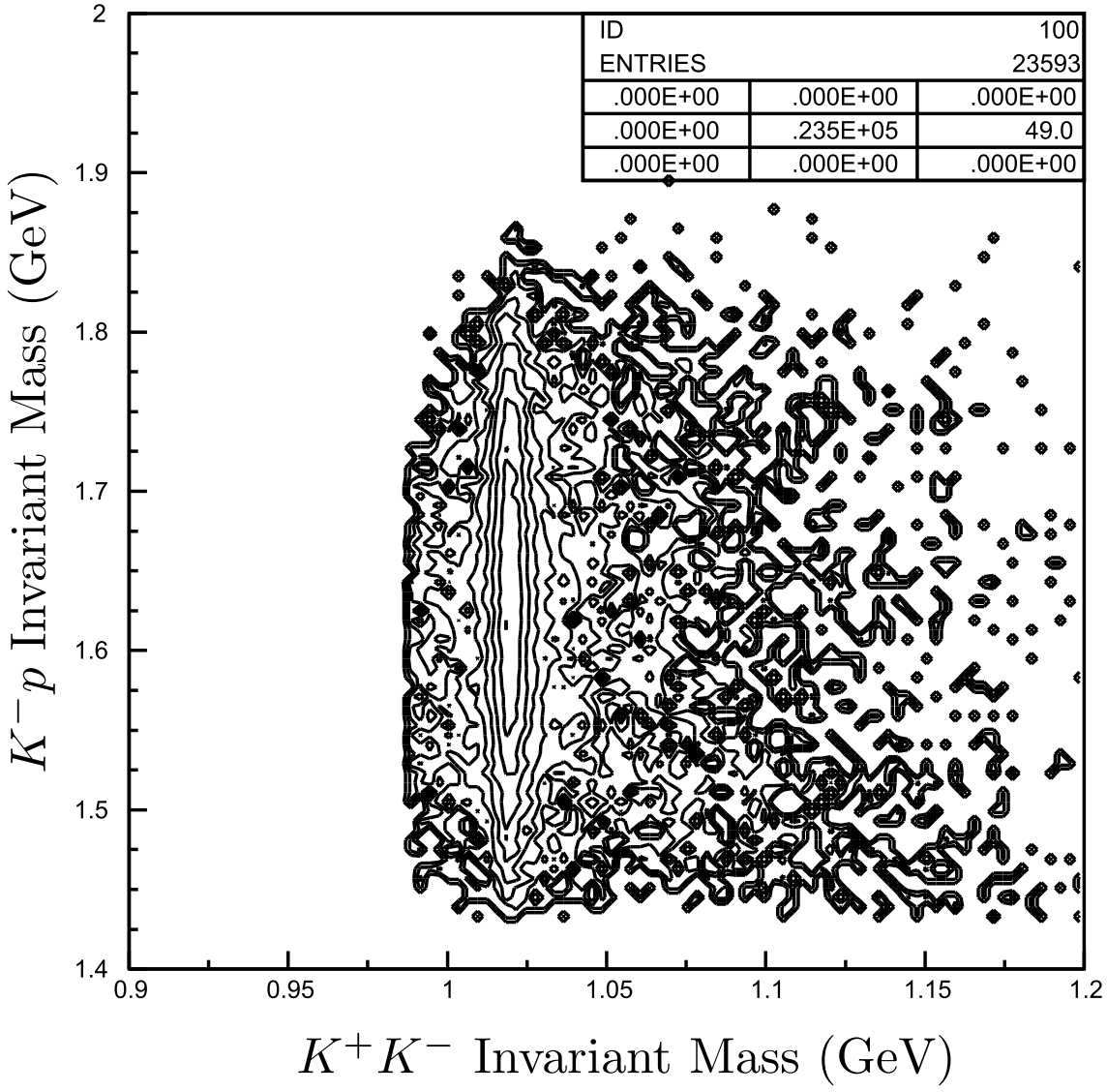

Figure 3.22: K^-p invariant mass distributions for real data as a function of invariant mass K^+K^-. Note that z-axis is in log scale.

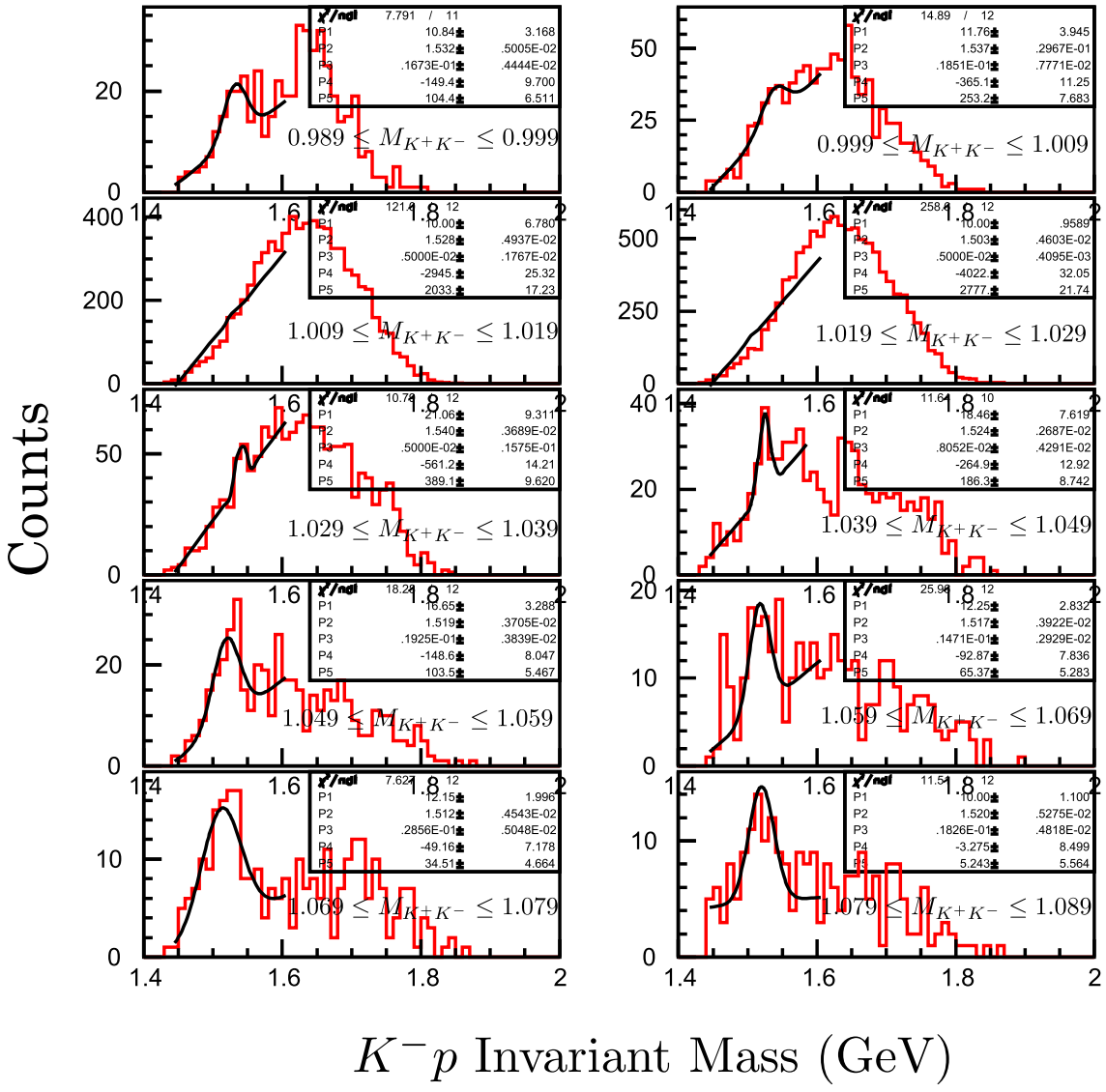

Figure 3.23: The K^-p invariant mass distributions for real data. Each histogram shows the plot in which invariant mass K^+K^- is limited per 10 MeV. Fit function is Gaussian + 1-dimensional polynomial.

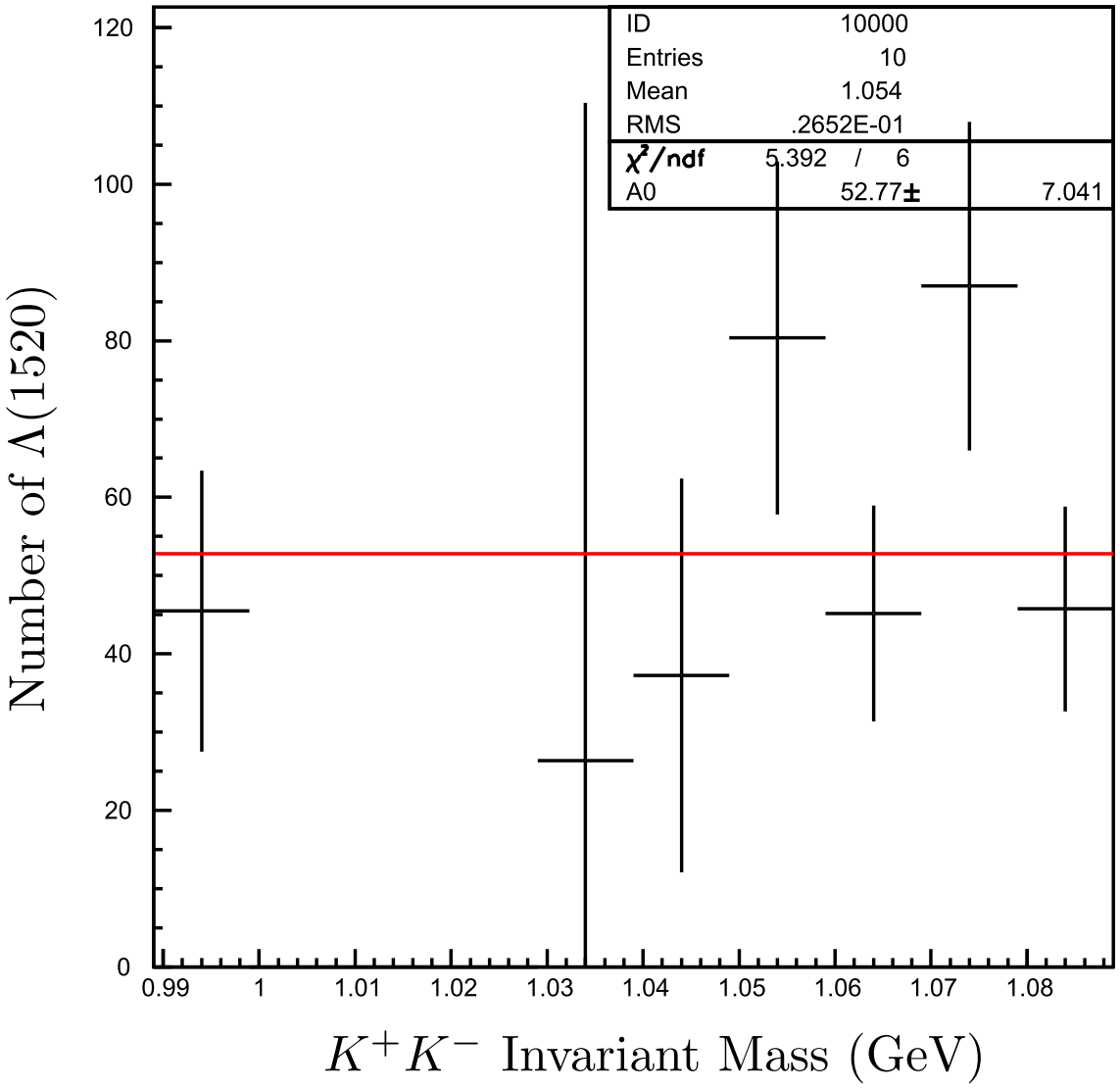

Figure 3.24: Number of Λ as a function of invariant mass K^+K^-. A count of $M_{KK} = 0.999 \sim 1.029$ is extrapolated by fitting.

3.8 The correction of photon flux in neutron rest frame

Previously in Sec.3.5 the minimum momentum, p_{min}^{spec}, is defined as the component of the spectator momentum in the direction of the missing momentum. There, the effective photon energy in neutoron(spectator) rest frame is defined as,

$$E_\gamma^{eff} = (s - M_N^2)/2M_N \tag{3.17}$$

where M_N is proton or neutron mass, s is the square of the total center-of-mass energy of the NKK system obtained by minimum momentum spectator approximation. E_γ^{eff} is used for the binning of photon energy. Thus the incoherent ϕ photoproduction is determined in a more consistent way with data of free proton.

Fig. 3.25 shows the Monte-Carlo simulation result. the resolutions of E_γ (ΔE_γ) for normal incident photonenergy E_γ from Tagger and E_γ^{eff} are figured respectively. The energy resolution for photon-nucleon system is clearly imploved.

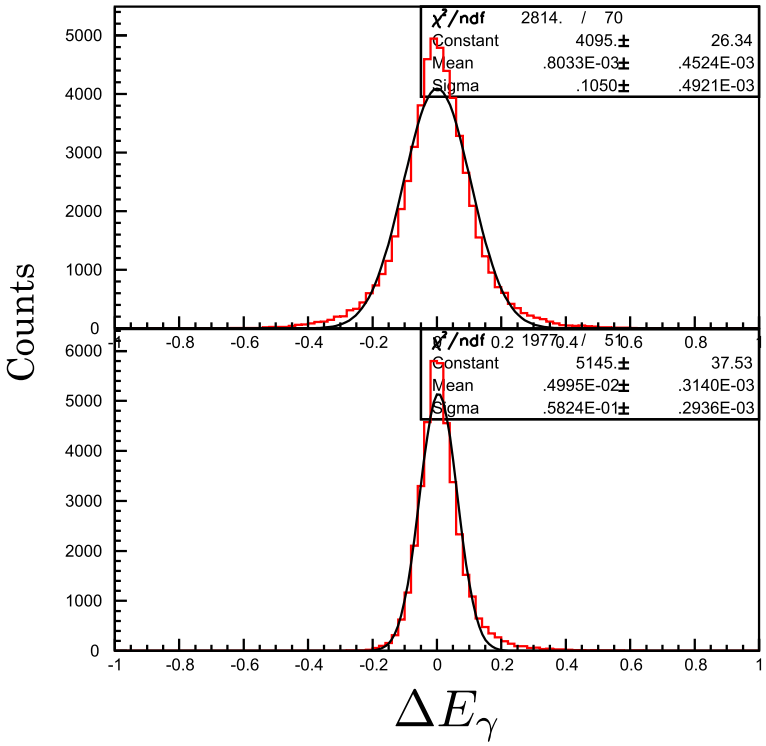

Figure 3.25: E_γ resolution for original E_γ and E_γ^{eff} respectively.

When we stands for the new system with target nucleon at rest, incident photon fraction for labratory system $\omega(\gamma)$, which simply calculated by Tagger scaler count, is not available. For events sitting at one specific E_γ bin, their E_γ^{eff} values would spread over because of kinematical effect of Fermi momentum p_z^F: E_γ is smaller than E_γ^{eff} when p_z^F is in the opposite direction to photon beam, and vice versa. We use Monte-Carlo simulation to generate the conversion ratio from E_γ to E_γ^{eff} in fine binning of 10 MeV, which is our photon beam resolution. Histograms

of conversion ratios at a couple of E_γ^{eff} bins are shown in Fig. 3.26. a photon flux ω_γ as

$$\omega_\gamma^j(E_\gamma^{eff}) = \sum_{i=1}^{i=n} N_j(E_\gamma^i)\omega_\gamma(E_\gamma^i) \tag{3.18}$$

where, $\omega_\gamma(E_\gamma^i)$ is the i-th photon flux in E_γ. $N_j(E_\gamma^i)$ is contribution ratio from E_γ^i for j-th E_γ^{eff}.

Then these conversion ratios are convoluted with the E_γ distribution in the lab system with 10 MeV bin (Fig. 3.27) to obtain the distribution of E_γ^{eff} (Fig.3.28). A cut of $1.5 < E_\gamma < 2.4$ GeV(and $p_{min}^{spec} \leq 0.09$) is applied to eliminate the low- and high-energy edge of Compton photon spectrum where precise MC simulation is missing due to tagger acceptance and multi-line in our laser system.

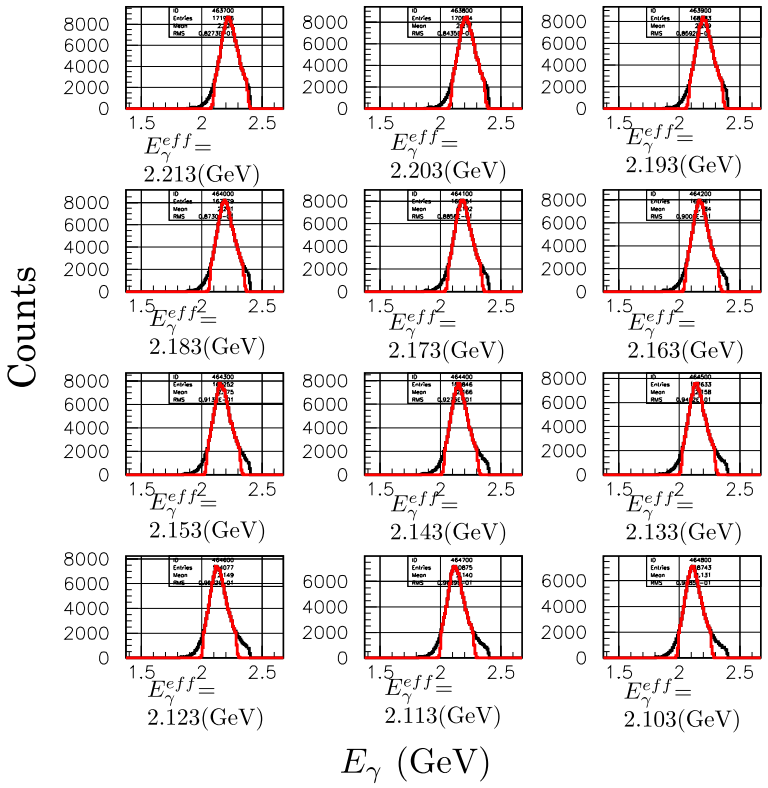

Figure 3.26: Conversion from E_γ to E_γ^{eff}. Each histogram shows a E_γ^{eff} and x-axis is corresponding to E_γ. Red histogram is condition $p_{min}^{spec} \leq 90$ MeV. Each E_γ^{eff} consists of several E_γ bins.

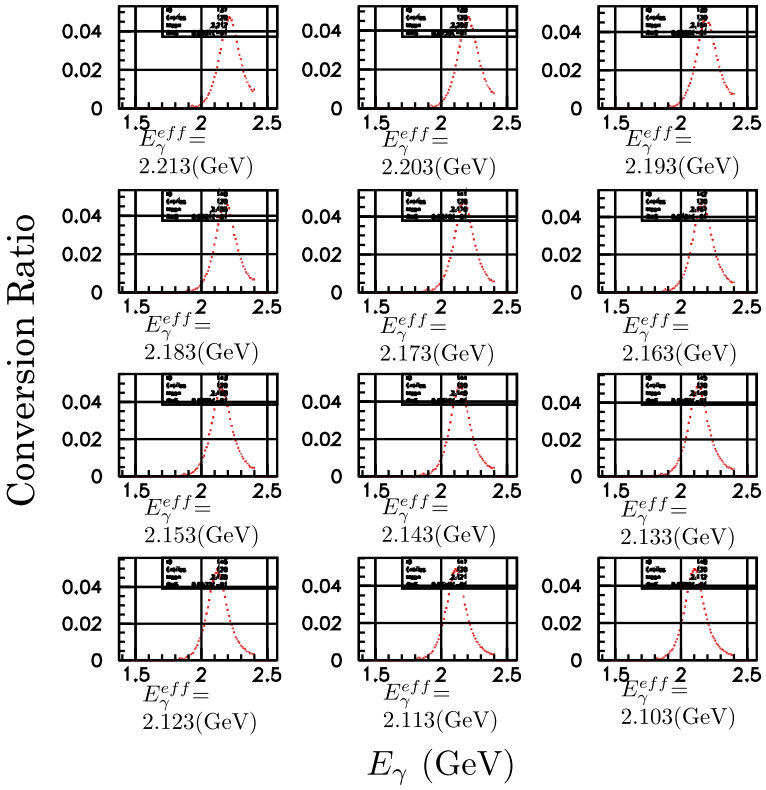

Figure 3.27: Conversion ratio from E_γ to E_γ^{eff}. Each histogram shows a E_γ^{eff} and x-axis is corresponding to E_γ. All histograms are normalized.

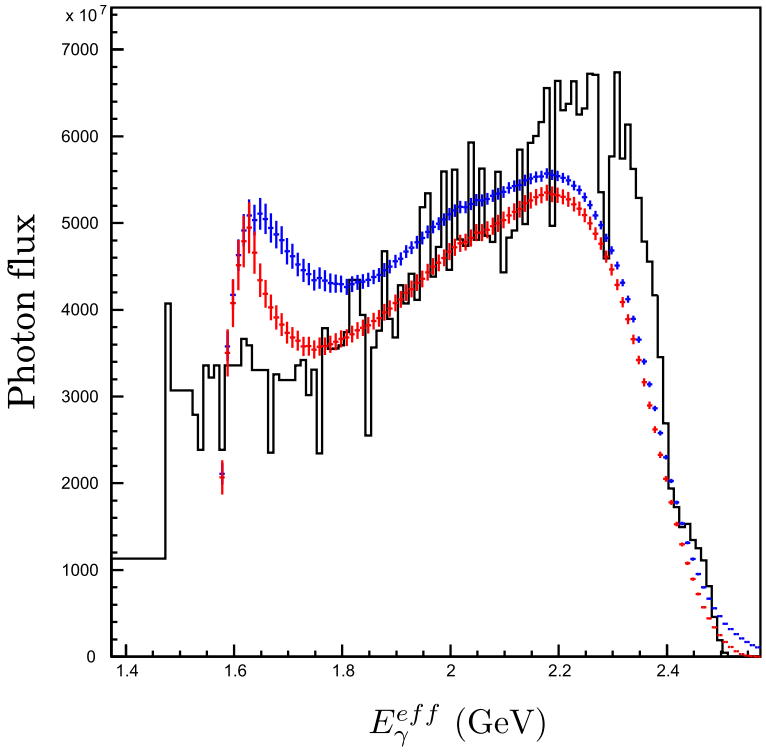

Figure 3.28: Distribution of photon flux. Solid line shows photon flux for original E_γ, blue histgram shows converted photon flux for E_γ^{eff}, red one shows $p_{min}^{spec} \leq 90$ MeV cut applied. x-axis is corresponding to E_γ and E_γ^{eff} respectively.

Chapter 4

Results

4.1 Differential cross section

In this section, the differential cross sections as a function of the photon energy are presented. The differential cross sections are calculated for the LD_2 target, and also, in comparison, it was carried out for the LH_2 target.

4.1.1 Calculation of ϕ yield

The number of ϕ events were identified by the K^+K^- invariant mass distribution and missing mass spectra of $\phi \to K^+K^-$ assuming that the target is proton(nucleon) at rest (MMp). The cut condition $|M(K^+K^-) - 1.019| < 0.01$ (GeV) and $|MMp - 0.9382| < 0.08$ (GeV) was shown in Fig.3.12 (Sec.3.4). Identification of incoherent events is $p_{min}^{spec} \leq 0.09$ GeV(Sec.3.5). The $\tilde{t} = t + |t|_{min}$ was measured with a 0.1 GeV^2 step of $\tilde{t}$. The E_γ bins are defined in Table 4.1.

Table 4.1: Definition of E_γ^{eff}

E_γ^{eff} bin	E_γ^{eff} (GeV)
E1	2.373 - 2.473
E2	2.273 - 2.373
E3	2.173 - 2.273
E4	2.073 - 2.173
E5	1.973 - 2.073
E6	1.873 - 1.973
E7	1.773 - 1.873
E8	1.673 - 1.773
E9	1.573 - 1.673

The number of ϕ events were obtained by subtracting the backgrounds. The background subtraction which was explained in Section 3.7.1 was applied.

4.1.2 Acceptance as a function of $\tilde{t}$

The acceptance of the LEPS detector as a function of E_γ^{eff} bin and $\tilde{t}$ bin is shown in Fig.4.1. The acceptance correction was applied to the measured $\tilde{t}$-distribution. $\tilde{t}$ distribution was further corrected by a factor ω_γ^{eff} which took into account difference of the relative photon flux among different E_γ^{eff} bins due to the non-flat beam energy spectrum. The analysis to obtain the ω_γ is described in Sec 3.8.

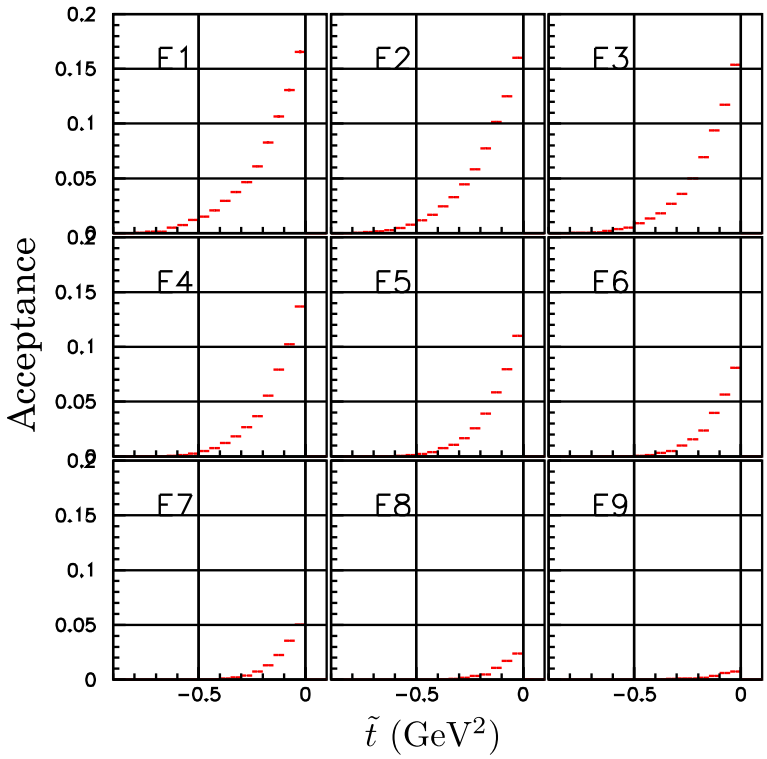

Figure 4.1: Acceptance as a function of $\tilde{t}$

4.1.3 Normalization for ϕ yield

The ϕ cross section as a function of $\tilde{t}$ as,

$$\frac{d\sigma}{d\tilde{t}} = \frac{N_\phi}{\omega_\gamma(E_\gamma^{eff}) P_{trans} P_{branch} N_{tar} P_{ntag>0} Acc} \tag{4.1}$$

where, the variables denote;

- N_ϕ : number of observed ϕ events after the background is subtracted.
- $\omega_\gamma(E_\gamma^{eff})$: relative photon flux in each E_γ^{eff},
- P_{trans} : Probability of transmission in upstream of start counter,
- P_{branch} : Branching ratio for $\phi \to K^+K^-$,

- N_{tar} : Number of target nucleon in unit area,
- $P_{ntag>0}$: Probability of Number of Tagging counter hit
- Acc : Acceptance of LEPS detector(Sec.3.6).

The energy dependence was corrected by a factor $\omega_\gamma(E_\gamma^{eff})$ which took into account difference of the relative photon flux among different E_γ^{eff} bins due to the non-flat beam energy spectrum. The analysis to obtain the $\omega_\gamma(E_\gamma^{eff})$ is described in Appendix 3.8. The number of target nucleon N_{tar} a unit area is calculated as

$$N_{tar} = \frac{N_A \rho \xi}{A} \tag{4.2}$$

where, A, ξ and ρ is mass number, thickness, and density, respectively, and $N_A = 6.02213 \times 10^{23}$ stands for Avogadro number. P_{trans} is 0.526 $\pm$ 0.03 estimated by transmission study[43]. $P_{ntag>0}$ is set to 0.762 [29]. Summary of normalization factor is shown in Table 4.2.

Table 4.2: Summary of Normalization factor

	values
P_{trans}	0.526 $\pm$ 0.03
P_{branch}	0.492 $\pm$ 0.007
$N_{tar}(\mathrm{LD_2})$	8.56×10^{23}
$N_{tar}(\mathrm{LH_2})$	6.77×10^{23}
$P_{ntag>0}$	0.762

4.1.4 The $\tilde{t}$ distribution

Figure 4.2 shows the t distributions as a function of energy after the above corrections. The fitting to exponential function

$$\frac{d\sigma}{d\tilde{t}} = C \exp(-b\tilde{t}) \tag{4.3}$$

is applied for each photon energy E_γ^{eff}. The result of the fit to the $\tilde{t}$ distribution was summarized in Table 4.3. The slope parameter b as a function of E_γ^{eff} is shown in Fig.4.3. The slope b = 3.74 $\pm$0.12 is obtained by averaging over each E_γ^{eff}. On the assumption that the slope parameters have the smooth energy dependence, in the present analysis, we choose the average value of slope parameter. Fig.4.4 shows a fit by a constant slope function (using average slope value). The result of the fit to the $\tilde{t}$ distribution with constant slope was summarized in Table 4.4. Table 4.5 shows χ^2 values for two fit methods. No big difference was seen in which slope methods.

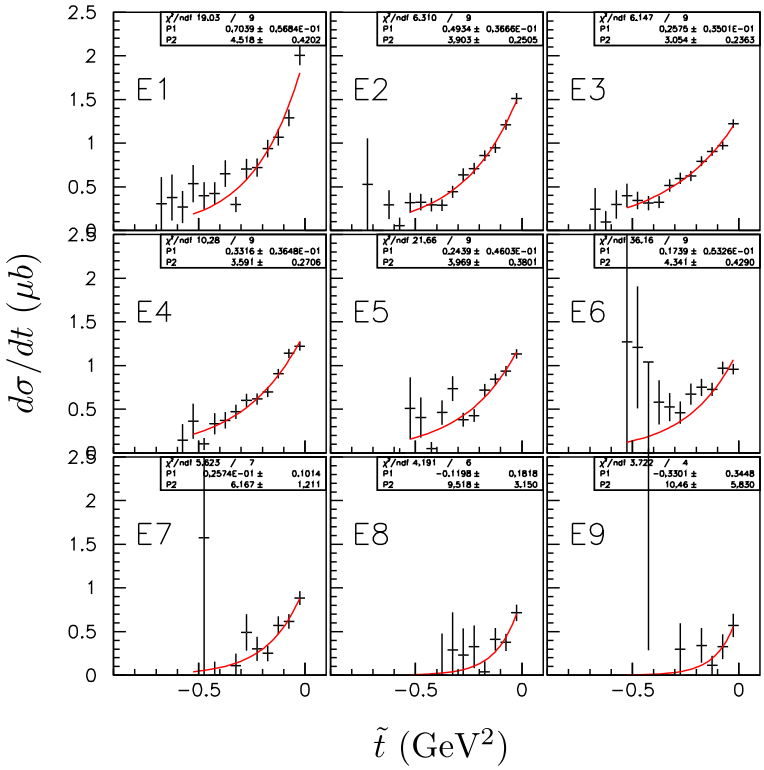

Figure 4.2: $\tilde{t}$ distributions for incoherent production. Red lines represent the fitting results with Eq.4.3

Table 4.3: Results of the fit to the $\tilde{t}$ distributions

E_γ^{eff} bin	$\frac{d\sigma}{d\tilde{t}}_{\tilde{t}=0}$ (μ b)	b (GeV^{-2})	χ^2/ndf
E9	0.72 ± 0.248	10.5 ± 0.42	0.93
E8	0.89 ± 0.161	9.52 ± 0.25	0.70
E7	1.03 ± 0.104	6.17 ± 0.24	0.80
E6	1.19 ± 0.064	4.34 ± 0.27	4.02
E5	1.28 ± 0.059	3.97 ± 0.38	2.41
E4	1.39 ± 0.051	3.59 ± 0.43	1.14
E3	1.29 ± 0.045	3.05 ± 1.21	0.68
E2	1.64 ± 0.060	3.90 ± 3.15	0.70
E1	2.02 ± 0.115	4.52 ± 5.83	2.11

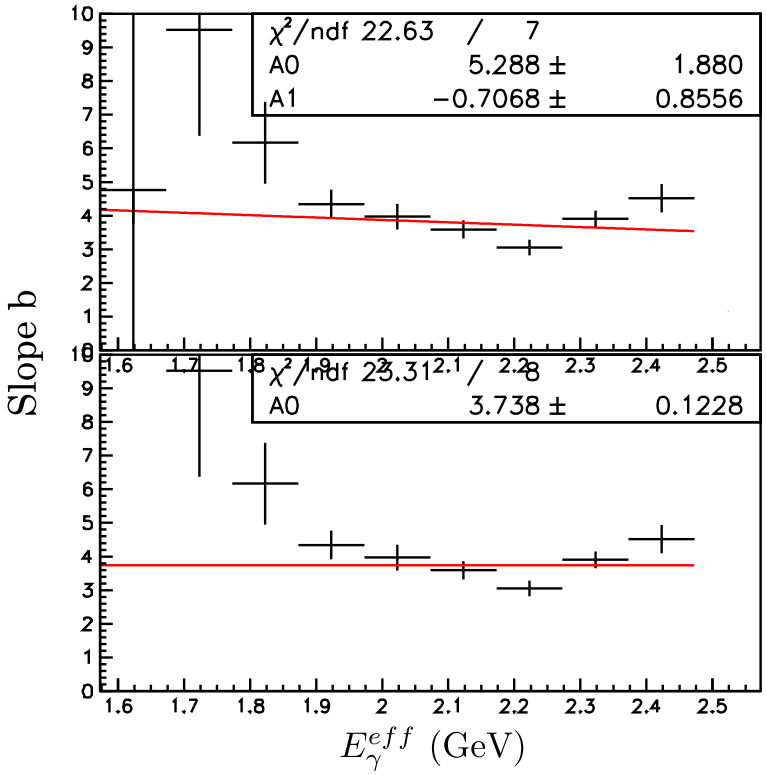

Figure 4.3: The energy dependence of the slope parameter b. Upper histogram was fitted with linear function. Lower histogram shows average of slope. Error bar represents the statistical error only.

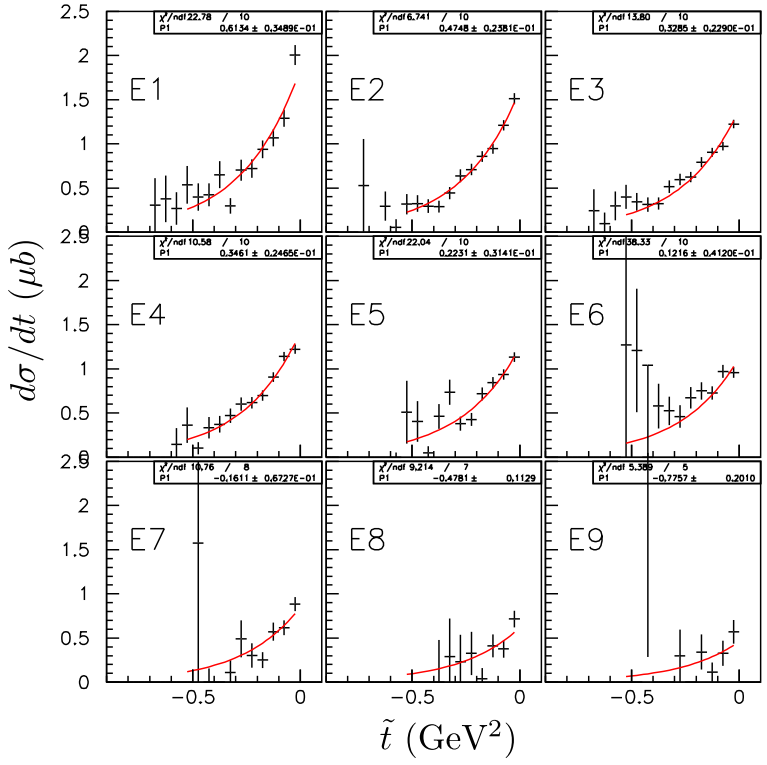

Figure 4.4: $\tilde{t}$ distributions. The distributions are fitted with constant slope.

Table 4.4: Results of the fit to the $\tilde{t}$ distributions(constant b)

E_γ^{eff} bin	$\frac{d\sigma}{d\tilde{t}}_{\tilde{t}=0}$ (μ b)	b (GeV^{-2})	χ^2/ndf
E9	0.460 ± 0.093	const.	1.08
E8	0.620 ± 0.070	const.	1.31
E7	0.851 ± 0.057	const.	1.35
E6	1.293 ± 0.047	const.	3.83
E5	1.250 ± 0.039	const.	2.20
E4	1.414 ± 0.035	const.	1.06
E3	1.389 ± 0.032	const.	1.38
E2	1.608 ± 0.038	const.	0.67
E1	1.847 ± 0.064	const.	2.28

Table 4.5: comparison of χ^2 values for the two fitting methods

slope	χ^2	ndf	χ^2/ndf
free	113.1	71	1.59
const	139.6	80	1.75

4.1.5 Energy dependence of differential cross section at $\tilde{t} = 0$ GeV^2

Figure 4.5 shows the energy dependence of the differential cross section at $\tilde{t} = 0$ GeV^2 without assuming any smooth energy dependence of the t-slope. The error bar represents the statistical error only.

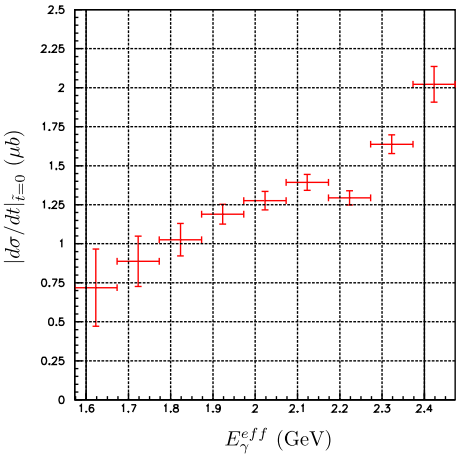

Figure 4.5: The energy dependence of the differential cross section at $\tilde{t} = 0$. Error bar represents the statistical error only.

Figure 4.6 shows the energy dependence of the differential cross section at $\tilde{t} = 0$ GeV^2 with assumption of constant slope b. The error bar represents the statistical error only. As shown in Appendix C, the selection cut for incoherent production using p_{min}^{spec} is imperfect at higher E_γ bin. Therefore, this prescription may introduce a systematic errors for result. The systematic error from this p_{min}^{spec} cut condition was estimated by the calculation of the coherent contamination using Monte Carlo simulation.

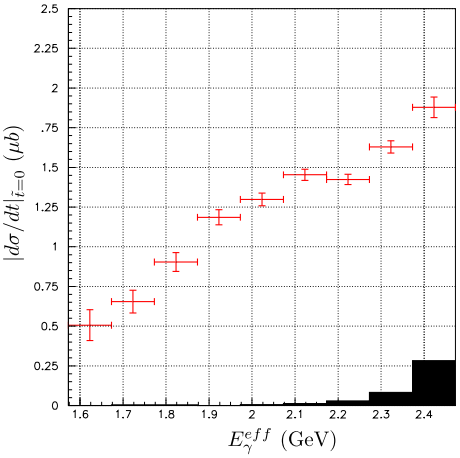

Figure 4.6: The energy dependence of the differential cross section at $\tilde{t} = 0$. Error bar represents the statistical error only. Filled histogram indicates the systematic error due to the coherent contamination.

4.1.6 K^+K^-p event

In the case of K^+K^-p 3-track event, although its statistics is very limited, it is unique tool to compare exclusive reactions and quasi-free events from the proton. Figure 4.7 is shown a fit by a constant function (average slope value $b_{proton} = 3.38$). Figure 4.7 shows the energy dependence of the differential cross section at $\tilde{t} = 0$ GeV^2 with assumption of constant slope b. The error bar represents the statistical error only

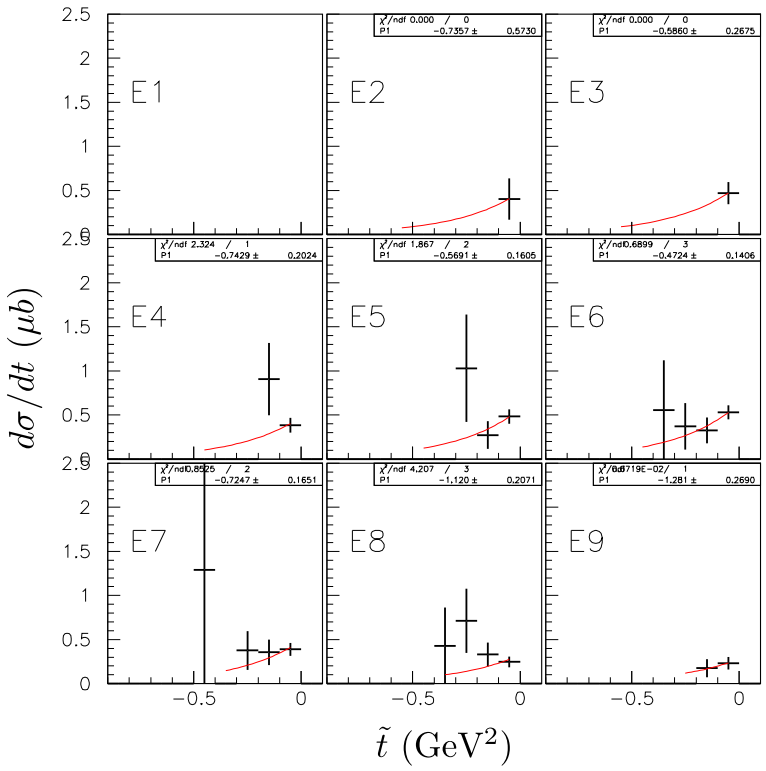

Figure 4.7: $\tilde{t}$ distributions in K^+K^-p mode. Red line represents the fitting with constant slope value.

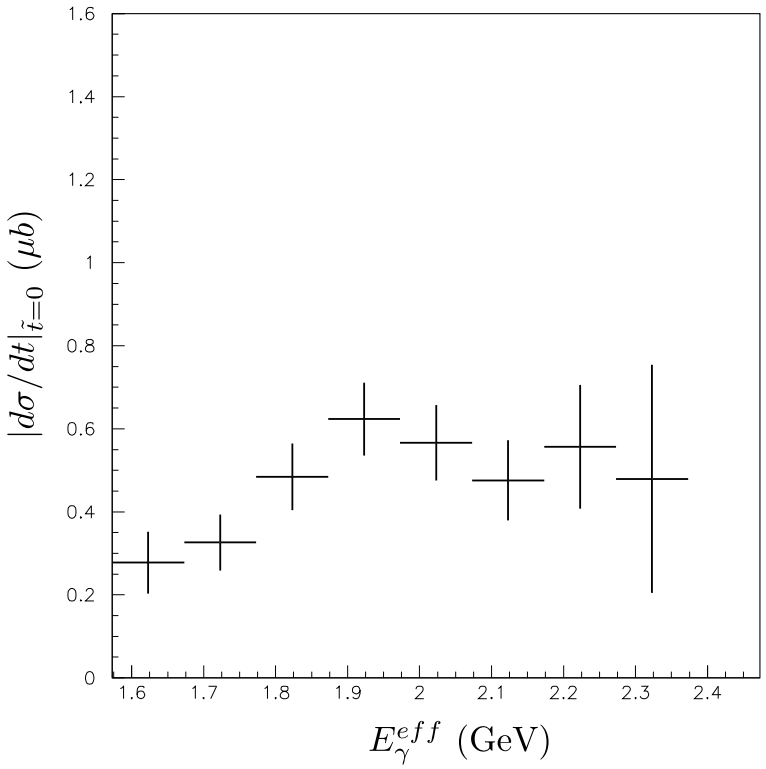

Figure 4.8: The energy dependence of the differential cross section at $\tilde{t} = 0$ in K^+K^-p mode. Error bar represents the statistical error only.

4.2 The decay angular distribution

Measurement of the decay angular distributions of ϕ meson is described in this section. The angular distributions of the K^+ from the ϕ decay were measured at forward angles($\tilde{t}\geq$-0.1) from 1.773GeV to 2.573 GeV. The E_γ bins are defined in Table 4.6.

Table 4.6: Definition of E_γ

E_γ bin	E_γ (GeV)
E1	2.373 - 2.573
E2	2.173 - 2.373
E3	1.973 - 2.173
E4	1.773 - 1.973

The angular distributions for 5 angular variables ($\cos\theta, \phi, \phi - \Phi, \phi + \Phi, \Phi$) were used to extract the spin density matrix elements. The angles were divided into 10 bins with equal bin size.

4.2.1 The acceptance calculation

The acceptance for different polarization angle (the VT data and the HZ data) was obtained separately from the Monte Carlo simulation. It was assumed that all the spin density elements are equal to proton case [6]. The acceptance as a function of angles are shown in Fig.4.9,4.10.

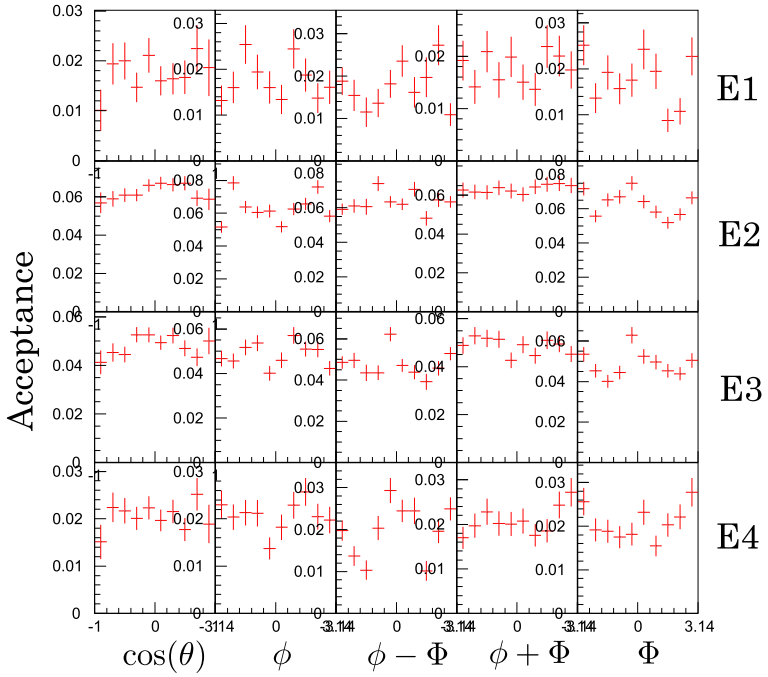

Figure 4.9: Acceptance for Vert data as a function of angles (a) $\cos\theta$, (b) ϕ, (c) $\phi - \Phi$, (d) $\phi + \Phi$, (e) Φ.

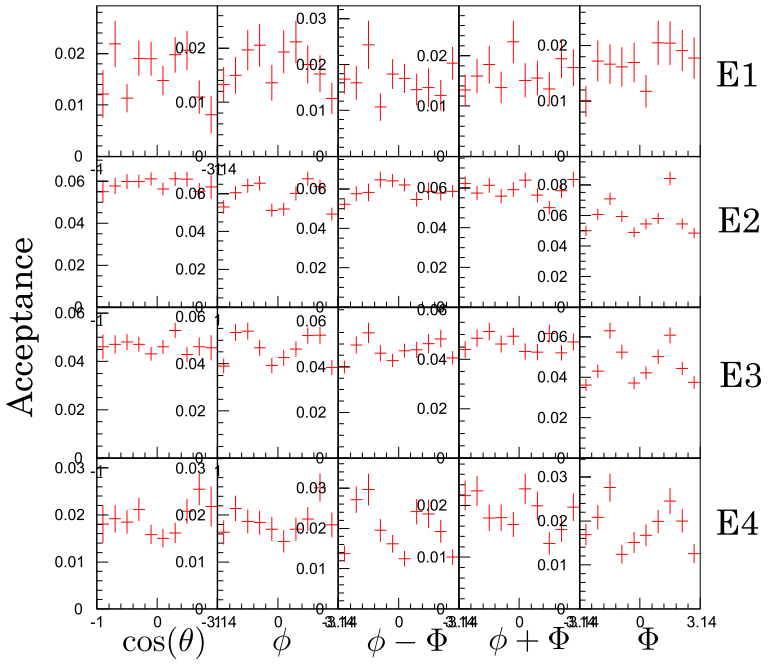

Figure 4.10: Acceptance for Horz data as a function of angles (a) $\cos\theta$, (b) ϕ, (c) $\phi - \Phi$, (d) $\phi + \Phi$, (e) Φ.

4.2.2 The spin density matrix elements

The number of events from the ϕ photoproduction as a function of the decay angle were measured by the same way as those in the measurement of the differential cross section (Section 4.1). The background subtraction was applied in each angular bin. The acceptance-corrected angular distributions were analyzed to extract the density matrix elements. The decay angular distributions for Vert and Horz sample are shown in Fig. 4.11 and Fig. 4.12, respectively.

Fit to the one-dimensional angular distribution was applied using following parameterizations :

$$W(\cos\theta) = N_0(\frac{1}{2}(1-\tilde{\rho}_1)(1-\cos^2\theta)+\tilde{\rho}_1\cos^2\theta) \quad (4.4)$$

$$W(\phi) = N_0(1-2\tilde{\rho}_2\cos(2\phi)) \quad (4.5)$$

$$W(\phi-\Phi) = N_0(1+2P_\gamma\tilde{\rho}_3\cos(2(\phi-\Phi)) \quad (4.6)$$

$$W(\phi+\Phi) = N_0(1+2P_\gamma\tilde{\rho}_4\cos(2(\phi+\Phi)) \quad (4.7)$$

$$W(\Phi) = N_0(1-P_\gamma\tilde{\rho}_5\cos 2\Phi), \quad (4.8)$$

where N_0 and $\tilde{\rho}_1$, $\tilde{\rho}_2$, $\tilde{\rho}_3$, $\tilde{\rho}_4$, $\tilde{\rho}_5$ are parameters in the fit. P_γ is a degree of photon polarization, calculated by QED (Fig. 2.2) multiplied by the polarization of the laser (P_{laser}). The polarization of the laser was obtained by averaging the measured polarization for each run [27] weighted by the number of photon. The P_{laser} was 0.9869 for the VT data and 0.9498 for the HZ data. The average polarization of the photon P_γ was shown in table 4.7.

Table 4.7: polarization of photon P_γ

E_γ	P_γ (Horz)	P_γ (Vert)
E1	0.89	0.93
E2	0.88	0.92
E3	0.84	0.88
E4	0.76	0.79

The fitting to the angular distributions by Eq. 4.4-4.8 was made simultaneously for the Vert and the Horz data.

In comparison of Eq. 4.4-4.8 with Eq. A.3-A.7, there are following relations between fitting parameters $\tilde{\rho}_i(i=1-5)$ and the spin density matrix elements (see Appendix A):

$$\tilde{\rho}_1 = \rho^0_{00} \quad (4.9)$$

$$\tilde{\rho}_2 = \rho^0_{1-1} \quad (4.10)$$

$$\tilde{\rho}_3 = (\rho^1_{1-1} - \mathrm{Im}\rho^2_{1-1})/2 \quad (4.11)$$

$$\tilde{\rho}_4 = (\rho^1_{1-1} + \mathrm{Im}\rho^2_{1-1})/2 \quad (4.12)$$

$$\tilde{\rho}_5 = 2\rho^1_{11} + \rho^1_{00} \quad (4.13)$$

The fitting result of measured spin density matrix is shown Fig4.13,

The angular distributions for all data (the Vert data + the Horz data) are shown in Fig. 4.14. The spin density matrix elements are summarized in Table 4.8,4.9,4.10.

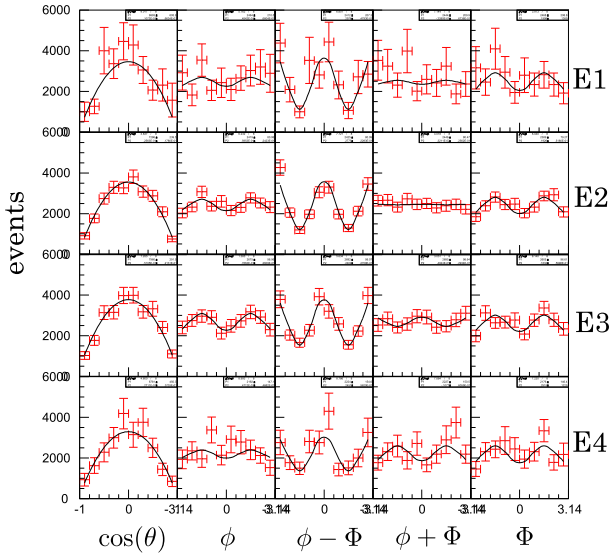

Figure 4.11: Decay angular distributions for the Vert data after the acceptance correction. Each solid curve indicates a fit to the data according to Eq.4.4-4.8.

Table 4.8: Spin density matrix elements for Vert

	$\tilde{\rho}_1$	$\tilde{\rho}_2$	$\tilde{\rho}_3$	$\tilde{\rho}_4$	$\tilde{\rho}_5$
E4	0.027±0.037	0.047±0.047	0.245±0.056	-0.108±0.061	0.251±0.123
E3	0.051±0.021	0.079±0.026	0.247±0.027	0.049±0.029	0.183±0.060
E2	0.026±0.018	0.060±0.024	0.277±0.023	0.003±0.026	0.193±0.052
E1	0.011±0.066	0.045±0.066	0.298±0.048	-0.023±0.067	0.200±0.139

Table 4.9: Spin density matrix elements for Horz

	$\tilde{\rho}_1$	$\tilde{\rho}_2$	$\tilde{\rho}_3$	$\tilde{\rho}_4$	$\tilde{\rho}_5$
E4	0.076±0.045	0.025±0.043	0.188±0.065	-0.106±0.054	-0.217±0.107
E3	0.056±0.022	0.038±0.028	0.174±0.030	-0.011±0.032	0.040±0.063
E2	0.103±0.022	0.039±0.024	0.259±0.024	0.011±0.026	-0.035±0.052
E1	0.017±0.052	-0.074±0.055	0.251±0.059	0.041±0.060	0.073±0.131

Table 4.10: Spin density matrix elements for Horz + Vert

	$\tilde{\rho}_1$	$\tilde{\rho}_2$	$\tilde{\rho}_3$	$\tilde{\rho}_4$	$\tilde{\rho}_5$
E4	0.050±0.030	0.033±0.032	0.224±0.046	-0.092±0.040	0.051±0.081
E3	0.055±0.015	0.061±0.019	0.218±0.020	0.019±0.021	0.113±0.044
E2	0.062±0.014	0.049±0.017	0.270±0.016	0.007±0.018	0.081±0.037
E1	0.028±0.046	0.001±0.045	0.282±0.039	0.024±0.046	0.159±0.102

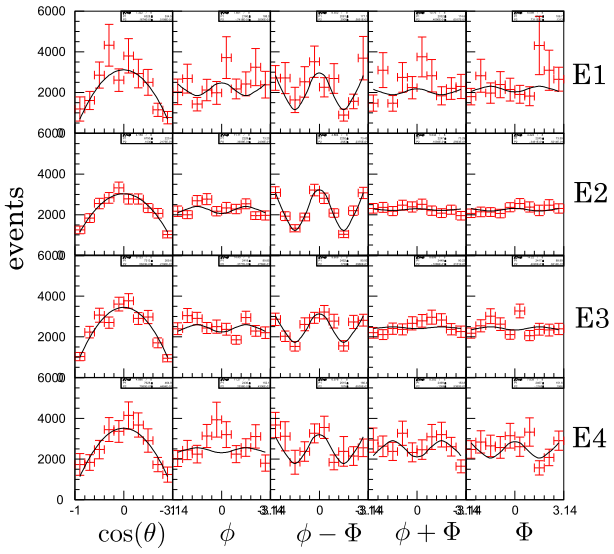

Figure 4.12: Decay angular distributions for the Horz data after the acceptance correction. Each solid curve indicates a fit to the data according to Eq.4.4-4.8.

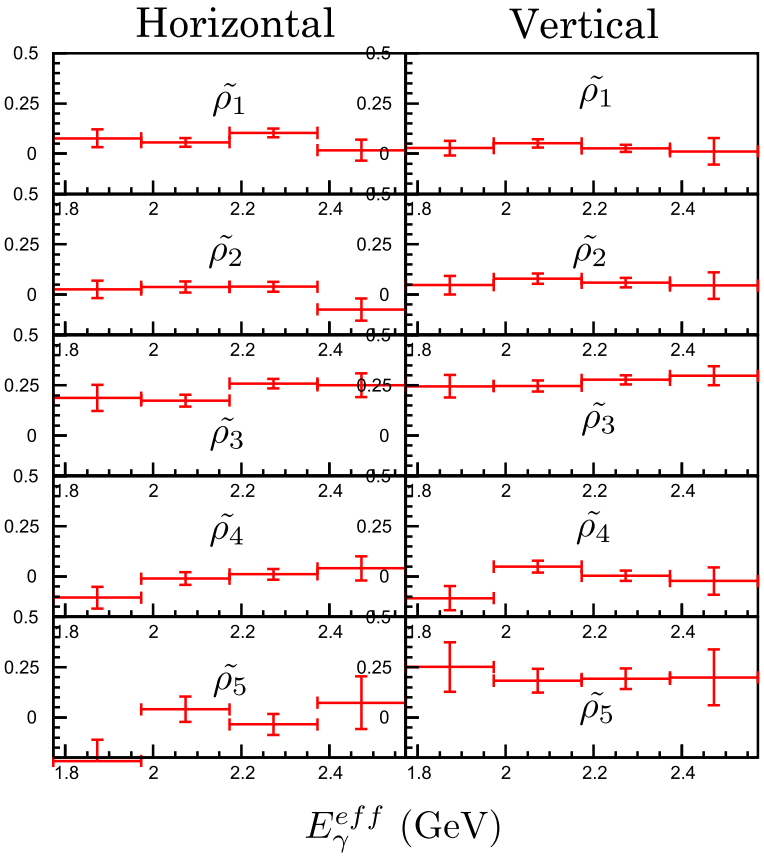

Figure 4.13: Spin density matrix elements of Eq.4.4-4.8.Left and right side histograms are Horz and Vert respectively.

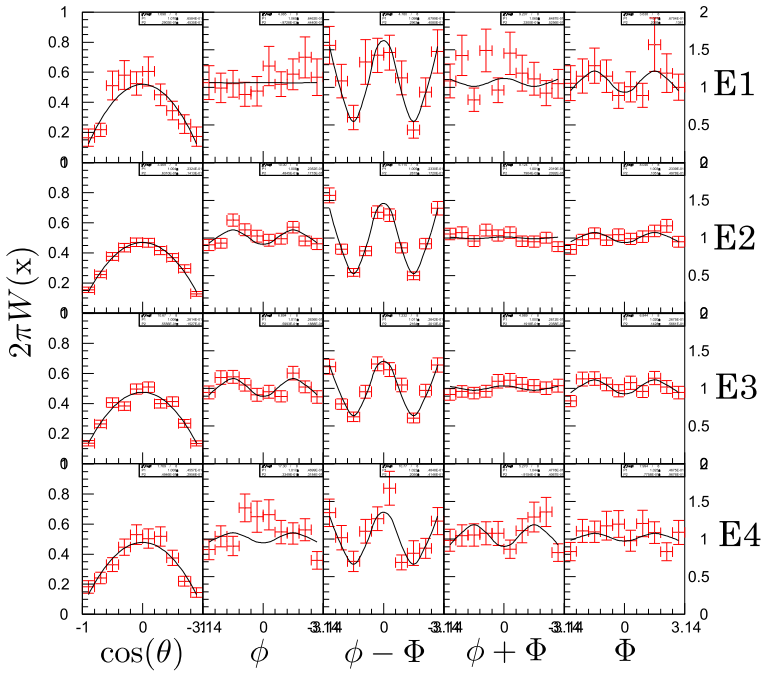

Figure 4.14: Decay angular distributions for the Vert + Horz. Each solid curve indicates a fit to the data according to Eq.4.4-4.8.

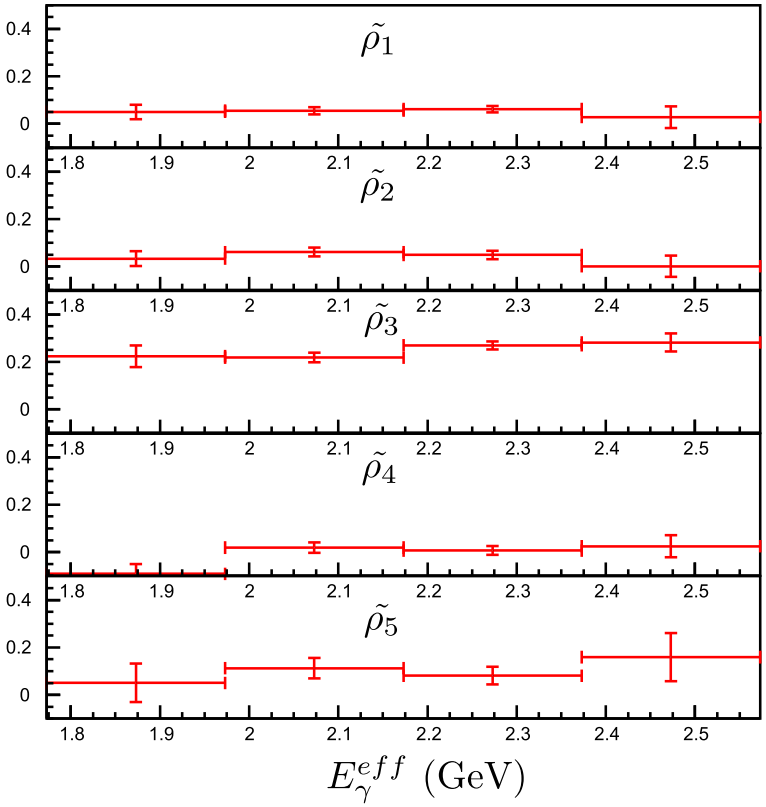

Figure 4.15: Spin density matrics elements of Eq.4.4-4.8. Histgrams contain both Horz and Vert.

Chapter 5

Conclusion and Discussions

Differential cross section

The converted E_γ^{eff} improves photon energy resolution and enable precise comparison with proton data.
The differential cross section as a function of $\tilde{t}$ (Fig. 4.2) has a consistent averaged slope b= 3.74 $\pm$ 1.2 value on proton at LEPS(b = 3.38 $\pm$ 0.23). This means that the quasi-free like incoherent process are observed using small p_{min}^{spec}.
The cross sections at $\tilde{t} = 0$ of incoherent production from deuterium as a function of the photon energy are shown in Fig.5.1, together with data from proton. The nuclear transparency ratios for deuterium T_d are also shown. T_d is defined as

$$T_d = \frac{|d\sigma/dt|^N_{\tilde{t}=0}}{2 * |d\sigma/dt|^p_{\tilde{t}=0}}$$

where, $|d\sigma/dt|^N_{\tilde{t}=0}$ and $|d\sigma/dt|^p_{\tilde{t}=0}$ are the cross section for incoherent and free proton respectively. Comparing with the production from a free proton, a significant $\sim$30% reduction of the yield per nucleon is observed for incoherent production from deuteron. From the result of ϕ photo-production off nuclei [11], a target mass number dependence of A^α is larger than that of theoretical prediction. One possible reason of this large reduction in nuclear medium is considered as large ϕ and nucleon total cross section $\sigma_{\phi N}$ in nuclei. However, since the deuteron is composed of a loosely bound proton and neutron, where the nuclear medium effect is minimal, the present observations strongly suggest that some effect other than nuclear density is necessary to achieve a complete understanding of the reduction of ϕ production in the nuclear medium [44]. For example, the ϕ meson converts to ω or π, then $\omega(\pi)$ absorbed by nucleon depending on large cross section $\sigma_{\omega N}$ and $\sigma_{\pi N}$[45]. In the low energy region like a production threshold, these two-step processes coupled-channel effects might induce a more significant loss of ϕ-mesons in nuclei than the current theoretical estimates.

In this study, we introduced the effective photon energy E_γ^{eff} at γ-N system using minimum momentum spectator approximation (Sec.3.5), in consequence, the photon energy resolution was improved well. However, since this assumption might cancel the enhancement of cross section at sub-threshold energy region, the large reduction of incoherent production could be caused as the result of this method. In Fig.5.2, the cross section of incoherent ϕ photo-production at $\tilde{t}$=0 in the LAB system(as a function of E_γ) instead of E_γ^{eff} are shown. In the

LAB system, the similar reduction appeared too. In addition, around E_γ ~1.9 GeV in which the photon flux is almost the same for both E_γ and E_γ^{eff}, this phenomenon still remains.

Another possible reason of this reduction might be considered the exclusion cut for coherent production. With the Fig.5.3, which shows the cross section at $\tilde{t}$=0 and the transparency ratio without the coherent exclusion cut, even if there is the whole contribution from the coherent production, the cross section from deuteron decreases compared with free proton. In particularly, at E_γ ≤2.0 GeV region, since the coherent contribution are quiet small, the reason of reduction couldn't be represented. From these reason, the reduction of the incoherent cross section from deuteron remains significant.

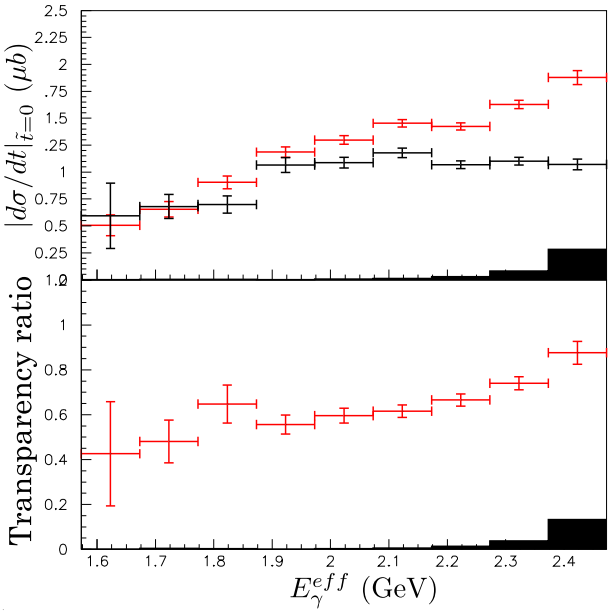

Figure 5.1: Upper figure shows the differential cross sections at $\tilde{t}$ = 0 GeV^2 of incoherent $\gamma N \rightarrow \phi N(|d\sigma/dt|^N_{\tilde{t}=0}$, red histogram) and $\gamma p \rightarrow \phi p(|d\sigma/dt|^p_{\tilde{t}=0}$, black histogram) simultaneously. Lower figure is a deuteron transparency ratio $T_d = |d\sigma/dt|^N_{\tilde{t}=0}/2 * |d\sigma/dt|^p_{\tilde{t}=0}$ as a function of the effective photon energy(E_γ^{eff}). Error bar represents the statistical error only. Filled histogram indicates the systematic error due to the coherent contamination.

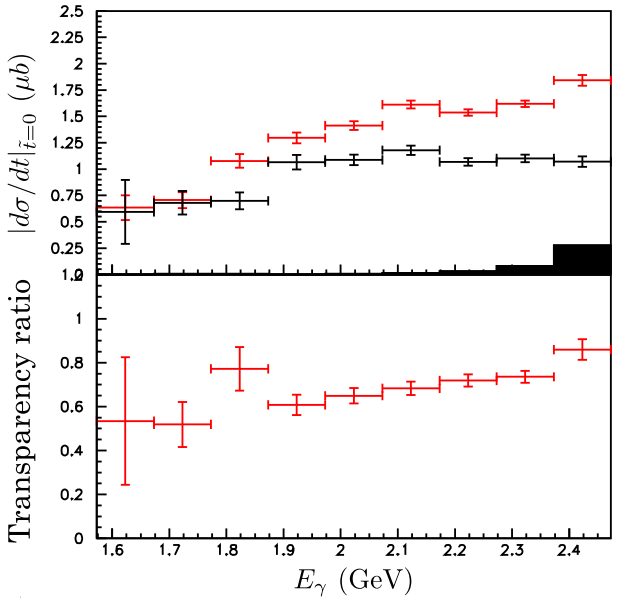

Figure 5.2: Upper figure shows the differential cross sections at $\tilde{t} = 0$ GeV^2 of $\gamma N \to \phi N$ ($|d\sigma/dt|^N_{\tilde{t}=0}$, red histogram) and $\gamma p \to \phi p$($|d\sigma/dt|^p_{\tilde{t}=0}$, black histogram) simultaneously. Lower figure is a deuteron transparency ratio $T_d = |d\sigma/dt|^N_{\tilde{t}=0}/2{*}|d\sigma/dt|^p_{\tilde{t}=0}$ as a function of the photon energy at LAB system(E_γ). Error bar represents the statistical error only. Filled histogram indicates the systematic error due to the coherent contamination.

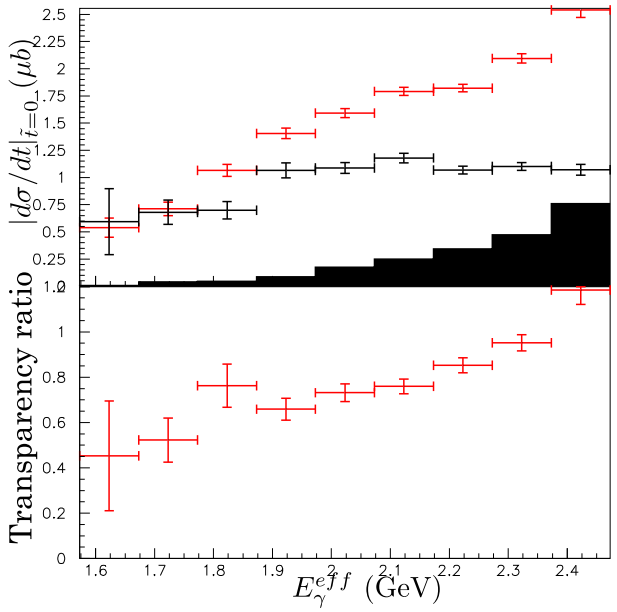

Figure 5.3: Upper figure shows the differential cross sections at $\tilde{t} = 0$ GeV^2 of $\gamma N \to \phi N$ without p^{spec}_{min} cut ($|d\sigma/dt|^{p^{spec}_{min}=all}_{\tilde{t}=0}$, red histogram) and $\gamma p \to \phi p$($|d\sigma/dt|^p_{\tilde{t}=0}$, black histogram) simultaneously. Lower figure is a deuteron transparency ratio $T_d = |d\sigma/dt|^N_{\tilde{t}=0}/2*|d\sigma/dt|^p_{\tilde{t}=0}$ as a function of photon energy. Error bar represents the statistical error only. Filled histogram indicates the systematic error due to the coherent contamination.

$\pi - \eta$ interference

We examined the isospin dependence of photoproduction by studying the exclusive K^+K^-p events whose final state of a K^+K^- pair and a proton is fully detected in the spectrometer. The kinematics of these events is dominated by interactions with the proton inside deuteron. The transparency ratio T_{excl} shown in Fig.5.4 is defined as

$$T_{excl} = \frac{|d\sigma/dt|^{excl}_{\tilde{t}=0}}{|d\sigma/dt|^{p}_{\tilde{t}=0}}$$

where, $|d\sigma/dt|^{excl}_{\tilde{t}=0}$ is the cross section of exclusive K^+K^-p event from deuteron. In Fig.5.4, there is a similar degree of reduction for quasi-free events from the proton as compared with exclusive reactions. Therefore the reduction in ϕ yields occurs in a similar scale for the incoherent production from both the proton and the neutron inside deuterium. It also suggests that the π-η interference effect, which makes a difference in the production from proton and neutron, is small.

In this analysis, we could get the all momentum for K^+, K^- and proton. Therefore, the effective photon energy at γp system could be calculated using the measured momentum of proton($E^{eff}_{\gamma}(KKp)$). On the other hand, we could also obtain the effective photon energy with minimum momentum method which contain only K^+ and K^- information($E^{eff}_{\gamma}(KK)$). Fig.5.5 shows the relation of these two photon energy ($E^{eff}_{\gamma}(KKp)$) and ($E^{eff}_{\gamma}(KK)$). The estimation for the effective photon energy with minimum momentum method works very well. Similarly, the difference of cross section at $\tilde{t}$=0 between ($E^{eff}_{\gamma}(KKp)$) and ($_E\gamma^{eff}(KK)$) in exclusive K^+K^-p events is figured in Fig.5.6. As the result makes no significant difference within statistical error, the estimation of effective photon energy works properly.

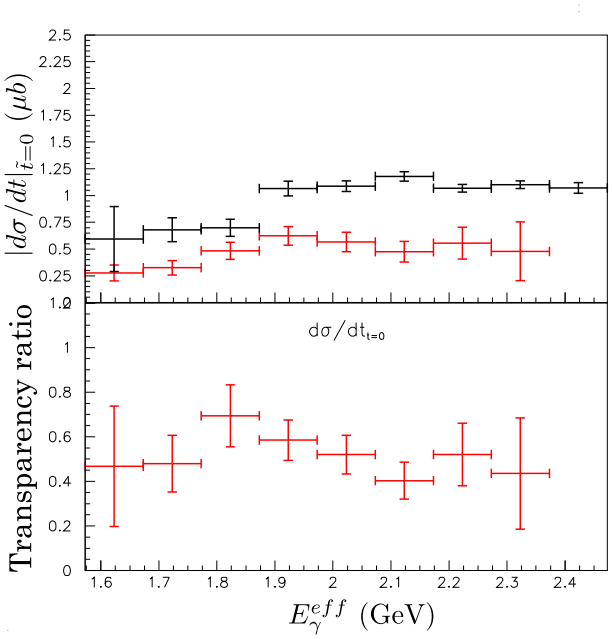

Figure 5.4: Upper figure shows differential cross sections at $\tilde{t} = 0$ GeV^2 in final state with K^+K^-p exclusive event from deuterium target (red histogram) and $\gamma p \to \phi p$ from free proton (black histogram) simultaneously. Lower figure is a transparency ratio $T_{excl} = |d\sigma/dt|^{excl}_{\tilde{t}=0}/|d\sigma/dt|^{p}_{\tilde{t}=0}$ as a function of photon energy. Error bar represents the statistical error only.

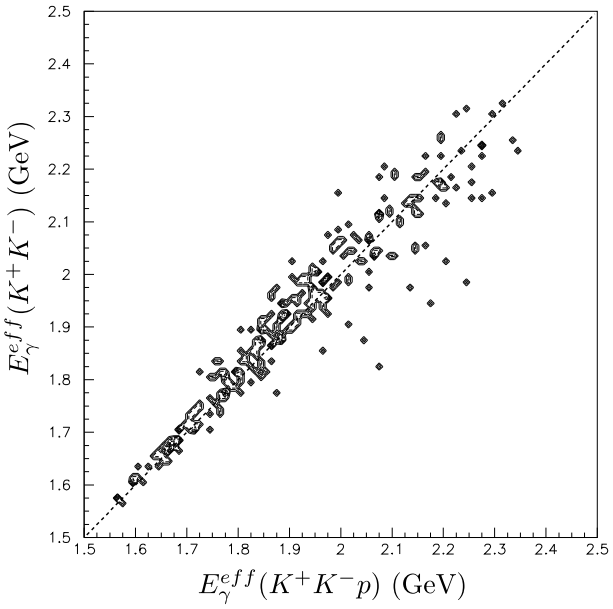

Figure 5.5: The relation between $E_\gamma^{eff}(KKp)$ and $E_\gamma^{eff}(KK)$ (GeV) in final state with K^+K^-p exclusive events from deuterium target.

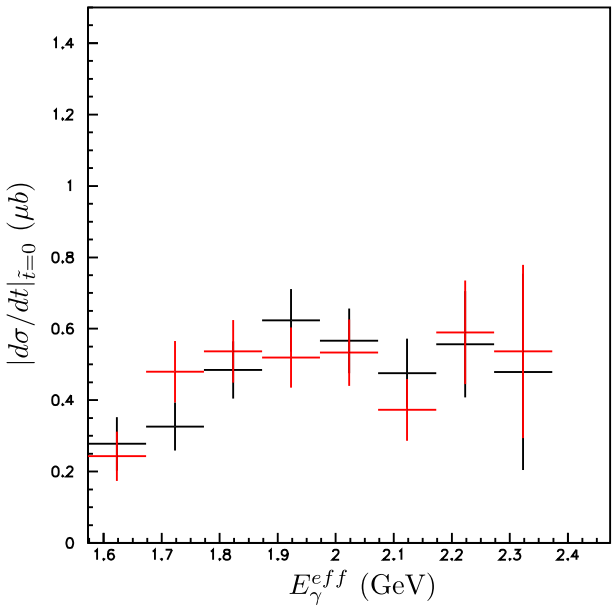

Figure 5.6: The differential cross sections at $\tilde{t} = 0$ GeV^2 in final state with K^+K^-p exclusive event from deuterium target. The black and red histograms show the cross sections as a function of $E_\gamma^{eff}(KKp)$ and $E_\gamma^{eff}(KK)$ respectively. Error bar represents the statistical error only.

Decay asymmetry

Further parity information on isospin effects comes from the decay angular distributions. These distributions were obtained in the Gottfried-Jackson frame and in the region of 1.57≤E$_\gamma$ ≤ 2.37 GeV. In the case of helicity-conservation, the decay asymmetry ρ^{-1}_{1-1}, ($\simeq \tilde{\rho}_3$, because of $\tilde{\rho}_4 \simeq 0$), is reflects the relative contributions of natural-($\rho^{-1}_{1-1} \sim 0.5$) and unnatural-parity($\rho^{-1}_{1-1} \sim -0.5$) processes. Figure 5.7 shows the decay asymmetries $\tilde{\rho}_3$ as a function of photon energy. Compared with those for hydrogen [6], the decay asymmetries for the incoherent reaction is little larger in some photon energy region. When we assuming an equal production from either the proton or the neutron, incoherent $\rho^{-1inco}_{1-1}\sim 0.25$ reconstruct the $\rho^{-1n}_{1-1}\sim 0.3$ from ρ^{-1p}_{1-1} ($\sim$0.2). One theoretical model gives a prediction of $\rho^{-1}_{1-1} = 0.25\sim 0.35$ [7] for $\gamma n \to \phi n$ interaction. The closeness of decay asymmetries in the interactions with nucleons and with free protons actually hints at the weakness of the isoscalar component η-exchange in the unnatural-parity exchange processes. This interpretation is supported by a complete dominance of the natural-parity Pomeron exchange processes in the coherent production[8].

To explain the results for both the weakness of π-η interference and η exchange component, contribution from the pseudo-scalar η exchange process should be small in comparison to the π-exchange process in the threshold energy region. This instance supports the bump structure around $E_\gamma = 2$ GeV for $\gamma p \to \phi + p$ result may be explained the contribution from a new natural parity candidate as a glueball, because the incoherent result shows the isotopic constructive effect in free proton from pseudo-scalar π, η is small in $E_\gamma = 2$ GeV.

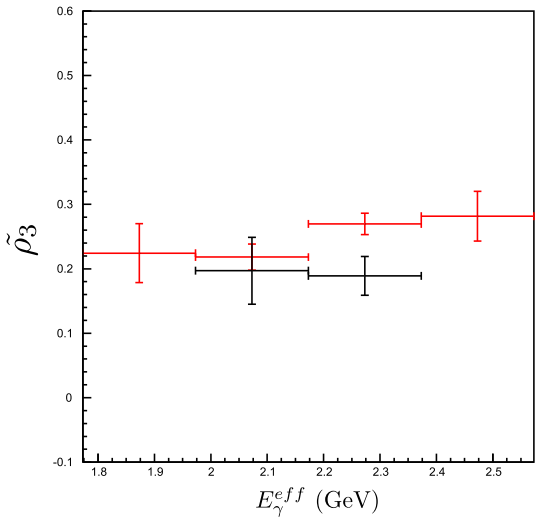

Figure 5.7: $\tilde{\rho}_3$ for incoherent production(red histogram) compared with free proton (black)[6] as a function of photon energy

Chapter 6

Summary

The incoherent photoproduction of ϕ meson off deuteron has been studied in the energy range from the production threshold to E_γ =2.4 GeV using the linearly-polarized photon beam at SPring-8/LEPS.
In order to verify the exotic production mechanisms such as the glueball exchange, the measurements of the differential cross section and spin-density matrix element from deuteron provides a good opportunity to search out such mechanisms. The cross section and decay angular distribution allow the precise study for pseudo scalar meson exchange process from its isotopic effect and unveil the exotic productions.

The high polarized γ beam was produced by Backward Compton Scattering with ultraviolet Ar laser from 8 GeV electrons in the storage ring. The energy of incident photon covered the range from 1.5 to 2.4 GeV which includes ϕ-photoproduction threshold energy. The new 150mm-length Liquid deuterium target system is performed. Charged K^+K^- pair from ϕ meson was detected by LEPS spectrometer. Observed K^+K^- invariant mass spectrum showed sharp peak in ϕ meson mass. Total 17k ϕ meson photoproduction event has been obtained in the experiment from May 2002 to Jun 2003.

Discrimination of the incoherent and coherent process is accomplished using minimum momentum spectator method. To adapt the same framework to the total energy of photon-nucleon system, photon energy resolution for quasi-free process was improved. Since observed $\tilde{t}$ slope of the differential cross sections was found to make no significant difference with proton, production was considered diffractive process. Most forward (0 degree) differential cross section per nucleon shows a significant reduction about 30%. The 3-track final state K^+K^-p cross section is similarly decrease in comparison with free proton. These results suggest the π-η interference is small. We also measured decay angular distribution with linearly polarized photon beam. Since spin density matrix element $\tilde{\rho}_3$ was not clearly different from proton, unnatural parity η-exchange process is small compared with Pomeron exchange process. From these result, pseudo scalar η exchange process is small in ϕ meson production near the threshold. The excess of cross section for free proton can be still interpreted as a possible presence of an additional natural parity exchange mechanisms to cancel out the increasing π exchange.

The target isospin asymmetry is found to be small and cannot be explained such a large

reduction from quasi-free proton. Since the deuteron is loosely bound system, nuclear medium effect is minimal. Some effects which are independent of the nuclear density is required.

Acknowledgements

First of all, I would like to gratefully acknowledge Prof. Takashi Nakano. He has continuously suggested, advised and encouraged me at a every stage of this work. His dedicated supervisions made this work possible.

I deeply appreciate Prof. Wen-Chen Chang. He taught and advised me about analyzing the experimental data. Without his helps and discussions, this work would not be completed.

I express many thanks to Prof. Ken'ichi Imai. He has given me a lot of supports and advices in graduate school.

I would like to thank Prof. Yosoi. He has given instruction in many important techniques on the experiments and the analysis. I have understood the intricacies of the experiments on nuclear physics from working with him.

I really appreciate Dr. H. Kohri, Dr. T. Hotta, Prof. J.K. Ahn, Dr. Y. Sugaya, Dr. T. Yorita, Dr. T. Muramatsu, Dr. H. Fujimura, Prof. A.I. Titov, Prof. H. Shimizu, Dr. T. Ishikawa, Prof. M. Sumihama, Prof. T. Mibe, and Dr. T. Matsumura. They have given a log of supports and helpful suggestions to work on the experiment and data analysis. Without their help, this work would never finished. My special thanks to Mr. T. Sawada, Mr. Y. Kato for their highest encouragement.

I would like to thanks the members of the Spring-8/LEPS collaborators: Ms. D.S. Ahn, Prof. H. Akimune, Dr. Y. Asano, Prof. M. Fujiwara, Prof. S. Fukui, Dr. H. Hasegawa, Prof. K. Hicks, Dr. K. Horie, Prof. T. Iwata, Prof. H. Kawai, Dr. K. Kino, Mr. Y. Kon, Dr. N. Kumagai, Dr. Y. Maeda, Prof. S. Makino, Prof. T. Matsuda, Dr. N. Matsuoka, Prof. Y. Miyachi, Mr Y. Nakatsugawa, Dr. M. Niiyama, Prof. M. Nomachi, Dr. H. Ohkuma, Mr. T. Ooba, Dr. D.S. Oshuev, Prof. Rangacharyulu, Prof. A. Sakaguchi, Prof. P.M. Shagin, Mr. Y. Shiino, Mr. Y. Toi, Dr. M. Uchida, Dr. A. Wakai, Prof S.C. Wang, Dr. K. Yonehara, Dr. M. Yoshimura, and Prof. R.G.T Zegers. I beleive the experiment was not successfully finished without their efforts.
I would like to acknowledge Dr. Y. Ohashi, Dr. S.Date, Dr. H. Toyokawa and other staffs of SPring-8. The SPring-8/LEPS experiments would not be running without their supports.

I have spent enjoyable years in graduate school. I would like to thank all members of Experimental Nuclear and Hadronic Physics Laboratory in Kyoto University: Prof. H. En'yo,

Prof. H. Sakaguchi, Prof. M. Nakamura, Prof. H. Funahashi, Dr. T. Murakami, Prof. N. Saito, Prof. T. Kawabata, Prof. A Ichikawa, Dr. H. Takahashi, Dr. M. Naruki, Dr. R. Muto, Dr. C.J. Yoon, Dr. S. Yamada, Dr. M. Kitaguchi, Mr. K. Miyazaki, Mr. D. Seki, Dr. F. Sakuma, Dr. K. Miwa, Dr. S. Terashima, Dr. M. Togawa, Dr. Y. Fukao, Dr. S. Ota, Dr. K. Aoki, Dr. K. Taketani, Mr. J. Zenihiro, Mr. K. Shoji, Mr. M. Hayata, Mr. Y. Seki, and Mr. S. Dairaku. I particularly appreciate Mr. Y. Yasuda for the encouragement with each other in graduate school. I have been motivated to continue this work by the competition between us.

I wish to thank the members of Institute of Physics in Academia Sinica: Dr. J.Y. Chen, Mr. P.J Lin, Ms. S.Y. Wang, and Mr. T.L. Hsieh. I really appreciate their supports during my stay in Taiwan.

Finally, I would like to thank all persons involved in this work.

Appendix A

Decay angular distribution

In this appendix, the decay angular distribution of ϕ meson is reviewed.
The ϕ-meson rest frame is commonly used in the analysis of the decay angular distributions. There are several ways of defining the quantization axis (z-axis) in the frame. We choose a direction of the incoming photon as a z-axis. This choice of z-axis is so-called the Gottfried Jackson (GJ) frame. The GJ frame is the most suitable frame for analyzing the t-channel exchange mechanisms since some of the t-channel exchange amplitudes have a simple helicity-conserving form which is independent of the momentum transfer [2]. In the GJ frame, production plane is defined as a plane on which momentum vectors of the incoming photon and produced ϕ-meson lie. The y-axis is defined as a direction normal to the production plane, the x-axis is defined as a direction of outer product $\hat{y} \times \hat{z}$.

We define the following angles ; ϕ, Φ, and θ. θ is the polar angle between the K^+ meson and the ϕ-meson production plane in the ϕ-meson rest frame. ϕ is an azimuthal angle between the K^+ meson and the ϕ-meson production plane in the ϕ-meson rest frame. Φ is an azimuthal angle between the photon polarization vector and the ϕ-meson production plane in the overall center-of-mass frame. The definitions of these angles are shown in Fig.A.1.

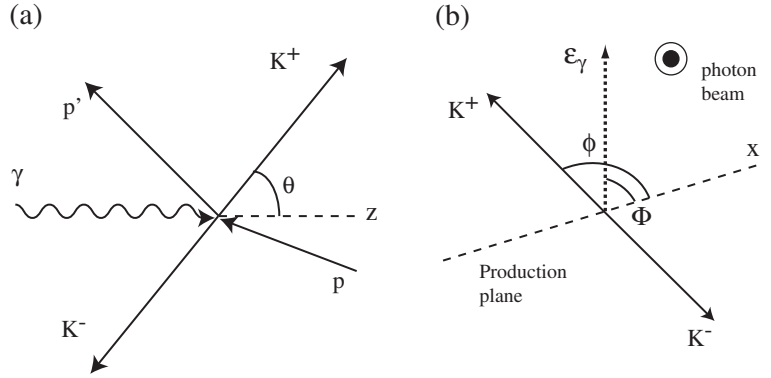

Figure A.1: Decay angles (Gottfried-Jackson frame) for the reaction $\gamma + p \to \phi + p \to K^+K^-p$. (a) diagrammatic representation of the system viewed from the x-axis, (b) the system viewed from the z-axis, where the arrow with $p(p\prime)$ stands for direction of the incident (outgoing) proton, and ϵ_γ represents the direction of the photon polarization.

The decay angular distribution $W(\phi, \theta, \Phi)$ for ϕ photoproduction by linearly-polarized pho-

tons are expressed using nine spin-density matrix elements ρ^0,ρ^1,ρ^2 and the polarization degree of the photon beam P_γ [46]:

$$W(\phi,\theta,\Phi) = (W^0 - P_\gamma\cos(2\Phi)W^1 - P_\gamma\sin(2\Phi)W^2) \quad (A.1)$$

where, W^0 is the polarization-independent part and W^1 and W^2 are polarization-dependent parts. W^0, W^1 and W^2 are represented in following form:

$$\begin{aligned}
W^0 &= \frac{3}{4\pi}(\frac{1}{2}(1-\rho^0_{00}) + (3\rho^0_{00}-1)\cos^2\theta \\
&\quad -\sqrt{2}Re(\rho^0_{10})\sin(2\theta)\cos\phi - \rho^0_{1-1}\sin^2\theta\cos(2\phi)), \\
W^1 &= \frac{3}{4\pi}(\rho^1_{11}\sin^2\theta + \rho^1_{00}\cos^2\theta \\
&\quad -\sqrt{2}Re(\rho^1_{10})\sin(2\theta)\cos\phi - \rho^1_{1-1}\sin^2\theta\cos(2\phi)), \\
W^2 &= \frac{3}{4\pi}(\sqrt{2}Im(\rho^2_{10})\sin(2\theta)\sin(\phi) + Im(\rho^2_{1-1})\sin^2\theta\sin(2\phi)) \quad (A.2)
\end{aligned}$$

The three-dimensional angular distribution Eq. A.1 can be reduced to one-dimensional distribution for a particular angular variable after integrating over the other remaining angles :

$$\begin{aligned}
W(\cos\theta) &= \frac{3}{2}(\frac{1}{2}(1-\rho^0_{00})\sin^2\theta + \rho^0_{00}\cos^2\theta)) & (A.3)\\
W(\phi) &= \frac{1}{2\pi}(1 - 2\mathrm{Re}\rho^0_{1-1}\cos 2\phi) & (A.4)\\
W(\phi-\Phi) &= \frac{1}{2\pi}(1 + P_\gamma(\rho^1_{1-1} - \mathrm{Im}\rho^2_{1-1})\cos 2(\phi-\Phi)) & (A.5)\\
W(\phi+\Phi) &= \frac{1}{2\pi}(1 + P_\gamma(\rho^1_{1-1} + \mathrm{Im}\rho^2_{1-1})\cos 2(\phi+\Phi)) & (A.6)\\
W(\Phi) &= \frac{1}{2\pi}(1 - P_\gamma(2\rho^1_{11} + \rho^1_{00})\cos 2\Phi) & (A.7)
\end{aligned}$$

The spin-density matrix elements (ρ^0, ρ^1, ρ^2) are bilinear combinations of scattering amplitude. We follow the standard definition given in Ref. [3]:

$$\begin{aligned}
\rho^0_{\lambda\lambda'} &= \frac{1}{N}\sum_{\alpha,\lambda_\gamma} I_{\alpha;\lambda,\lambda_\gamma} I^\dagger_{\alpha;\lambda',\lambda_\gamma}, \\
\rho^1_{\lambda\lambda'} &= \frac{1}{N}\sum_{\alpha,\lambda_\gamma} I_{\alpha;\lambda,-\lambda_\gamma} I^\dagger_{\alpha;\lambda',\lambda_\gamma}, \\
\rho^2_{\lambda\lambda'} &= \frac{i}{N}\sum_{\alpha,\lambda_\gamma} \lambda_\gamma I_{\alpha;\lambda,-\lambda_\gamma} I^\dagger_{\alpha;\lambda',\lambda_\gamma}, \quad (A.8)
\end{aligned}$$

where λ_γ, λ ($\lambda\prime$) are helicity of the incoming photon, helicity of outgoing ϕ meson, respectively. I represents the scattering amplitude, and N is a normalization factor. α is a set of the other quantum numbers including the polarization of the incoming and outgoing proton. The

scattering amplitude I consists of helicity conserving amplitude ($\equiv I_{\lambda,\lambda}$) and helicity non-conserving amplitude ($\equiv I_{\lambda,\lambda'}$ with $\lambda \neq \lambda'$). As shown in Eq. A.8, the spin-density matrix elements are the product of these two types of amplitudes. When only helicity-conserving amplitudes are present in the process, the elements ρ^1_{1-1} and $\mathrm{Im}\rho^2_{1-1}$,which contain products of helicity-conserving amplitudes, are possible to have non-zero values. All the other elements, in which all terms contain helicity non-conserving amplitudes, are 0 ; i.e. Eq. A.8 leads :

$$\begin{aligned}
\rho^1_{1-1} &= \frac{1}{N}\sum_{\alpha,\lambda_\gamma} I_{1,-\lambda_\gamma}\, I^\dagger_{-1,\lambda_\gamma} \\
&= \frac{1}{N}\sum_{\alpha} I_{1,-1}\, I^\dagger_{-1,1} + I_{1,1}\, I^\dagger_{-1,-1} \\
&= \frac{1}{N}\sum_{\alpha} I_{1,1}\, I^\dagger_{-1,-1} \\
&= -\mathrm{Im}\rho^2_{1,-1} \\
&\quad \rho^0_{00} = \rho^0_{1-1} = \mathrm{Re}\rho^0_{10} = \rho^1_{00} = \mathrm{Re}\rho^1_{10} = \rho^1_{11} = \rho^2_{10} = 0.
\end{aligned} \tag{A.9}$$

The amplitudes for Pomeron exchange, scalar (0^+ glueball) exchange (natural-parity exchange, $J^P = 0^+$) and pseudo scalar (π,η) exchange (unnatural-parity exchange, $J^P = 0^-$) are examples of the helicity-conserving amplitude at forward angles. Pure natural-parity exchange gives $\rho^1_{1-1} = -\mathrm{Im}\rho^2_{1-1} = +1/2$, while pure unnatural-parity exchange gives $-1/2$. When both of these two contribute to the scattering amplitude with a relative weight β ($I_{tot} = \sqrt{1-\beta^2}I^N + \beta I^{UN}$), the spin-density matrix elements are given by

$$\rho^1_{1-1} = -\mathrm{Im}\rho^2_{1-1} = \frac{1-2\beta^2}{2}, \tag{A.10}$$

and all the other elements are zero. Therefore, information on ρ^1_{1-1} and $\mathrm{Im}\rho^2_{1-1}$ provides the relative weight (β) between natural-parity exchange and unnatural-parity exchange under the absence of the helicity non-conserving amplitudes.

When the helicity non-conserving amplitude is present, the other seven spin-density matrix elements could have non-zero value. Examples of helicity non-conserving amplitude are the tensor meson (f'_2) exchange, and the production of nucleon resonances which couples to ϕN. Fig. A.2 shows predictions of the decay angular distribution for the Pomeron exchange, f'_2 exchange (2^+) and glueball exchange (0^+). A large helicity non-conserving contribution from f'_2 exchange results in remarkable difference in the angular distributions, while the Pomeron and glueball exchanges give similar distributions.

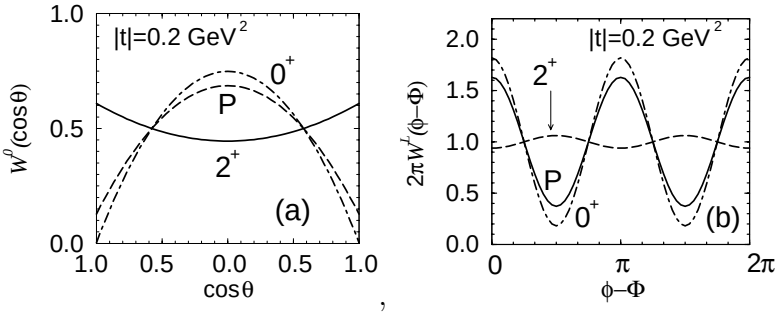

Figure A.2: Predictions for the decay angular distribution by Ref. [3]. (a) $\cos\theta$ distribution (b) $\phi - \Phi$ distribution, for ϕ photoproduction at E_γ =2.2 GeV. The Solid, dashed and don-dashed curves indicate the predictions from (P) Pomeron exchange + pseudo scalar exchange, (2^+) f_2' exchange + pseudo scalar exchange and (0^+) glueball exchange + pseudo scalar exchange (0^+), respectively.

Appendix B

Study for Final State Interaction effect

In this appendix, we present the study for Final State Interaction of incohrent ϕ photoproduction.
Near the threshold region the relative velocity of the outgoing nucleon is small which might result in a strong final state interaction (FSI) between them.

B.1 PN relative momentum

In order to estimate for FSI strength, relative momentum between proton and neutron in deuteron is required. Since we detect only a KK pair, in this analysis, we estimate momenta of nucleons from Missing Momentum k as following equation.

$$P_{miss} = P_\gamma - P_\phi$$

$$E_{miss} = E_\gamma + M_D - E_\phi$$

$$M_{pn}^2 = E_{miss}^2 - P_{miss}^2$$

$$k = \frac{\sqrt{(M_{pn}+M_p+M_n)(M_{pn}-M_p+M_n)(M_{pn}+M_p-M_n)(M_{pn}-M_p-M_n)}}{2M_{pn}}$$

this relations are quiete the same assumption as p_{min}^{spec}. In Sec.3.5, the p_{min}^{spec} gives good estimation for target nucleons momentum.

Fig.B.1 shows PN relative momentum k distribution of ϕ event in Real data.

B.2 coherent contribution

On the other hand, in coherent production case, the PN relative momentum k equal to zero when neglectin the small deuteron binding energy, But the effect of experimental resolution, relative momentum k flow out over zero. Fig.B.2 shows k^2 distribution in coherent MC simulation. The 0.9 (9)% of total coherent event are exist with cut condition $k^2 \geq 0.1(0.05)$ assuming $\Delta E\gamma = 10MeV$.

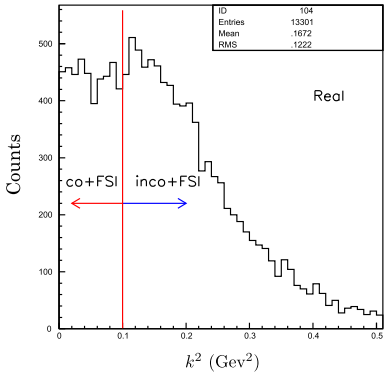

Figure B.1: k^2 distribution (Real data)

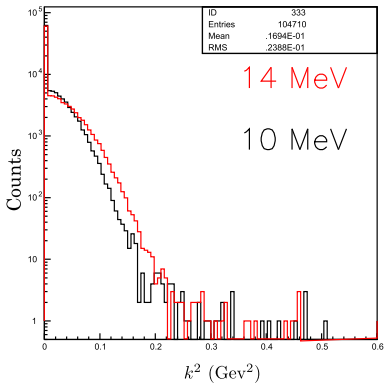

Figure B.2: PN relative momentum distribution for coherent MC. Black:$\Delta E_\gamma = 10[MeV]$, Red:$\Delta E_\gamma = 14[MeV]$

B.3 FSI enhancement factor

From the theoretical calculations[47], FSI enhancement function $F_{s,t}(k)$ for PN singlet case reads

$$F_s(k) = \frac{k^2 + \alpha_0^2}{k^2 + \beta^2} \tag{B.1}$$

$$\alpha_0 = (\sqrt{1. - 2. * r_0/a_0} + 1.)/r_0$$

$$\beta = (\sqrt{1. - 2. * r_0/a_0} - 1.)/r_0$$

and in triplet case,

$$F_t(k) = \frac{k^2 + \alpha_1^2}{k^2 + \kappa^2} \tag{B.2}$$

$$\alpha_1 = (2. - \kappa * r_1)/r_1$$

Where, k is momentum of two identical particles in cms, $\kappa^2 = 2\mu\epsilon_d$, ϵ_d is deuteron binding energy, NP scattering length(singlet) $a_0 = -23.768fm$, NP effective radius(singlet)

$r_0 = 2.75fm$, NP effective radius(triplet) $r_1 = 1.759fm$, $\kappa^{-1} = 4.318fm$ respectively. These values are obtained from the low energy NN scattering experiment[48]. Fig.B.3 shows enhancement values with momentum k^2.

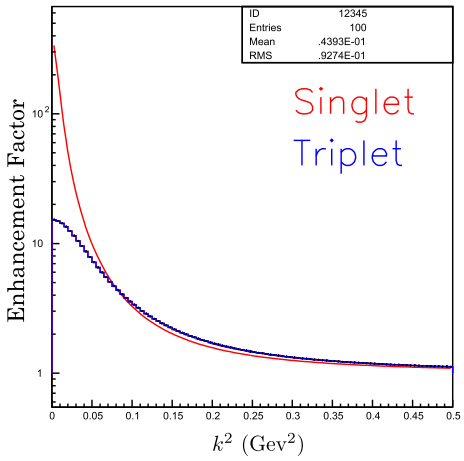

Figure B.3: Final state interaction enhancement factor

B.4 Comparison of Real data with MC

Fig.B.1 shows k^2 distribution in Real data, and Fig.B.4 shows incoherent MC distribution. In the lower k^2 region, because real data contains FSI process and coherent process like Fig.B.2, the distribution is differ from incoherent MC one.

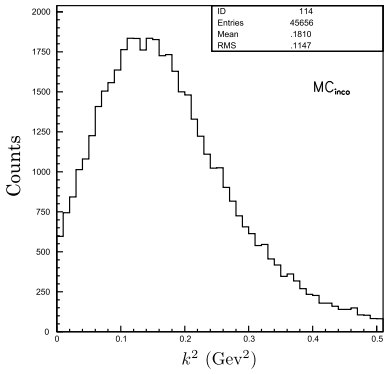

Figure B.4: k^2 distribution (MC inco)

We filtered MC simulation using Function.B.2 and check the FSI effect. Fig. B.6 shows the missing mass distribution on deuteron (MM_d) distributions. The results of MC simulation including singlet(triplet) FSI are placed with Real data. Since the singlet contribution is too strong in the coherent region $MM_D \sim 1.87$, the triplet enhancement is favor in this study.

Fig.B.5 shows the 3-combination fit for Real data, using coherent MC, incoherent MC and FSI including MC simulation. Ratios of the incoherent production and FSI is less than $\sim 1\%$ all over the energy region.

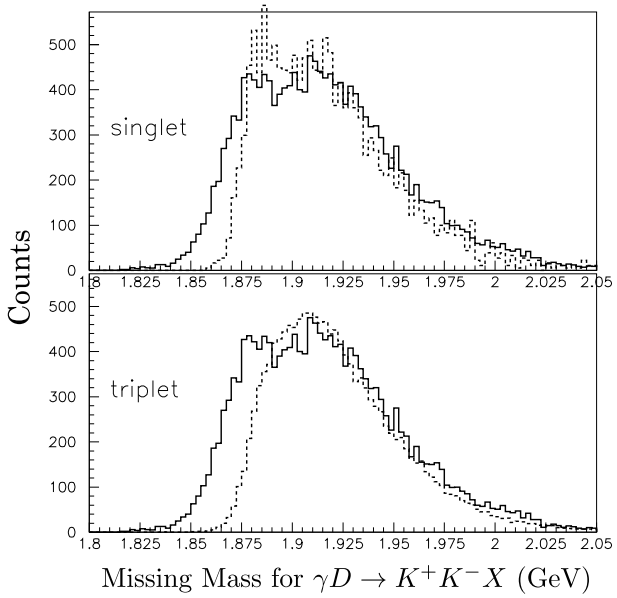

Figure B.5: MM_D distribution (Real data) comparison with FSI including MC. Solid line and dashed line show Real data and MC simulation containing FSI respectively

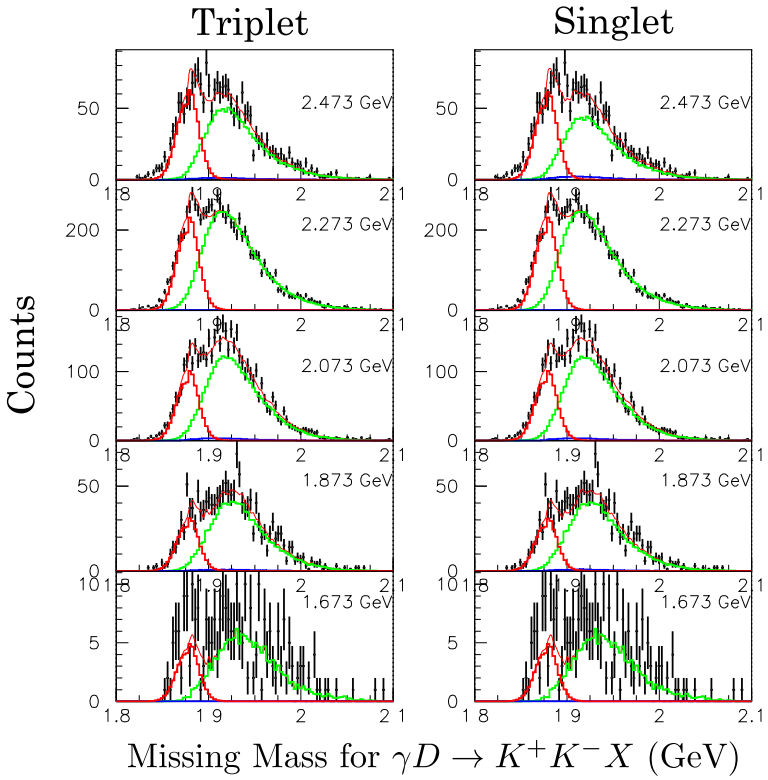

Figure B.6: 3-component fit for MM_D distribution. Histograms with error-bars show Real data. Red, Green and Blue histograms are coherent MC, incoherent MC, and FSI MC respectively.

Appendix C

Various check of the cross section for several p_{min}^{spec} cut

In this section, we report the validity check for p_{min}^{spec} cut. Since the p_{min}^{spec} reflect the target nucleon momentum, if set the tighter cut for p_{min}^{spec}, deduce the clean qusai-free $\gamma N \to \phi N$ process, but of course, statistics becomes poor. On the other hand, when we choose looser cut, the contamination from coherent production around $p_{min}^{spec} = 0.2$ was not negligble. Figure C.1 shows the slope parameter as a function of p_{min}^{spec} in various energy bin. Figure C.2 also discribes the differential cross section at $\tilde{t}$=0 depends on p_{min}^{spec} cut condition. In the region $E_\gamma \leq 2.173(GeV)$ which corresponds to $E4 \sim E9$, slope and cross section keep a flat distribution around $|p_{min}^{spec}| \leq 90$MeV cut. But in the case of E1, E2 and E3, the cross section increases depending on $|p_{min}^{spec}|$ cut.

As a result of coherent production study[8], the coherent ϕ production cross section increases depending on the incident photon energy. Fig. C.3 shows Missing Mass $\gamma D \to K^+K^-X$ spectra fitted with the sum of MC simulated components of coherent and incoherent events. Obviously, at E1-E3 there are large contributions of coherent events. We calculated the contamination by coherent event in the several p_{min}^{spec} cut condition. Fig. C.4 shows the coherent contamination as a function of p_{min}^{spec} cut condition. The contribution from coherent is less than 3% in the region $E_\gamma \leq 2.173(GeV)$ with $|p_{min}^{spec}| \leq 90$MeV cut, but at the E1, E2 and E3, the coherent contamination reaches 12%, 6.1% and 4.7% respectively.

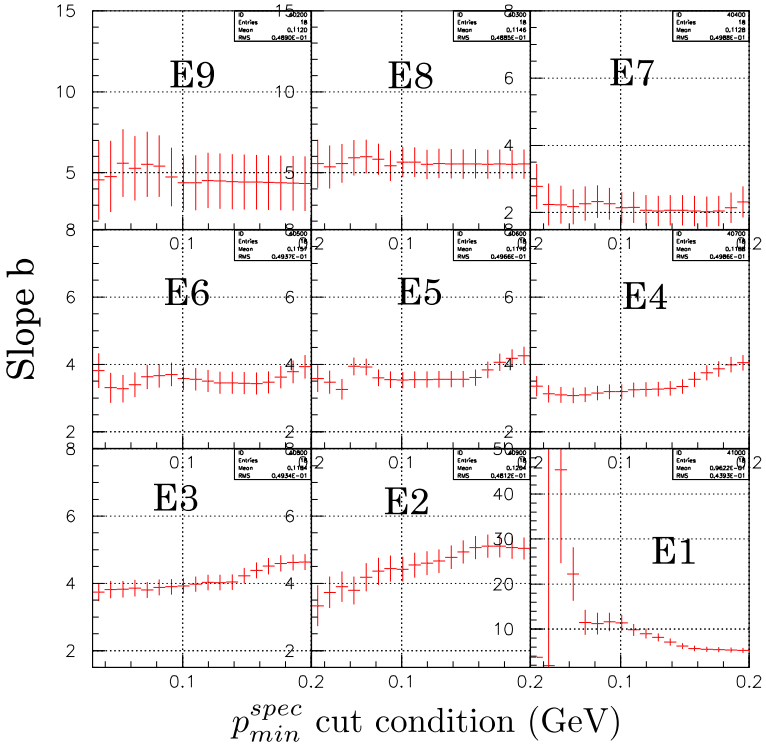

Figure C.1: slope parameter b as a function of p_{min}^{spec} cut.

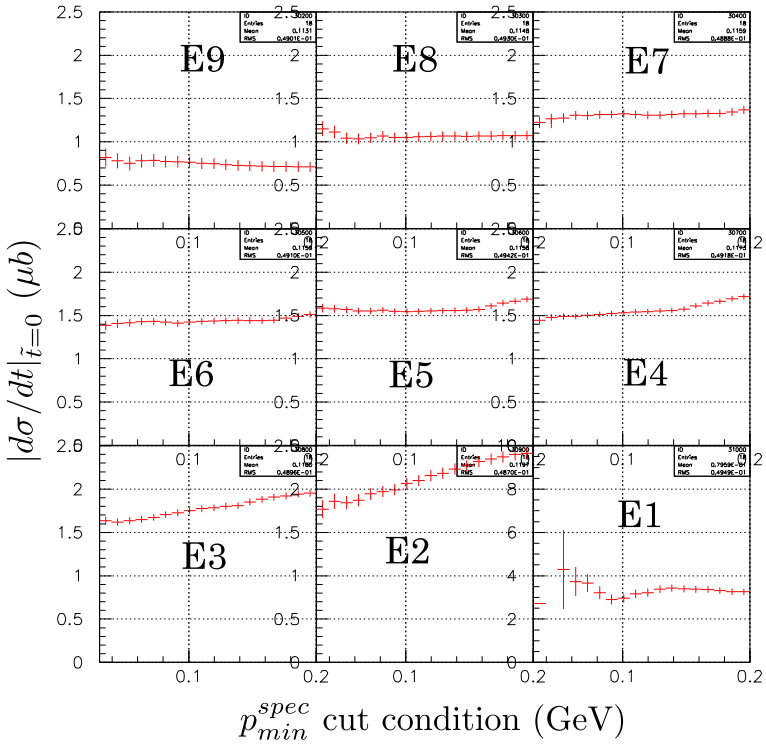

Figure C.2: $|\frac{d\sigma}{dt}|_{\tilde{t}=0}$ as a function of p_{min}^{spec} cut. Constant slope parameter was used in all energy.

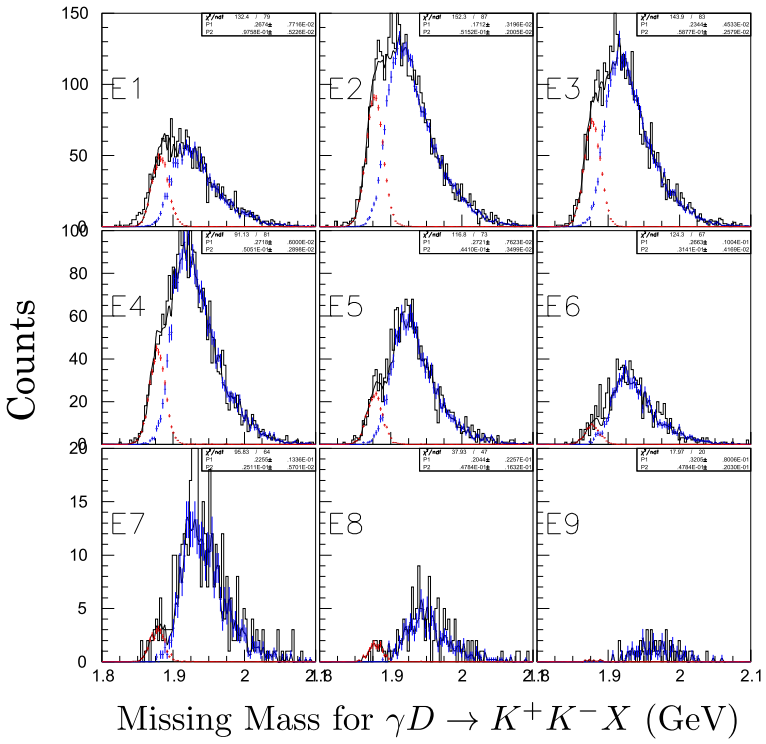

Figure C.3: Missing Mass $\gamma D \to K^+K^-X$ (MM_D) spectra fitted with the sum of MC simulated components of coherent (red line) and incoherent (blue line) events.

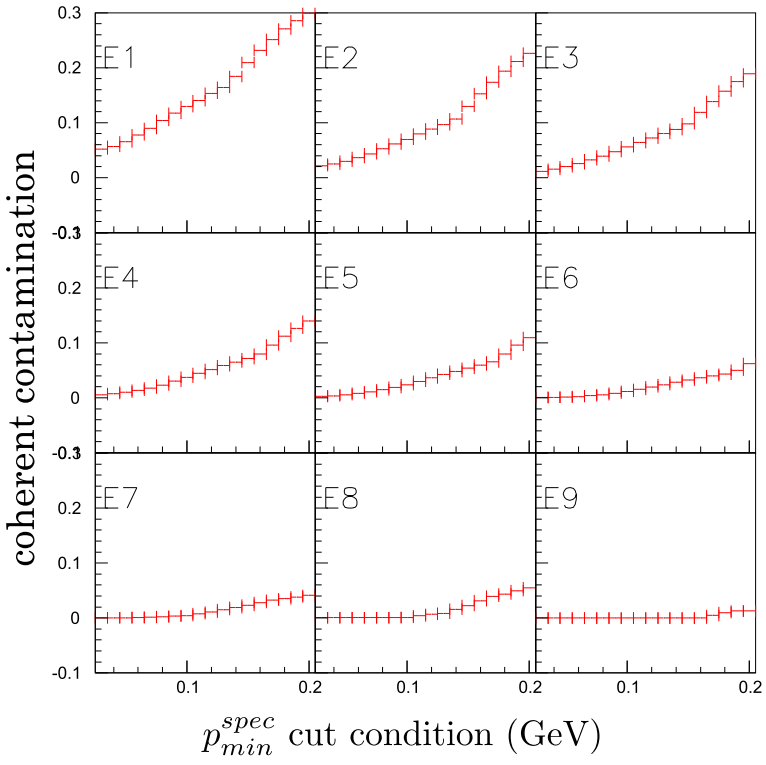

Figure C.4: The contamination of coherent events as a function of p_{min}^{spec} cut.

Bibliography

[1] T. Nakano and H. Toki, Internal Workshop on Exiting Physics with New Accelerators Facilities (EXPAF97) (1997).

[2] A. I. Titov, T. S. H. Lee, et al., Physical Review C **60**, 035205 (1999).

[3] A. I. Titov and T. S. H. Lee, Phys. Rev. **C67**, 065205 (2003), `nucl-th/0305002`.

[4] J. J. Sakurai, Annals Phys. **11**, 1 (1960).

[5] T. Regge, Nuovo Cim. **14**, 951 (1959).

[6] T. Mibe et al. (LEPS), Phys. Rev. Lett. **95**, 182001 (2005), `nucl-ex/0506015`.

[7] A. I. Titov, T. S. H. Lee, and B. Kampfer, Physical Review **C76**, 035202 (2007).

[8] W. Chang et al. (LEPS), Physics Letter B **658**, 209 (2008).

[9] T. Mibe et al. (CLAS), Physical Review (2007).

[10] A. I. Titov, T.-S. H. Lee, and H. Toki, Phys. Rev. **C59**, R2993 (1999).

[11] T. Ishikawa et al., Phys. Lett. **B608**, 215 (2005), `nucl-ex/0411016`.

[12] R. H. Milburn, Phys. Rev. Lett. **10**, 75 (1963).

[13] F. R. Arutyunian and V. A. Tumanian, Phys. Lett. **4**, 176 (1963).

[14] J. Ballam et al., Phys. Rev. **D7**, 3150 (1973).

[15] A. M. Sandorfi, J. LeVine, C. E. Thorn, G. Giordano, and G. Matone, IEEE Trans. Nucl. Sci. **30**, 3083 (1983).

[16] H. Ohgaki et al., IEEE Trans. Nucl. Sci. **38**, 386 (1991).

[17] J. P. Bocquet et al., Nucl. Phys. **A622**, 124c (1997).

[18] J. K. Ahn et al. (1999), prepared for 12th Symposium on Accelerator Science and Technology (SAST'99), Wako, Japan, 27-29 Oct 1999.

[19] T. Matsumura (LEPS), Master thesis of Yamagata University (in Japanease) (2000).

[20] http://www.spring 8.or.jp.

[21] T. Nakano et al., Nucl. Phys. **A684**, 71 (2001).

[22] T. Nakano et al. (LEPS), Phys. Rev. Lett. **91**, 012002 (2003), `hep-ex/0301020`.

[23] R. G. T. Zegers et al. (LEPS), Phys. Rev. Lett. **91**, 092001 (2003), `nucl-ex/0302005`.

[24] J. K. Ahn (LEPS), Nucl. Phys. **A721**, 715 (2003).

[25] T. Hotta (LEPS), Nucl. Phys. **A721**, 751 (2003).

[26] T. Matsumura (LEPS), Doctor thesis of Osaka university (2004).

[27] N. Muramatsu et al. (LEPS), LEPS technical note **14** (2002).

[28] K. Tsumaki, SPring-8 annual report p. 132 (1998).

[29] Y. Kato (LEPS), LEPS technical note **34** (2007).

[30] H. Kohri et al. (LEPS), RCNP annual report (2002).

[31] V. Fild Ltd., *OPERA-3D TOSCA*, URL `http://www.vectorfields.co.uk`.

[32] T. Ishikawa (LEPS), Ph.D. thesis (2005).

[33] M. Sumihama (LEPS), Ph.D. thesis (2003).

[34] Y. Sugaya et al., IEEE Trans. Nucl. Sci. **48**, 1282 (2001).

[35] N. Muramatsu et al. (LEPS), LEPS technical note **1** (2002).

[36] T. Mibe (LEPS), Ph.D. thesis (2004).

[37] W. Chang et al. (LEPS), LEPS technical note **2** (2002).

[38] Http://wwwasd.web.cern.ch/wwwasd/geant/index.html.

[39] M. Lacombe et al., Phys. Lett. **B101**, 139 (1981).

[40] K. Particle Data Group, Hagiwara, Phys. Rev. **D66**, 010001 (2002).

[41] E. Anciant et al. (CLAS), Phys. Rev. Lett. **85**, 4682 (2000), `hep-ex/0006022`.

[42] T. Nakano (LEPS), LEPS technical note **56** (2002).

[43] K. Kino (LEPS), LEPS technical note **12** (2002).

[44] D. Cabrera et al., Nucl. Phys. **A733**, 130 (2004).

[45] A. Sibirtsev et al., Eur. Phys. J **A29**, 209 (2006).

[46] K. Schilling, P. Seyboth, and G. E. Wolf, Nucl. Phys. **B15**, 397 (1970).

[47] A. I. Titov, B. Kampfer, and B. L. Reznik, arXiv:nucl-th **0001027v1** (2000).

[48] O. Dumbrajs, R. Koch, and H. Pilkuhn, Nuclear Physics **B216**, 277 (1982).